Laser Magnetic Resonance applied to excited States of Iodine and to the Fine structure Transition in the electronic Groundstate of Iodine Monoxide

Dissertation
zur
Erlangung des Doktorgrades (Dr. rer. nat.)
der
Mathematisch-Naturwissenschaftlichen Fakultät
der
Rheinischen Friedrich-Wilhelms-Universität Bonn

vorgelegt von
Thomas H. Breitbach
aus
Andernach

Bonn 2001

Angefertigt mit Genehmigung der Mathematisch-Naturwissenschaftlichen Fakult¨at der Rheinischen Friedrich-Wilhelms-Universit¨at Bonn

Acknowledgements

First of all I wish to thank Prof. Dr. Wolfgang Urban and Prof. Dr. John M. Brown for giving me the opportunity to carry out this investigation. They both guided me through it and did not limit their support to purely academical matters.

Furthermore I am also grateful for the support of Dr. Christian Schmidt. He was my 'big brother' in the lab and introduced me to the technique of Faraday-LMR. Whenever the setup caused serious trouble he provided helpful advice and it was a pleasure to work with him. Not only for his advice but also for raising the mood when saying something like: "Na, dann werden Sie mal kreativ!"

Highly appreciated was the help of the groups at Bonn and at Oxford. It was fun to work with people like Dr. Ralph G¨abler and Andreas Jentsch at Bonn or Dr. Christian Hill and Dr. Stephen Kermode at Oxford. They provided a friendly atmosphere in which it was easy to work as well as to relax.

I am also most grateful for the support that I received from my parents. Their permanent encouragement gave me the sedateness necessary to cope with difficult times. Another valuable contribution to this has been made by Miss Silke Rhein who stayed with me during the most exhausting times.

Many other persons have contributed to this work but I can not mention all of them explicitly. Be it the workshops at Bonn or the friends at Kruft, Bonn, Oxford and elsewhere. Many thanks to all of you!

Finally, it should be mentioned that this work was supported by the Sonderforschungsbereich 334 of the Deutsche Forschungsgemeinschaft and the Deutscher Akademischer Auslands Dienst.

Contents

Chapter 1

Introduction

In this thesis two very different quantum mechanical systems are investigated: The first one is the iodine atom. This system is characterized by 53 electrons collected around a heavy nucleus ($m_I = 127amu$) with a large nuclear spin of $\frac{5}{2}$. These properties make the iodine atom a rather complicated quantum mechanical system with a huge number of closely spaced electronic states at high energy so that all kinds of perturbations may occur.

Despite the complex scheme of electronic terms realized in iodine, it has been widely investigated already. Due to the rather high vapor pressure of the iodine crystals it was relatively straightforward to handle in the laboratory. To obtain single atoms from the vapor is easily done in a gas discharge. In later years many investigations of atomic iodine were indeed by-products of other investigations. E.g., A. Gedanken *et al.* report in [Ged82] an investigation of the photo-dissociation of methyl iodide in which the CH_3I molecule was split into a CH_3 radical and an excited iodine atom. Thus, the investigation of methyl iodide also provided information on the iodine atom.

Some technological interest in iodine atoms has arisen due to the invention of the iodine laser (eg. [Sch88]). This laser operates on the transition between the two spin components $^2P_{\frac{3}{2}}$ and $^2P_{\frac{1}{2}}$ at a wavelength of $1.315\mu m$.

The results of the present work could find another application in astronomy. B. Lemoine *et al.* report in [Lem88] the observation of certain Rydberg transitions of magnesium in the laboratory that were previously observed in the spectrum of the sun. They suggest that the magnetic properties measured in the laboratory could be used to determine the solar magnetic field with high accuracy. Obviously, this determination depends crucially on the knowledge of the Zeeman effect. The only magnetic data of iodine

currently available are the ones obtained by C. E. Moore in [Moo71] and Luc-Koenig *et al.* [LK75], so that it seems worthwhile to study the excited states of iodine under high resolution in order to provide more accurate information about such states.

The second species investigated here is iodine monoxide. Several reasons make this molecule a very interesting one. Theoretical chemists are interested in it because it is the heaviest accessible member of the halogen oxides. Since FO, ClO and BrO are quite well known already, it becomes possible to observe the increase of relativistic effects in dependence on the mass of the molecules. Also, the most simple oxide, OH, has the same open shell electronic structure as the halogen oxides. Thus, the iodine monoxide appears to be just the most complicated molecule in a series of very basic ones.

Another, much more applied aspect is found in atmospheric chemistry (eg. [All00, Wit00]. It is well known that the ClO molecule is causing the rapid destruction of the ozone layer via a catalytic cycle in which the radicals are recovered after destroying a number of ozone molecules. While the concentrations of fluorine and chlorine in the atmosphere result completely from human sources, the concentration of iodine arises almost completely from the emission by marine sources. Since for iodine monoxide the same catalytic cycle is possible as for the other halogen oxides, this raises the question whether some of the depletion of the ozone layer is just a natural effect.

Since spectroscopy can be used for remote monitoring of the concentration of such molecules, it is important to know their spectra quite well. Therefore this series of molecules has been investigated thoroughly by spectroscopy in the optical as well as in the infrared and microwave region (eg. [Car67, Car70, Bro72, Sai73, Bek83, Tam99, Tam01, Mil01]). The electronic ground state of FO, ClO and BrO have been fully characterized now. For IO the situation is slightly worse. Although most parameters necessary to describe the electronic ground state of this molecule are known quite well, the spin-orbit splitting has not been measured directly up to now. Therefore the aim of the work on IO that is presented in this thesis was the direct measurement of the absorption frequency for transitions between both spin-orbit components.

The next chapter will explain the apparatus used for the two different investigations. The following chapter describes the investigation of the spec-

tra of atomic iodine. It is followed by the corresponding chapter for iodine monoxide. Although each of the two main parts ends with a brief summary of the results, a short summary of the achievements finishes the thesis.

Chapter 2

The Faraday-Rotation Laser Magnetic Resonance Spectrometer at Bonn

It is the aim of this chapter to give a brief introduction to the more technical details of the experiment. First, the general idea of Laser Magnetic Resonance is described. It is then shown how the Faraday effect can be used to increase the sensitivity of the apparatus further.
The next subsection then describes briefly how these principles are transferred to the real apparatus. There follows a brief description of the different radiation sources used for this study. In order to get a feeling for the quality of the analysis of the experimental data the last section of the chapter presents a rough estimate of the accuracy of apparatus.

2.1 The Zeeman Effect and the Technique of Laser Magnetic Resonance

Whenever a system of charged particles possesses a non-vanishing total angular momentum this produces a magnetic moment. The interaction of this magnetic moment with an external magnetic field leads in quantum mechanics to the Zeeman effect, i.e. the splitting of a single state $|\eta, J, M_{\mathbf{J}}>$ [1] of energy E and total angular momentum **J** into its $(2J+1)$ $M_{\mathbf{J}}$-components.

In first order approximation this splitting of the different components

[1] In this thesis all vectorial variables are denoted in bold while quantum numbers are denoted in italic. The symbol η is used as an abbreviation for all further quantum numbers necessary to identify a particular state of the system under consideration.

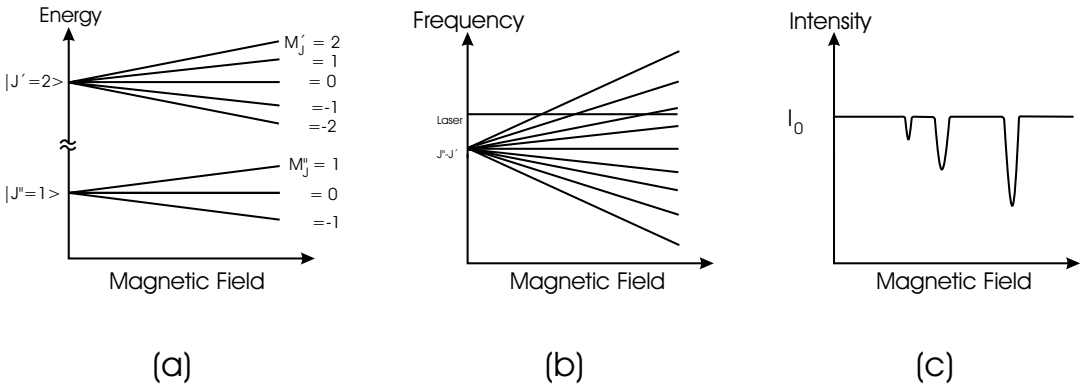

Figure 2.1: Tuning of two states of a paramagnetic system in a magnetic field. Trace (a) shows how the different $M_{\mathbf{J}}$ levels shift with the magnetic field strength. In (b) it is shown, how the transition frequency between those levels shifts correspondingly. Finally, the resultant intensity obtained in an absorption experiment is shown in trace (c).

is proportional to the applied magnetic field and to $M_{\mathbf{J}}$ so that it can be described by:

$$E_{\eta,J,M_{\mathbf{J}}}(B) = E_{\eta,J,M_{\mathbf{J}}}(B=0) + g_{\mathbf{J}} \cdot \mu_{Bohr} \cdot M_{\mathbf{J}} \cdot B \tag{2.1}$$

Here the constant $g_{\mathbf{J}}$ is the so-called Landé-factor. This situation is shown in figure (2.1) (a).

Since the magnetic moments for the different states are usually different, the transition frequency between such states varies with field as:[2]

$$\begin{aligned} \nu(B) &= \nu_0 + (g_{\mathbf{J}'} \cdot \mu_{Bohr} \cdot M'_{\mathbf{J}} - g_{\mathbf{J}''} \cdot \mu_{Bohr} \cdot M''_{\mathbf{J}}) \cdot B \\ &= \nu_0 + \frac{\Delta\nu}{\Delta B} \cdot B \end{aligned} \tag{2.2}$$

where ν_0 is the transition frequency in the absence of an external magnetic field and $\frac{\Delta\nu}{\Delta B}$ is called the tuning rate of the transition. It is usually of the order of $10\ \mathrm{MHz/mT}$.

Thus the transitions can be tuned by varying the magnetic field as it is shown in figure (2.1) (b). The technique of Laser Magnetic Resonance

[2]Throughout this work, the lower state is designated by the $''$ while the upper state is designated by $'$.

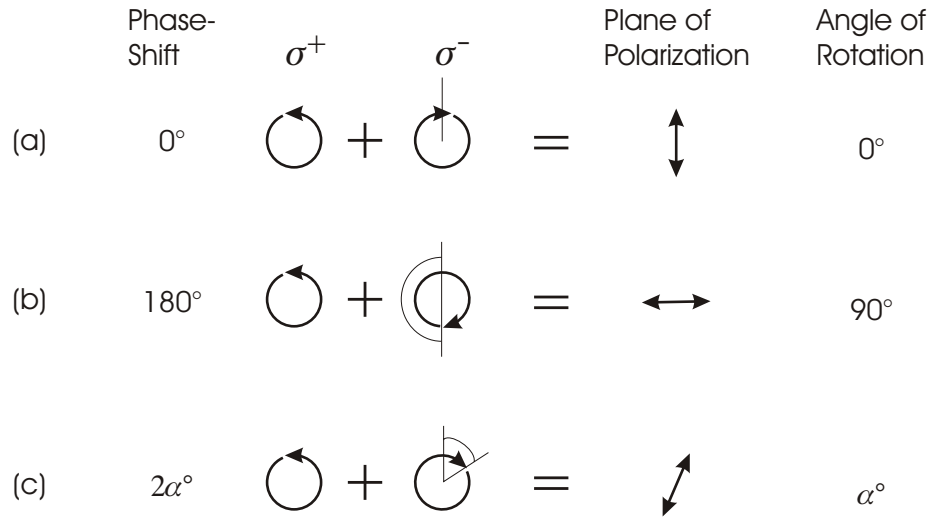

Figure 2.2: A linear polarized wave can be thought to be made of two circular polarized waves. The plane of polarization depends on the phase shift between the two circular polarized components. For 0° a vertical plane of polarization is obtained (a). A wave polarized at an angle of 90° corresponds to a phase shift of 180° (b). Any intermediate phase shift leads to a different plane of polarization (c).

makes use of this property. Here the light source is kept at a constant frequency and the sample itself is tuned into resonance with the light source. Whenever the transition frequency coincides with the laser frequency absorption occurs. Thus the observed intensity varies with the magnetic field as it is shown in figure (2.1) (c).

2.2 The Faraday-Effect and Polarization Sensitive Detection

For the possible transitions between the different M_J components the selection rule $\Delta M_J = 0, \pm 1$ applies. Which of these transitions can be observed depends on the geometry of the experiment. When the optical axis is transverse to the magnetic field, transitions with all three different values of ΔM_J can take place and it is possible to distinguish between transitions with $\Delta M_J = 0$ and $\Delta M_J \neq 0$ depending on the polarization of the light wave.

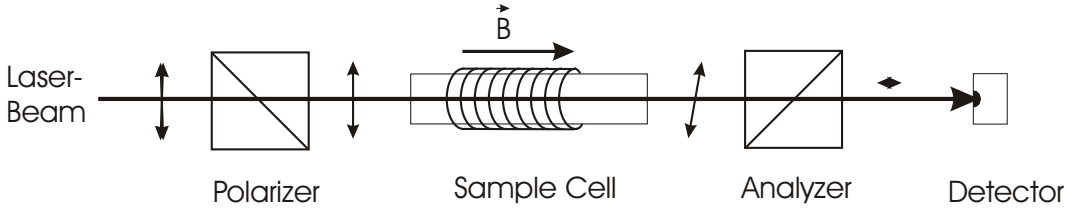

Figure 2.3: The principal configuration used in a Faraday-Laser Magnetic Resonance Spectrometer.

When the optical axis and the magnetic field have the same direction, transitions with $\Delta M_J = 0$ are not observed. Instead of this the sign of transitions with $\Delta M_J = \pm 1$ can be distinguished since transitions with $\Delta M_J = +1$ are only excited by σ^+-circular-polarized light and vice versa.

A plane polarized wave of light can be imagined as a superposition of a σ^+-polarized and a σ^--polarized light wave with equal intensities and a fixed phase between them (cf. fig. (2.2)). Thus, when radiation is being tuned over the dispersion curve of a transition in a paramagnetic molecule[3] that is induced by e.g. σ^+-polarized radiation the σ^--component is not affected and the phase between the two components will change. When both components are superimposed again this leads finally to a rotation of the plane of polarization (Faraday effect)[4].
The rotation can be detected easily by an analyzer placed in a crossed position behind the sample cell. This detection configuration is called Faraday-Laser Magnetic Resonance. It is shown schematically in figure 2.3. Due to the crossed polarizer in front of the detector there is (almost) no background intensity. This leads to an improved sensitivity compared with a standard intracavity absorption experiment [Hin82]. When the coaxial geometry for the magnet and the sample cell is chosen, it also becomes possible to use a longer region for the detection of the molecules which leads to an additional improvement in the sensitivity of the apparatus.

[3]The term *molecule* is used in this chapter for atoms as for molecules as well since it does not make a difference at this point.

[4]Here the absorption has obviously been neglected. When taking this effect into account, a slightly elliptically polarized lightwave is obtained [Boh89]. However, in this kind of experiment the absorption is usually so small that this effect is not observed.

2.3 Experimental Setup used in this Work

The experimental realization of the Laser Magnetic Resonance Spectrometer employed in this study is shown in figure (2.4). It has been built by Claus Pfelzer in 1991 [Pfe91].

As source of radiation, a molecular gas laser is used. The spectrometer can be equipped with a CO_2- ($900 - 990cm^{-1}$ and $1000 - 1100cm^{-1}$), an N_2O- ($910cm^{-1} - 960cm^{-1}$) [Sch00] or a CO-Laser ($1300cm^{-1} - 2100cm^{-1}$ and $2500cm^{-1} - 3500cm^{-1}$) . These lasers provide an adequate output power and a large frequency range with a reasonable small frequency bandwidth.

The laser frequency is stabilized to the top of the gain curve by a commercial lock-in stabilizer. For this, the length of the laser cavity can be changed and modulated by a piezoelectric transducer on which the end mirror is fixed.

The laser beam emerges from the grating box polarized with the electric field parallel to the table. The beam is passed on via a number of mirrors onto the first polarizer where the polarization of the laser beam is refined once more. Although the Brewster windows inside the laser cavity already polarize the beam quite well, the ratio of $\frac{I_\perp}{I_\parallel}$ can be improved down to $\approx 10^{-5}$ in this way [Sch96].

Having passed the first polarizer, the light enters the sample cell which is placed concentrically inside the bore tube of a superconducting solenoid which provides a magnetic flux of up to $5T$. For a typical tuning rate of about $15\frac{MHz}{mT} \equiv 0.5 \cdot 10^{-3}\frac{cm^{-1}}{mT}$ this gives a range of about $2.5cm^{-1}$. The field is homogeneous[5] in a region of about $200mm$ from the central axis of the magnet. Since the Faraday rotation is of the order of $10^{-4}\,^\circ$, it is necessary to employ effect modulation in order to detect the transitions. For this purpose, another solenoid is fixed concentrically within the superconducting magnet. This solenoid serves as a modulation coil giving a field amplitude of up to $30mT_{pp}$ at a modulation frequency of $7kHz$. The length of the modulation coil does not exceed the homogeneous region since a longer modulated area would lead to an additional broadening of the signals.

The sample cell is about $800mm$ long and consists of Pyrex glass. The inner diameter is about $13mm$. Due to the high reactivity of radicals it is necessary to produce the radicals continuously and directly inside the detection zone. Therefore several inlets for the different precursors and an

[5] i.e. homogeneous within 0.1%

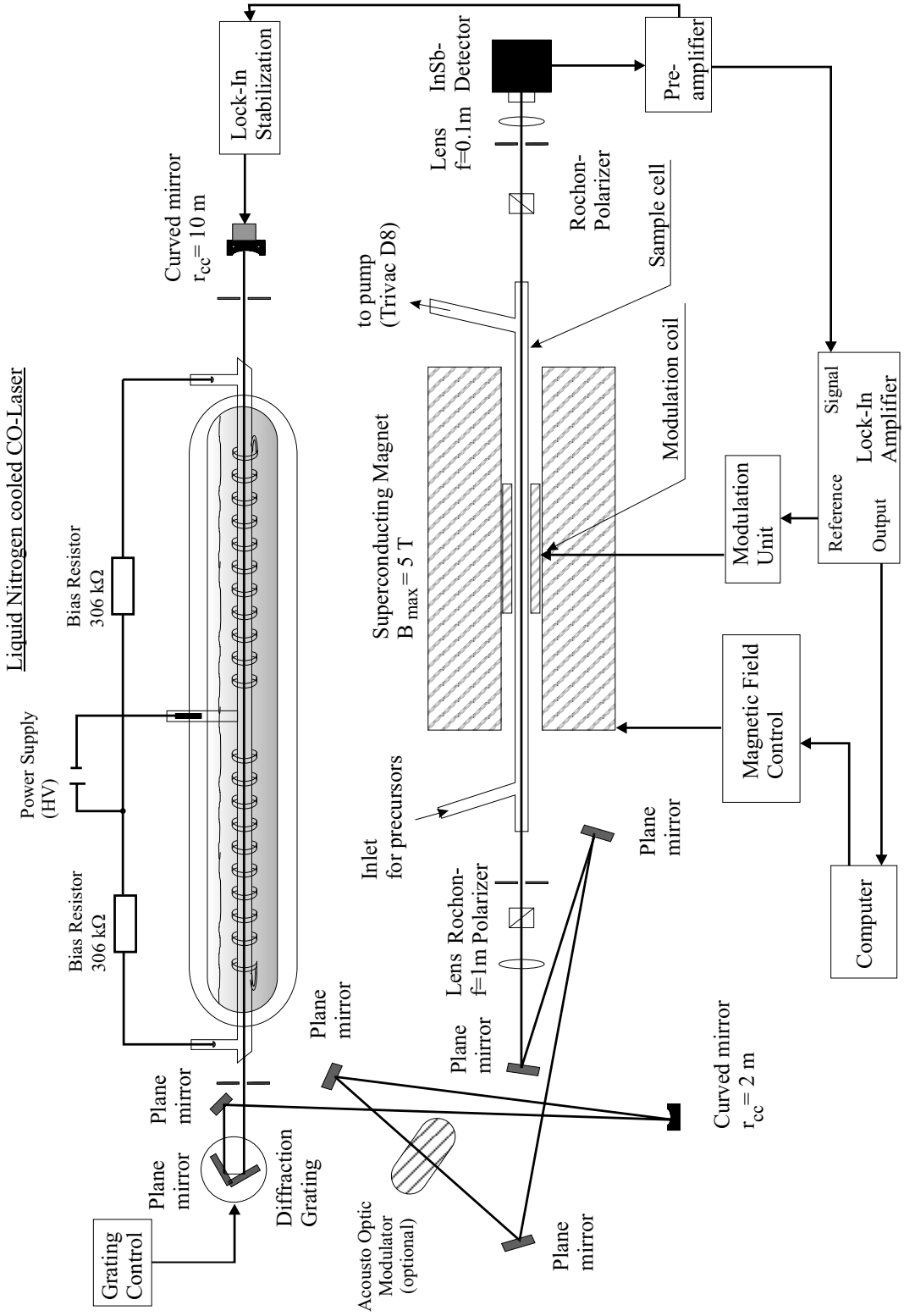

Figure 2.4: General Overview of the Faraday Laser Magnetic Resonance Spectrometer used for this study. The AOM is shown although it is only installed when measuring the tuning rate.

outlet to a pump are provided. The production itself is achieved by passing a DC glow discharge through the cell containing a mixture of the different precursors and helium. The details of the production of the different species are given in the corresponding chapters later in this thesis.

Directly behind the sample cell, a Rochon prism is placed. It serves as analyzer for the Faraday rotation and is opened by about $1-2^\circ$ with respect to the crossed position so that the laser noise and the noise of the detector are about equal.

From here the light passes on to the detector. In this study, an InSb photodiode detector was used. Since the active area of the detector is just $1mm^2$ wide a lens of focal length $100mm$ was used to focus the laser beam onto the photosensitive element.

When the setup is supplemented with an Acousto Optic Modulator the measurement of tuning rates becomes possible [Bac88]. In such a device the frequency of the laser light can be shifted by several $10MHz$. This shift in the laser frequency is translated into a small shift of the spectrum with regard to the magnetic field. Thus it is possible to measure the tuning rate $\frac{\Delta\nu}{\Delta B}$ of a particular signal. This provides also information about the relative position of the laser frequency and the transition frequency of the molecule. The AOM used during this study provides a frequency shift of $90MHz$ which corresponds approximately to half a Doppler linewidth under the experimental conditions.

2.4 The CO- and the CO-$v=(1\rightarrow 0)$-Laser

Only two of the various available radiation sources have been used during the work presented in this thesis. These are the ”normal” CO-Laser and the CO-$v=(1\rightarrow 0)$-Laser. Since they have been described very well in literature (e.g. [Urb87, Urb90, Geo90, Geo93, Bre98]) only a brief description is given here.

The active medium of a CO-Laser is a plasma produced by a DC-glow discharge through a mixture of He, N_2, O_2 and CO. The CO molecules are excited either directly by collisions with free electrons or by vibration-vibration energy transfer. The second process can take place between a nitrogen and a carbon monoxide molecule since the potential curve of both molecules is very similar. VV-transfer may also take place in a collision between two carbon monoxide molecules. In this case the transfer of en-

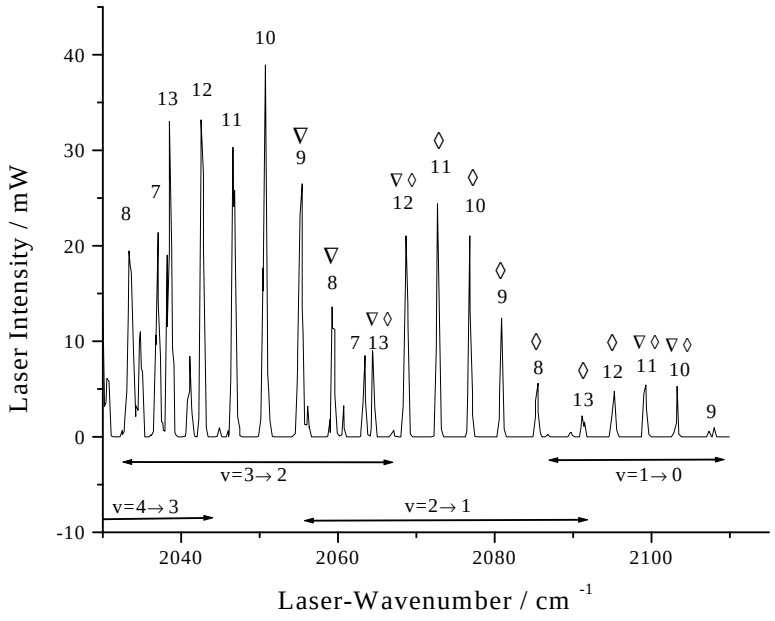

Figure 2.5: Spectrum of the CO laser around $2000cm^{-1}$ (from [Bre98])

ergy is based on the anharmonicity of the potential curve of CO. This so-called anharmonic or Treanor-pumping strongly favors the excitation of CO-molecules into higher vibrational levels.

Due to these pumping processes it is possible to achieve lasing action on ro-vibrational P-branch transitions with $J'' \approx 5 - 17$ and $v'' \approx 2 - 35$. The maximum output power is typically of the order of $100mW$ to $\leq 1W$ when working with a single mode.

Whereas the CO-Laser resembles a four-level system, the CO-$v = (1 \rightarrow 0)$-Laser resembles a three state system with an inherently small gain. Here the Treanor-pumping strongly disturbs the lasing process by either transferring molecules from the upper laser level into higher levels or by short-circuiting the laser transition.

For this reason the concentration of CO present in the plasma has to be reduced strongly which in turn reduces the possible gain. Hence the output power of this laser is reduced to less than $10mW$ and only the transitions with $J'' = 7 - 14$ have been observed [Geo93].

As is obvious from the pumping processes involved, the transition from the "normal" CO-Laser to the CO-$v = (1 \rightarrow 0)$-Laser is not a sharp one. The first sign of a change in the nature of the excitation processes can already be observed when working with the $v = 3 \rightarrow 2$ and $v = 2 \rightarrow 1$ band. The gain

becomes very weak and very low losses of the laser cavity are necessary in order to get the laser working at all.

Overall it is possible to cover a range of $\approx 1300cm^{-1} - 2100cm^{-1}$. For the lower vibrational branches the gap between adjacent laser lines is limited by the rotational constant of CO ($2B_e = 3,86cm^{-1}$); this is reduced to about $2cm^{-1}$ on average for the higher vibrational branches. This is caused by the overlap between adjacent vibrational branches. Around $2000cm^{-1}$ the vibrational branches cease to overlap.

A typical spectrum of the region relevant for the study presented here is shown in figure (2.5). The laser lines used for the experiment on atomic iodine are indicated by a triangle $\bigtriangledown$. The lines on which iodine monoxide was observed are marked by a diamond $\diamond$.

2.5 Uncertainty of the Apparatus

The accuracy of a measurement depends on several factors:

1. the stability of the laser frequency

   In previous studies (e.g. [Bre98]) the uncertainty of the laser frequency was found to be about 7 to $10MHz$. This accuracy itself depends mainly on the ability of the user to prevent the laser from multi-mode lasing since the stabilizer will have difficulty finding the optimum gain when several minima are present in the gain profile. In the same way this uncertainty is influenced by the finesse of the resonator since a higher finesse leads to a steeper line profile thus giving a better signal for the lock-in stabilizer in turn.

2. the homogenity of the magnetic field

   The homogenity of the magnet has been determined by C. Pfelzer [Pfe91] to be within 0.1% over a region of $200mm$ in length and $10mm$ in diameter in the middle of the magnet. Thus it can be assumed that the magnetic field at a certain position in the detection zone deviates by no more than $5mT$ from the measured field.

3. the co-axial arrangement of the laser beam and the magnetic field

   Assuming that the laser beam and the axis of the magnet can be arranged to coincide within 1° we can estimate this error to be within $0.8mT$.

4. the accuracy of the resistor used to measure the current through the solenoid and its calibration

   The resistor used for measuring the current through the solenoid is watercooled. Therefore it is not necessary to take temperature dependence into account. The total accuracy of the resistor is of no interest since any error will be cancelled by the calibration process. The calibration is done using an NMR probe and its accuracy can be estimated to be within $0.9mT$

5. the errors in determining the signal position from the recorded spectrum

   Here the error depends strongly on the particular signal itself. Since the error of the transition frequency is just the product of the tuning rate and the error in the magnetic field position, the error of a sharp, fast tuning signal is larger than that of a broad and slow tuning one. Irrespective of this, the read-out error in terms of the magnetic flux can be estimated for an unblended line to be less than $0.5mT$

Some of the errors appear as errors in the laser frequency while others appear as errors in the magnetic field. Therefore the total accuracy of a particular signal depends finally on its tuning rate. If we assume a typical tuning rate of $\approx 15\frac{MHz}{mT}$, we get a total accuracy of:

$$\Delta\mathbf{B} = \sqrt{\left(\left(\frac{\partial\nu}{\partial B}\right)^{-1} \times \Delta\nu\right)^2 + (\Delta B)^2_{inhomogen} + \ldots} \approx 5.2mT \quad (2.3)$$

since the above mentioned errors are statistically independent. In terms of frequency or wavenumber, this error corresponds to $\approx\ 78MHz$ or $0.0026cm^{-1}$ respectively. Obviously, this number resembles an upper limit of the resolution of the setup. As can be seen from above, the real error depends largely on the magnetic field at which the resonance occurs[6].

[6] cf. also section 3.4.3

Chapter 3

Spectroscopy of excited states in iodine atoms

During the first scans of the search for iodine monoxide (cf. chapter 4) some very strong signals showing the characteristic hyperfine pattern of iodine turned up. Quickly it became clear that this spectrum originated not from IO but from excited states of atomic iodine.
At first sight, an analysis of the data seemed to be straightforward because a similar investigation for atomic chlorine had already been carried out by Elizabeth R. Comben in 1986 [Com86]. In the course of this it turned out that the theoretical model used by her was too simple for the interpretation of the iodine data. Therefore a more sophisticated model had to be developed.

In the first section of this chapter, a short review of the current knowledge about iodine is given. It is followed by a description of the setup of the sample cell and a brief description of the experimental details. The next section develops the quantum mechanical description of single atoms. After this, the analysis of the data is described in detail. The chapter ends with a brief summary of the obtained results.

3.1 Previous investigations

Iodine has been the object of several previous investigations (e.g. [Mur58, Kie59, Mar60]). A first collection of these results was published by C. Moore [Moo71] in 1949. In 1961, L. Minnhagen has extended these results in a concise form [Min61]. From combination differences of optical measurements he obtained a very complete term scheme for the $^3P_2$ core

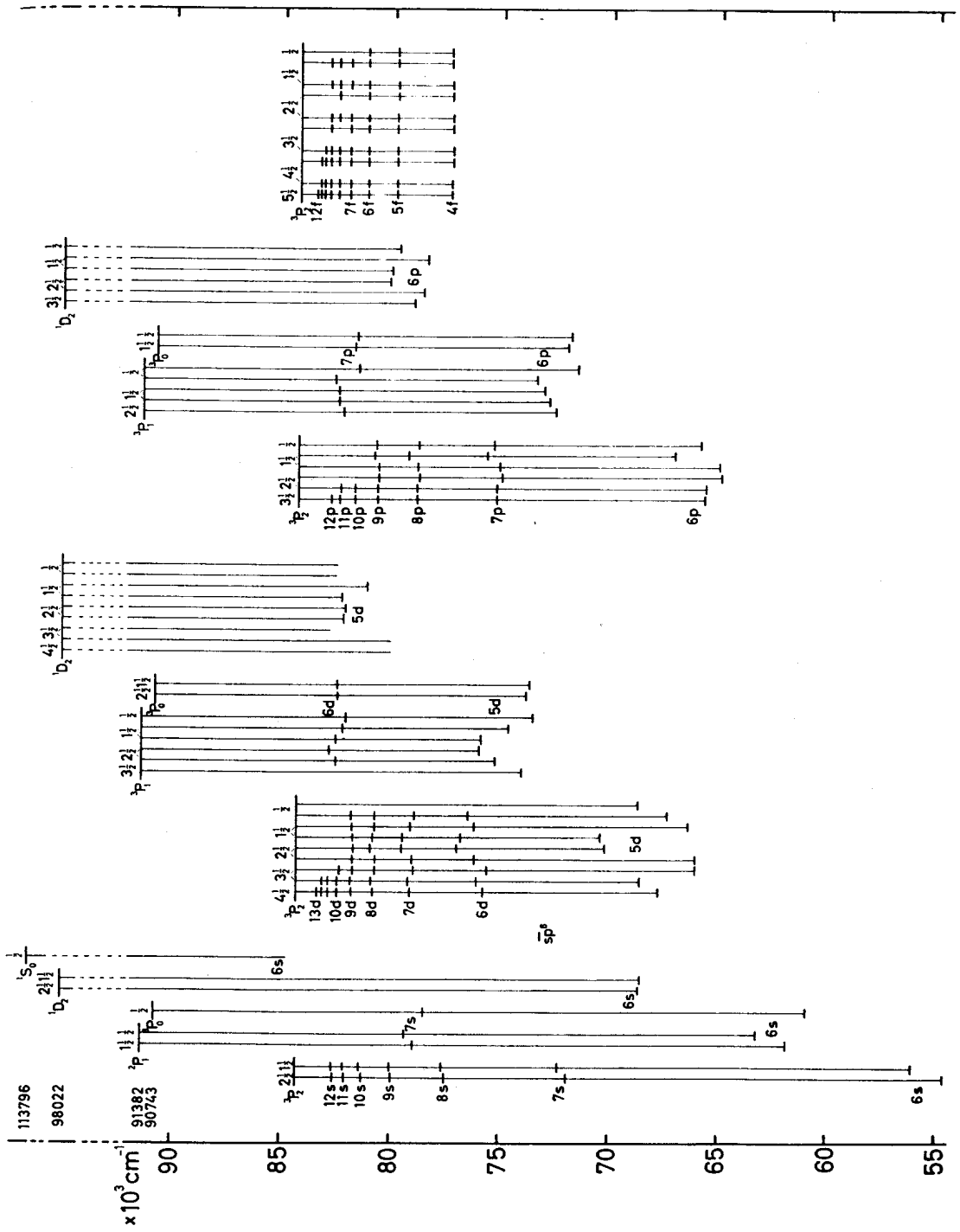

Figure 3.1: Energy terms of iodine atoms (from [Min61])

of I^*. Much less is known for the excited core states ${}^3P_{1,0}$,${}^1D_2$ and ${}^1S_0$. The term scheme as it can be found in [Min61] is printed in figure (3.1). In 1970, a first investigation in the mid-infrared has been carried out by C. J. Humphreys *et al.* [Hum71]. It was followed by several further investigations [LK75, Mor75, Bie01].

The first Laser Magnetic Resonance spectra have been recorded by Eberhard Bachem in 1988 [Bac88]. During the search for spectra of HI^+, he found accidentally some spectra that were identified to originate from atomic iodine. An analysis of these signals was not performed.

3.2 Experimental Details

The iodine atoms were produced and excited in a DC glow discharge through a mixture of helium and iodine vapor. As shown in figure (3.2) iodine crystals were placed upon a stainless-steel tube concentrically fixed inside the absorption cell. Due to ion bombardment, the glow discharge heats the tube slightly and evaporates the iodine. The vapor above the crystal surface is then transported into the discharge by a continuous stream of helium just in front of the detection zone. Here the I_2 molecules are split into single atoms in collisions with free electrons and ions inside the plasma. The surplus energy leaves some of the atoms in excited states.

This setup inherently leads to the disadvantage that it becomes impossible to determine the partial pressure of iodine. Instead the concentration of iodine present in the discharge depends on

- the temperature of the crystals,
- the flow of helium over the crystals,
- the area of the surface of the iodine crystals.

Although it would be much more convenient to evaporate the iodine outside the discharge cell, it was found that this is quite difficult to achieve. The iodine tends to condense at cold parts of the tubing wall so that it becomes necessary to heat the whole tubing. Conventionally, heating tape made from a wire containing nickel is used for this purpose. Due to the strong magnetic field present, it is impossible to use such a tape here. Instead of this it was tried to use a copper wire that was wound around the glassware in a bifilar manor for heating. A variable transformer provided the necessary current,

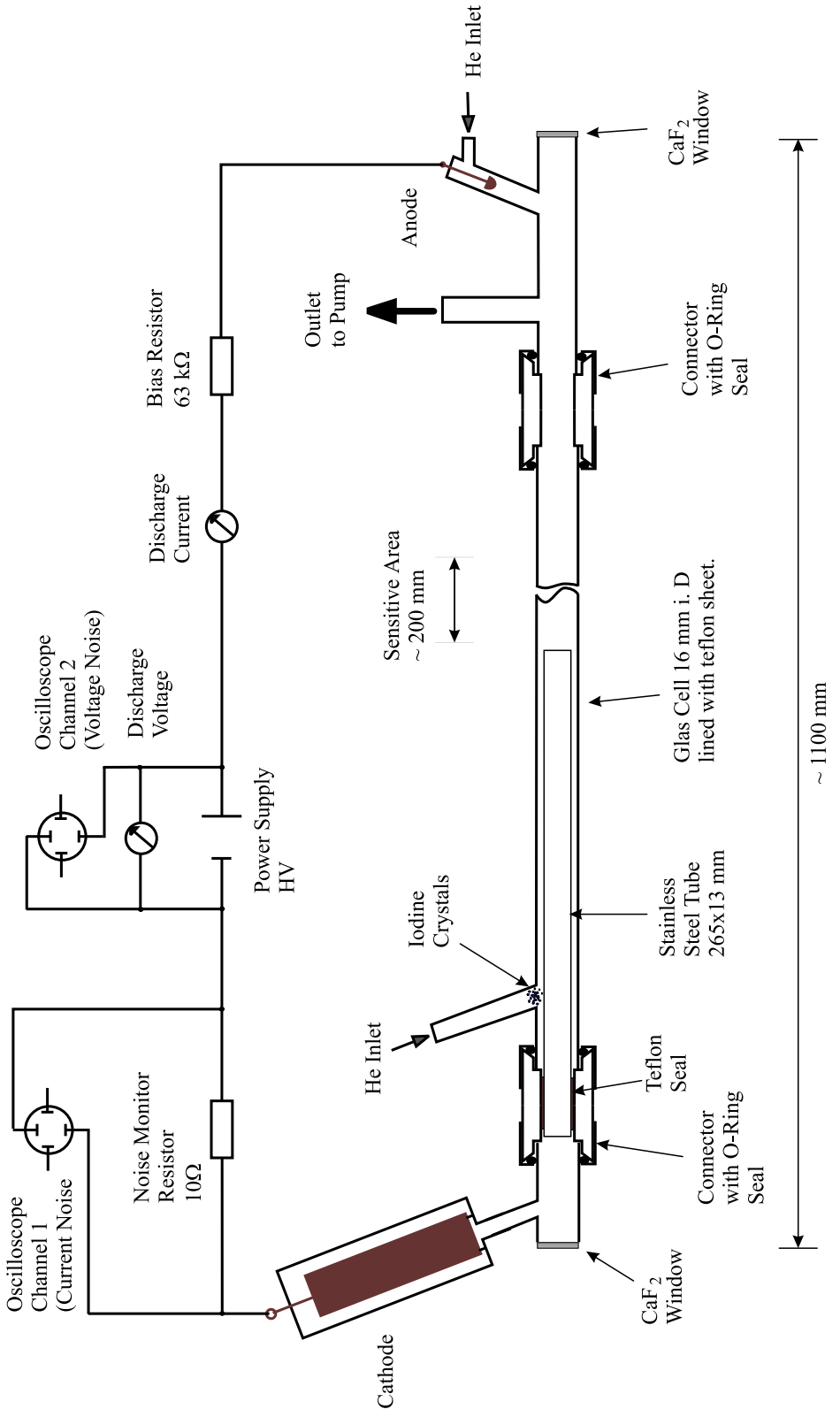

Figure 3.2: The setup of the sample cell and glow discharge used for the excitation of single atoms of iodine.

but even this was not sufficient for heating the glass because of unavoidable gaps between the single lines of wire at the bent parts of the glassware.

Finally, heating was just provided along the wall of the absorption cell along the metal tube in order to avoid a re-condensation of the iodine vapor before it reached the discharge. It was decided to bear with the disadvantages of this setup, since the signals were quite intense.

As an indicator for the amount of iodine present the chemiluminescence of the discharge plasma was found to be very useful. A bright yellow-brownish color was taken as a sign for the presence and the excitation of iodine. Furthermore the discharge voltage showed a rise of several hundred volts[1] when the iodine was transported into the discharge by the helium stream. The total pressure in the plasma was kept at $4hPa$.

The helium served not only as a carrier of the discharge but was also used for purging the electrodes. It was found that the noise of the discharge increased significantly when the iodine glow extended towards the anode.

Transitions were observed on six laser lines between $2056cm^{-1}$ and 2103 cm^{-1}. The resonances on the laser lines $2P_9$, $2P_8$, $1P_{13}$ and $1P_{12}$ have been ascribed to iodine atoms. First of all, the hyperfine structure occurs as a sextet as expected for a single iodine atom with the nuclear spin $I = \frac{5}{2}$. Furthermore the signals appear as well in a discharge through pure iodine vapor so that no other atom can be bound to the single iodine atom.

Differently, the signals on the $0P_{11}$ and $0P_{10}$ have been observed during experiments on IO so that in addition to iodine and helium, oxygen was also present. No attempt has been made to record these spectra without oxygen present since the used laser lines are very weak and the IO experiment had priority over the iodine atoms. Some of these signals have to be ascribed to iodine atoms since they show the same hyperfine structure and look very similar to the observations on the other laser lines[2].

3.3 Theoretical Description

3.3.1 Terms arising from the electronic configuration

The observed transitions take place between different excited electronic states of the atom. It is therefore necessary to understand how the structure of these states arises. When neglecting the spin-orbit and the hyperfine in-

[1] e.g. $4.3kV$ to $6.0kV$, depending on the iodine concentration.

[2] See also subsection 3.4.6 on pages 66ff.

teraction, the hamilton operator for any atom can be given by (cf. [Con35]):

$$\mathcal{H} = \sum_{i=1}^{N} \left(\frac{1}{2\mu} \mathbf{p}_i^2 - \frac{Ze^2}{r_i} \right) \tag{3.1}$$

$$+ \sum_{i,j>i}^{N} \frac{e^2}{r_{ij}}, \tag{3.2}$$

where μ is the reduced mass of the electron-nucleus system, $\mathbf{p}_i$ is the linear momentum of the i-th electron, e is the electric charge of an electron and Z the number of charges of the nucleus. r_i is used for the distance between the electron $\#i$ and the nucleus, while r_{ij} is the distance between two electrons $\#i$ and $\#j$.

This hamiltonian is not separable in the different variables because of the terms (3.2) that represent the mutual repulsion of the electrons. In order to deal with this problem, E. U. Condon and G. H. Shortley have described a way to simplify the hamiltonian by using the central field approximation [Con35].

In this approximation it is assumed that the major effect of the repulsion term consists in shielding the nuclear charge seen by a particular electron. In other words, the i-th electron sees the potential of the nucleus which is isotropically reduced by its fellow electrons. This reduction to spherical symmetry now allows the separation of the variables so that a solution of the Schr¨odinger equation is much simplified.

In this way, energy eigenvalues E_0 can be found, that are degenerate for a whole electron configuration. This degeneracy is lifted by the deviation of the repulsion term from the spherical symmetry which is then taken into account by means of perturbation theory. Thus the total energy of a particular state can be written as:

$$E = E_0 + \sum_{i,j<i}^{N} \left[J(i,j) - K(i,j) \right] \tag{3.3}$$

$$= E_0 + \sum_{i,j<i}^{N} \left[\sum_{\lambda=0}^{\infty} a^{\lambda}(l^i m_l^i, l^j m_l^j) F^{\lambda}(n^i l^i, n^j l^j) - \right.$$

$$\left. \delta_{s^i,s^j} \cdot \delta_{m_s^i,m_s^j} \sum_{\lambda=0}^{\infty} b^{\lambda}(l^i m_l^i, l^j m_l^j) G^{\lambda}(n^i l^i, n^j l^j) \right] \tag{3.4}$$

The second term in equation (3.3) describes the energy contribution made by the perturbation. J is the correction to the central field arising from the Coulomb energy of the electrons in the field of the nucleus[3] while K is the exchange energy between the several electrons themselves.

[3]For historical reasons it was decided to stick with the symbol J for the coulombic interaction of

What looks rather difficult in practice usually reduces to a few terms only. For the electronic configuration p^4nl^1 which is present in the halogens, N. M¨oller has derived formulas to calculate the constants d^λ and b^λ [M¨ol60].

3.3.2 Spin-Orbit interaction

The spin-orbit splitting arises from the interaction of the magnetic moment produced by the motion of the electron in the electrostatic field of the nucleus and the magnetic moment of the electron spin. As a dipole-dipole interaction it can be described in the language of spherical tensors by:

$$\mathcal{H}_{so} = \sum_{i=1}^{N} A_i \cdot T^1(\mathbf{l}_i).T^1(\mathbf{s}_i) \tag{3.5}$$

Here $\mathbf{l}_i$ and $\mathbf{s}_i$ mean the orbital and spin angular momentum of the i-th electron. The parameter A_i is specific for each electron and can be expressed as:

$$A = g_s \cdot g_l \cdot \mu_{Bohr}^2 \cdot \frac{1}{r_i^3} \tag{3.6}$$

3.3.3 Hyperfine Interactions

To describe the hyperfine structure everything arising from the presence of the nucleus is considered. These interactions involve either the nuclear spin (magnetostatic interaction) or a deviation of the electric charge density of the nucleus from spherical symmetry (electrostatic interaction).

Four different types of hyperfine interactions can be distinguished:

- orbital hyperfine interaction

  This interaction arises between the magnetic moment of the nucleus and the magnetic moment produced by the motion of the electrons about the nucleus. Its interaction energy can be expressed analogous to the classical interaction:

  $$\mathcal{H}_{hf}^{orb} = g_l g_I \mu_{Bohr} \mu_{nuc} \cdot \sum_{i=1}^{N} \frac{1}{r_i^3} \cdot T^1(\mathbf{I}).T^1(\mathbf{l}_i) \tag{3.7}$$

  μ_{Bohr} and μ_{nuc} are the electron and nuclear magneton while g_l and g_I are their corresponding g-factors. The interaction drops with r^{-3}

the electrons introduced by Condon and Shortley. Throughout the rest of this thesis this letter will be used for the total angular quantum number.

so that electrons with a higher principal quantum number quickly become negligible. This is important for the interpretation of the spectra of Rydberg states where the hyperfine structure arises almost solely from the hyperfine interaction of the electron core (i.e. all electrons aside of the excited one).

- Fermi-contact interaction

  This interaction has no classical analogue and it is not easy to provide an intuitive picture of it. It arises from the interaction of the nuclear and the electron spin at the position of the nucleus. Accordingly it can be written as:

$$\mathcal{H}_{hf}^{fc} = \frac{8\pi}{3} \cdot g_s g_I \mu_{Bohr} \mu_{nuc} \cdot \sum_{i=1}^{N} \delta(\mathbf{r}_i) T^1(\mathbf{I}).T^1(\mathbf{s}_i) \qquad (3.8)$$

  g_s is the spin g-factor for free electrons. Relativistic corrections due to the potential of the nucleus are rather small and can be neglected in the present context. The δ-distribution represents here the expectation value of finding the electron at the position of the nucleus.

- Anisotropic interaction

  The interaction of the nuclear spin and the electron spin over a certain distance depends also on the angle between those two magnetic dipoles. The derivation of this effect follows in the same way as for the classical analogue and just inserts the appropriate tensor operators in the end. Since in contrast to the classical picture the position of the electron is not known, it becomes necessary to take the spin density of the electron into account. This is done by taking the tensor product $T^1(\mathbf{s}, C^2)$ of the electron spin s and the modified spherical harmonic C^2 that describes the angular dependence of the wavefunction of the electron. In this way one gets the contribution by the anisotropic interaction to be:

$$\mathcal{H}_{hf}^{aniso} = g_s g_I \mu_{Bohr} \mu_{nuc} \sum_{i=1}^{N} \sqrt{10} \cdot \frac{1}{r_i^3} \cdot T^1(\mathbf{I}).T^1(\mathbf{s}_i, C_i^2) \qquad (3.9)$$

- Electric Quadrupole Hyperfine Interaction

  The charge density of a nucleus with a spin $I \geq 1$ is usually not spherical anymore. In the proximity of the nucleus the electrons therefore

move in an electric field that deviates from the field produced by a point charge. This deviation can be taken into account by developing the charge density of the nucleus into a series of spherical harmonics. The coefficients of this series are called the electrostatic moments of the charge distribution.

The interaction between the electrons and such electrostatic moments leads to a small splitting of the different z-components of the total angular momentum $\mathbf{J}$. In spectroscopic experiments under high resolution the splitting caused in this way can be determined and thus it becomes possible to derive information on the geometry of the nucleus.

Since the nucleus contains only positively charged particles, the electric dipole moment of the nucleus vanishes. Instead the first moment not to vanish is the electric quadrupole moment. Its interaction can be described by the hamiltonian:

$$\mathcal{H}_{hf}^{quad} = -e \cdot T^2(\mathbf{Q}).T^2(\nabla\mathbf{E}) \tag{3.10}$$

Here $eT^2(\mathbf{Q}) = \sum_p e_p r_p^2 \mathbf{C}^2(\theta_p, \phi_{,p})$ is the quadrupole tensor describing the geometrical distribution of the protons p inside the nucleus. $T^2(\nabla\mathbf{E}) = -\sum_i \frac{e_i}{r_i^{-3}} \mathbf{C}^2(\theta_i, \phi_i)$ is the tensor describing the gradient of the electric field seen by the electrons. The sum runs over all protons and electrons and e_i is correspondingly the positive or the negative elementary charge.

3.3.4 Zeeman-Interaction

When an external magnetic field $\mathbf{B}$ is applied to a quantum mechanical system with a non-vanishing total angular momentum $\mathbf{J}$, the system shows the Zeeman effect. This means that the degeneracy between different $M_{\mathbf{J}}$-components is lifted. The energy of the states is changed by the additional contribution arising from the interaction between the magnetic field and the different magnetic moments present. These magnetic moments arise from their motion about the nucleus of the atom and from the spin of the electrons. Therefore this interaction can be written as:

$$\mathcal{H}_{\mathbf{B}} = \sum_{i=1}^{N} \mu_{Bohr} \cdot T^1(\mathbf{B}).\left(g_s^i T^1(\mathbf{s}_i) + g_l^i T^1(\mathbf{l}_i)\right) \tag{3.11}$$

3.3.5 The total Hamiltonian

Collecting the different parts from the previous paragraphs, one obtains for the total hamiltonian:

$$\begin{aligned}
\mathcal{H} &= \mathcal{H}_{config} + \mathcal{H}_{so} + \mathcal{H}_{hf}^{dip} + \mathcal{H}_{hf}^{fc} + \mathcal{H}_{hf}^{aniso} + \mathcal{H}_{hf}^{quad} + \mathcal{H}_{\mathbf{B}} \\
&= E_0 + \sum_{i,j<i}^{N'} \left[\sum_{\lambda=0}^{\infty} a^{\lambda}(l^i m_l^i, l^j m_l^j) F^{\lambda}(n^i l^i, n^j l^j) - \right. \\
&\qquad \left. \delta_{s^i,s^j} \cdot \delta_{m_s^i,m_s^j} \sum_{\lambda=0}^{\infty} b^{\lambda}(l^i m_l^i, l^j m_l^j) G^{\lambda}(n^i l^i, n^j l^j) \right] \\
&\quad + \sum_{i=1}^{N} A_i \cdot T^1(\mathbf{l}_i).T^1(\mathbf{s}_i) + g_s g_I \mu_{Bohr} \mu_{nuc} \cdot \sum_{i=1}^{N} \\
&\qquad \left[\frac{1}{g_s \cdot r_i^3} \cdot T^1(\mathbf{I}).T^1(\mathbf{l}_i) + \frac{8\pi}{3} \cdot \delta(\mathbf{r}_i) T^1(\mathbf{I}).T^1(\mathbf{s}_i) \right. \\
&\qquad\qquad \left. + \sqrt{10} \cdot \frac{1}{r_i^3} \cdot T^1(\mathbf{I}).T^1(\mathbf{s}_i, C_i^2) \right] \\
&\quad + (-e) \cdot T^2(\mathbf{Q}).T^2(\nabla \mathbf{E})
\end{aligned} \tag{3.12}$$

3.3.6 Different Coupling Schemes

When calculating the eigenenergies of the above given hamiltonian, it becomes necessary to express the different quantum mechanical operators in some basis set. The sum of their matrix elements then represents the total hamiltonian. In order to calculate the eigenvalues of the system under consideration, this matrix has to be diagonalized. The unitary transformation used for this procedure then contains in its columns the eigenstates expressed as a linear combination of the prior basis vectors. In this study, three different basis sets have been used:

- LS-coupling
- JcK-s-coupled, I-decoupled basis set
- JcK-s-decoupled, I-decoupled basis set

LS-Coupling

In the LS-coupling scheme the orbital angular momenta of all electrons build a total orbital angular momentum **L**. In the same way the spin of the different electrons adds up to a total spin **S** which then in turn couples to **L** to give a total angular momentum **J** (cf. figure (3.3)).

When the nucleus of the atom possesses a spin angular momentum **I** of its own, this couples to **J** to give a resultant **F**. Since the interaction between both angular momenta is typically $\leq 0.1cm^{-1}$ they are easily decoupled when an outer magnetic field is applied. In this case, both angular momenta are precessing around the magnetic field independent of each other. Therefore both will be space-quantized separately along this axis.

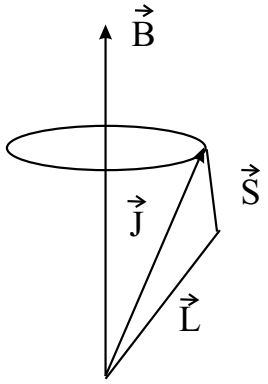

Figure 3.3: Vector model of the different angular momenta in an LS-coupled scheme.

Thus, the basis set used for describing such states is given by:

$$|(LS)J, M_{\mathbf{J}} > \otimes |I, M_{\mathbf{I}} >$$

This coupling scheme is realized only in very light atoms with a small number of electrons. Chlorine with its seventeen electrons is already one of the cases where this coupling scheme still holds for the low lying electronic states while it ceases to be an adequate description for states of higher energies.

Since the electrons are modelled as a whole rather than individually, the individual parameters in the hamiltonian are replaced by a common average instead. In this way the sums over the single electrons vanish in the hamiltonian and equation (3.12) becomes:

$$\begin{aligned}
\mathcal{H}_{LS} \;=\; & \delta_{LL'}\delta_{SS'}\delta_{JJ'}\delta_{M_{\mathbf{J}}M'_{\mathbf{J}}} \sum_{\lambda=0}^{\infty} f_\lambda F^\lambda + (-1)^S g_\lambda G^\lambda \\
& + A \cdot T^1(\mathbf{L}).T^1(\mathbf{S}) \\
& + g_s g_{\mathbf{I}} \mu_{Bohr} \mu_{nuc} \cdot \\
& \quad \Big(a \cdot T^1(\mathbf{I}).T^1(\mathbf{L}) + b \cdot T^1(\mathbf{I}).T^1(\mathbf{S}) + c \cdot T^1(\mathbf{I}).T^1(\mathbf{S}, C^2) \Big) \\
& + d \cdot \mathsf{V}(T^2(\mathbf{Q}), T^2(\nabla \mathbf{E})) \\
& + \mu_{Bohr} \cdot T^1(\mathbf{B}). \Big(g_s T^1(\mathbf{S}) + g_l T^1(\mathbf{L}) \Big)
\end{aligned} \tag{3.13}$$

As above, the F^λ and G^λ are the direct and exchange integrals from section 3.3.1. Their factors a^λ and b^λ have been renamed to f_λ and g_λ, respectively, to emphasize that the sum over the different electrons has now been absorbed in them. The constant A is the common spin-orbit coupling constant

for all electrons. The same applies to the constants g_s and g_l. The hyperfine constants a to c are defined now as follows:

$$a = g_I \mu_{Bohr} \mu_{nuc} \cdot \left\langle \frac{1}{r^3} \right\rangle \tag{3.14}$$

$$b = \frac{8\pi}{3} \cdot g_s g_I \mu_{Bohr} \mu_{nuc} \cdot |\Psi(r=0)|^2 \tag{3.15}$$

$$c = g_s g_I \mu_{Bohr} \mu_{nuc} \cdot \sqrt{10} \cdot \left\langle \frac{1}{r^3} \right\rangle \tag{3.16}$$

In the definition of b, the expectation value $|\Psi(r=0)|^2$ replaces now the δ distribution in the hamiltonian (3.8). d is used for the nuclear quadrupole constant and is defined as:

$$d := < I \| T^2(\mathbf{Q}) \| I > \cdot < L \| T^2(\nabla \mathbf{E}) \| L > \tag{3.17}$$

The symbol $\mathsf{V}(T^2(\mathbf{Q}), T^2(\nabla \mathbf{E}))$ absorbs all necessary vector coupling coefficients and the elementary charges. In literature (eg. [Abr70, LK75, Mor75, Bie01]) one often finds the quadrupole constant $b_{\mathbf{J}}$ which relates to d as:

$$b_{\mathbf{J}} = (-1)^{L+S+J+1} \cdot 2 \cdot \sqrt{\frac{(2J-1)(2J)(2J+1)}{(2J+2)(2J+3)}} \cdot \begin{pmatrix} I & 2 & I \\ I & 0 & -I \end{pmatrix} \cdot \begin{Bmatrix} S & L & J \\ 2 & J & L \end{Bmatrix} \cdot d \tag{3.18}$$

From the expressions above, it can be seen that a to c are expected to be positive quantities while the nuclear quadrupole constant d can have both signs. In the case of a negative sign, $d < 0$, the geometry of the nuclear charge distribution is oblate, in the opposite case prolate [Kop56].

The matrix elements in this coupling scheme have been worked out by previous authors (e.g. [M¨ol60, Con35]). For clarity, they are repeated in appendix A.1.

Electric dipole transitions between states close to this coupling scheme have to obey the following selection rules:

$$\begin{aligned}
\Delta(L'', L') &= 0, \pm 1 \text{ and } L'' = 0 \not\leftrightarrow L' = 0 \\
\Delta(S'', S') &= 0 \\
\Delta(J'', J') &= 0, \pm 1 \text{ and } J'' = 0 \not\leftrightarrow J' = 0 \\
\Delta(M''_{\mathbf{J}}, M'_{\mathbf{J}}) &= 0, \pm 1 \\
\Delta(I'', I') &= 0 \\
\Delta(M''_{\mathbf{I}}, M'_{\mathbf{I}}) &= 0
\end{aligned}$$

J_cK-coupled, s-coupled, I-decoupled Scheme

When the excitation of an electron leaves a partially filled shell behind, another coupling scheme becomes more apropriate to describe the situation: In the case of J_cK-coupling the inner electrons (i.e. the so-called core) are treated by LS-coupling while the excited electron is dealt with separately. This coupling is appropriate for states with Rydberg character.

Now the total angular momentum $\mathbf{J}_c$ of the core electrons couples to the orbital angular momentum $\mathbf{l}$ of the excited electron to give an intermediate angular momentum $\mathbf{K}$. The spin angular momentum of the excited electron, $\mathbf{s}$, then couples to $\mathbf{K}$ to give the total angular momentum $\mathbf{J}$. This situation is shown pictorially in figure (3.4). As in the case of LS-coupling the nuclear spin is easily decoupled in the presence of a magnetic field.

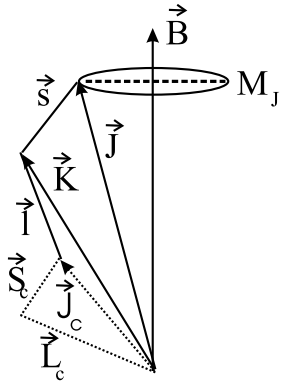

Figure 3.4: Vector model of the different angular momenta in J_cK-coupling.

Therefore the basis set used in this case is given by:

$$|(((L_c, S_c)J_c, l)K, s)J, M_{\mathbf{J}} > \otimes |I, M_{\mathbf{I}} >$$

In this picture, the hamiltonian takes a slightly different form:

$$\begin{aligned}
\mathcal{H}_{J_cK} \;=\; & \delta_{L_c'' L_c'}\delta_{S_c'' S_c'}\delta_{J_c'' J_c'}\delta_{l'' l'}\delta_{K'' K'}\delta_{s'' s'}\delta_{J'' J'}\delta_{M_{\mathbf{J}}'' M_{\mathbf{J}}'} \\
& \cdot \sum_{\lambda=0}^{\infty} f_\lambda F^\lambda + (-1)^S g_\lambda G^\lambda && (3.19)\\
& + A \cdot \Big(T^1(\mathbf{L_c}).T^1(\mathbf{S_c}) + T^1(\mathbf{l}).T^1(\mathbf{s}) \Big) && (3.20)\\
& + g_{\mathbf{I}} \mu_{Bohr} \mu_{nuc} \cdot \Big(a_c \cdot T^1(\mathbf{I}).T^1(\mathbf{L_c}) + b_c g_s \cdot T^1(\mathbf{I}).T^1(\mathbf{S_c}) \\
& \quad + c_c g_s \cdot T^1(\mathbf{I}).T^1(\mathbf{S_c}, C^2) \Big) && (3.21)\\
& + + \, d_c \cdot \mathsf{V}_c(T^2(\mathbf{Q}), T^2(\nabla \mathbf{E})) && (3.22)\\
& + \mu_{Bohr} \cdot T^1(\mathbf{B}). \\
& \quad \Big[\Big(T^1(\mathbf{S_c}) + T^1(\mathbf{s}) \Big) \cdot g_s + \Big(T^1(\mathbf{L_c}) + T^1(\mathbf{l}) \Big) \cdot g_l \Big] && (3.23)
\end{aligned}$$

At first sight, the energy of the electronic configuration (3.19) still appears to be unchanged but different expressions appear when it is expressed in the basis set explicitly. More evident is the change in the other parts of the hamiltonian. The contribution by the spin-orbit coupling (3.20) is split

into a part describing the spin-orbit coupling of the ionic core and a part describing the spin-orbit coupling for the single outer electron. The same applies to the part describing the Zeeman effect (3.23).

Due to its dependence on $< r_i^{-3} >$ and the expectation value $|\Psi_i(r = 0)|$, respectively, the hyperfine structure can be assumed to arise solely from the core electrons. For higher principal quantum numbers n of the excited electron the values of $< r_i^{-3} >$ and $|\Psi_i(r = 0)|$ drop down very quickly so that its contribution can be neglected. Thus the hyperfine constants a_c to d_c are defined now in the following way:

$$\begin{aligned} a_c &= g_I \mu_{Bohr} \mu_{nuc} \cdot \left\langle \frac{1}{r_c^3} \right\rangle \\ b_c &= \frac{8\pi}{3} \cdot g_s g_I \mu_{Bohr} \mu_{nuc} \cdot |\Psi_c(r_c = 0)| \\ c_c &= g_s g_I \mu_{Bohr} \mu_{nuc} \cdot \sqrt{10} \cdot \left\langle \frac{1}{r_c^3} \right\rangle \end{aligned}$$

where the index "c" symbolizes the restriction to the core electrons. For the electric quadrupole term, the different treatment in contrast to the hamiltonian (3.10)/(3.12) is not obvious from the formula itself but again manifests itself when calculating the matrix elements in this basis set. Similar to the treatment in LS coupling, d_c is defined as:

$$d_c := < I \| T^2(\mathbf{Q}) \| I > \cdot < L_c \| T^2(\nabla \mathbf{E}) \| L_c > \tag{3.24}$$

The relation to the constant $b_{\mathbf{J}}$ is given by equation 3.18 where the quantum numbers L, S and J are replaced by the corresponding quantum numbers of the core configuration, L_c, S_c and J_c.

The matrix elements in this basis set have been derived and are given in appendix A.2. As before in the case of LS coupling, the different parameters are treated as common to all electrons with the exception of the hyperfine parameters as described above. When evaluating the transition matrix for electric dipole transitions between states described in this basis set, one obtains the following selection rules:

$$\begin{aligned} \Delta(L_c'', L_c') &= 0 \\ \Delta(S_c'', S_c') &= 0 \\ \Delta(J_c'', J_c') &= 0 \\ \Delta(l'', l') &= 0, \pm 1 \text{ and } l'' = 0 \not\leftrightarrow l' = 0 \\ \Delta(K'', K') &= 0, \pm 1 \text{ and } K'' = 0 \not\leftrightarrow K' = 0 \\ \Delta(J'', J') &= 0, \pm 1 \text{ and } J'' = 0 \not\leftrightarrow J' = 0 \end{aligned}$$

$$\begin{aligned}\Delta(M''_{\mathbf{J}}, M'_{\mathbf{J}}) &= 0, \pm 1 \\ \Delta(I'', I') &= 0 \\ \Delta(M''_{\mathbf{I}}, M'_{\mathbf{I}}) &= 0\end{aligned}$$

This coupling scheme was used in a simplified way by E. R. Comben [Com86] for some of the excited states of chlorine where the required information on the nature of the states was available. It is particularly useful for the description of iodine where significant departure from the behavior expected for an LS coupled system is observed for almost all of its excited states (cf. [Min61]).

J_cK-coupled, s-decoupled Scheme

When the spin-orbit interaction between the intermediate angular momentum $\mathbf{K}$ is of the same order as the Zeeman interaction, $\mathbf{K}$ and $\mathbf{s}$ start to decouple and to precess around the magnetic field separately from each other (cf. figure (3.5)). In this case the basis set used for describing the atoms is slightly different, namely:

$$|((L_c, S_c)J_c, l)K, M_{\mathbf{K}} > \otimes |s, m_{\mathbf{s}} > \otimes |I, M_{\mathbf{I}} >$$

This different basis set does not change the hamiltonian (3.19) in its appearance since it still splits the electrons into the core and the excited electron. Due to the different vector coupling coefficients the matrix elements are still changed. The elements obtained for this coupling scheme are given in appendix A.3. Due to the different coupling, the selection rules for electric dipole transitions change. They now become:

$$
\begin{aligned}
\Delta(L_c'', L_c') &= 0 \\
\Delta(S_c'', S_c') &= 0 \\
\Delta(J_c'', J_c') &= 0 \\
\Delta(l'', l') &= 0, \pm 1 \\
\text{and} \quad & l'' = 0 \not\leftrightarrow l' = 0 \\
\Delta(K'', K') &= 0, \pm 1 \\
\text{and} \quad & K'' = 0 \not\leftrightarrow K' = 0 \\
\Delta(M_{\mathbf{K}}'', M_{\mathbf{K}}') &= 0, \pm 1 \\
\Delta(s'', s') &= 0 \\
\Delta(m_{\mathbf{s}}'', m_{\mathbf{s}}') &= 0 \\
\Delta(I'', I') &= 0 \\
\Delta(M_{\mathbf{I}}'', M_{\mathbf{I}}') &= 0
\end{aligned}
$$

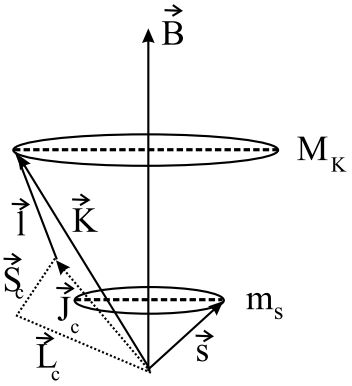

Figure 3.5: Vector model of the different angular momenta in J_cK-coupling where the electron spin of the excited electron is decoupled.

3.4 Analysis and Results

3.4.1 Determinable parameters

The model described in the previous section contains a number of parameters that are not determined by the theory itself. These parameters have to be extracted from experimental data in order to understand (and predict) the behavior of the atoms. In particular, these parameters are:

- The energy of the electronic states in the absence of an outer magnetic field:

  As described above, the zero-field energy of the different electronic states is not determined by a unique constant but by the energy of the whole electronic configuration and the different integrals F^λ and G^λ. In practice it is not possible to obtain the observations by Laser Magnetic Resonance which are required to determine these parameters. Therefore these different constants were collected into a zero-field energy difference, $\tilde{\nu}_0$, between lower and upper state.

- The spin-orbit splitting:

  When the spin-orbit coupling is strong, it becomes sometimes possible to determine the spin-orbit splitting from several separate obser-

vations of the different spin-orbit components. In the opposite case, where the spin is almost decoupled from the orbital motion of the electrons, strong perturbations are caused by avoided crossings of the different M_J-components. In general, these perturbations can be used for the determination of this constant, when the available information about the electronic configuration is precise enough.

Since in the present study of iodine, the information available is not precise enough for this purpose, this parameter had to be absorbed into $\tilde{\nu}_0$ as well.

- The electronic g-factors g_l and g_s:

  Due to the spherical symmetry, the contribution of the orbital angular momentum to the Zeeman energy has got the same M_J-dependency as the contribution by the spin angular momentum. Due to this, g_s and g_l become linearly dependent in parameter space. Thus, it becomes impossible to determine both parameters independently of each other. Therefore it is necessary to fix one of these parameters to a reasonable value and to determine the other one separately from the experimental data. Since the theoretical value for g_s is affected much less by the electronic configuration than the g_l factor, in the analysis presented here, g_s was kept at a value of 2.002.

- The hyperfine parameters a,b and c:

  Although the physical origin of the three single interactions is quite different their M_J/M_I-dependency is still the same. Therefore these parameters also become linearly dependent so that it is impossible to determine them separately from the same transition. In general, these linear combinations can be solved when the same ionic core has been observed for three different transitions. Unfortunately, since the mixing of electronic configurations does not uniformly affect the different states, this possibility is usually frustrated[4].

- The electric quadrupole parameter d:

  Provided the effect is strong enough, this parameter is determinable from the laser magnetic resonance spectrum. In particular, iodine possesses a large quadrupole constant so that this parameter can be obtained from the experimental data presented in this work. The only

[4] See also 5

limitation is that as before only a constant common to all core electrons can be obtained.

3.4.2 The software "Hamiltonian" and its test on a known transition in chlorine atoms

A software has been developed for determining these parameters from the experimental spectra via a least squares fit routine. The program is capable of using all three of the above mentioned basis sets. In particular, the basis set for upper and lower state may be different so that transitions from e.g. low lying LS-coupled states into higher excited J_cK-coupled states can be treated. For J_cK-coupled systems the splitting between different K-levels can become quite important. Therefore these properties can be fed to the software either as empirically determined separations or, where available, by means of the appropriate Coulomb and exchange integrals. In the second case, an additional fit-program has been developed for determining the necessary parameters from experimental data obtained by e.g. optical work.

To make sure that the software works well two sets of synthetic data using a linear model in LS- and J_cK-coupling have been calculated by hand. Fitting this artificial data with "Hamiltonian" yielded the expected results.

As an additional test, especially for the case of two different coupling schemes for upper and lower state, the fit of the transition from $(^3P)5p^2P_{\frac{3}{2}}$ to $(^3P_0)4d[2]_{2\frac{1}{2}}$ in chlorine observed by E. R. Comben [Com86] was repeated. This transition has been chosen since it shows a spectrum similar to the one observed on the $2P_8$ and $2P_9$ laser lines (cf. section 3.4.3) in iodine. Two of the chlorine spectra are shown in fig. (B.1) and (B.2). The signals are tabulated in appendix B.

Fitting this transition in a similar way as it was done by E. R. Comben[5], results in a set of parameters that is consistent with hers but not identical (table 3.1). Since "Hamiltonian" uses the g-factor g_l while Comben used $g_{\mathbf{J}}$ it is necessary to convert them into each other for comparison. This is done

[5]Comben did not describe which weights she used or how she treated blended lines. This makes it difficult to follow her footsteps exactly. Also the vector coupling coefficients for the hyperfine structure of the upper state vanish for $J_c = 0$. The consequences arising from this fact are described in the further text. For the present fit, $J_c = 1$ was assumed for the description of the hyperfine structure.

using the formulas [Com86]:

$$g_{\mathbf{J}} = \frac{1}{2}\left[(g_l + g_s) + (g_l - g_s)\cdot\frac{L(L+1) - S(S+1)}{J(J+1)}\right] \quad (3.25)$$

$$\begin{aligned} g_{\mathbf{J}} = {} & g_l \cdot [K(K+1) + J(J+1) - S(S+1)] \\ & \cdot\frac{[l(l+1) + K(K+1) - J_c(J_c+1)]}{4J(J+1)K(K+1)} \\ & + g_s \cdot \frac{s(s+1) + J(J+1) - K(K+1)}{2J(J+1)} \\ & + (g_l + g_s)\cdot[K(K+1) + J(J+1) - s(s+1)] \\ & \cdot\frac{[J_c(J_c+1) + K(K+1) - l(l+1)]}{8J(J+1)K(K+1)} \\ & + (g_l - g_s)\cdot[K(K+1) + J(J+1) - s(s+1)] \\ & \cdot[J_c(J_c+1) + K(K+1) - l(l+1)] \\ & \cdot\frac{[L_c(L_c+1) - S_c(S_c+1)]}{8J(J+1)K(K+1)J_c(J_c+1)} \end{aligned} \quad (3.26)$$

for LS- and J_cK-coupling, respectively.

Figure (3.6) on page 42 shows a comparison between the residuals given in [Com86] and the ones calculated by "Hamiltonian" for the signals observed on the $23P_{18}$. Data set (a) gives the values from table (3.3) of [Com86]. (b) contains the residuals calculated using the new software assuming an equal weight for all signals including the blended ones while for set (c) these signals were rejected. The reason for the observed discrepancy between Comben's fit and the new one is not clear.

However, a look into the theory developed above shows another problem with Comben's fit. All hyperfine matrix elements involving the core electrons contain the $6j$-symbol $\left\{ \begin{array}{ccc} l & J_c & K \\ 1 & K' & J_c \end{array} \right\}$. For $J_c = 0$ this matrix element vanishes so that no hyperfine structure should arise for the $(^3P_0)4d[2]_{2\frac{1}{2}}$ state. Therefore the coupling constant a' can not be determined by a fit of spectroscopic data.

This affects also the assignment of the different $M_{\mathbf{I}}$ components. The contribution to the transition energy can be written as:

$$\tilde{\nu}_{hfs} = \hat{a}' \cdot M'_{\mathbf{J}} \cdot M_{\mathbf{I}} - \hat{a}'' \cdot M''_{\mathbf{J}} \cdot M_{\mathbf{I}} \quad (3.27)$$

where the symbol $\hat{a}$ absorbs all vector coupling factors for the involved angular momenta. When $\hat{a}'$ vanishes, this equation becomes:

$$\tilde{\nu}_{hfs} = -\hat{a}'' \cdot M''_{\mathbf{J}} \cdot M_{\mathbf{I}} \quad (3.28)$$

From this we see that the quantum numbers $M_{\mathbf{I}}$ are "swapping" their order: While for $M''_{\mathbf{J}} = 1\frac{1}{2}$ the component with $M_{\mathbf{I}} = 1\frac{1}{2}$ decreases the transition

frequency, this effect is reversed for $M''_{\mathbf{J}} = -1\frac{1}{2}$. Thus, the order of the $M_{\mathbf{I}}$ is reversed as well.

Therefore a new fit was computed using the revised assignment given in table B.1. The parameters obtained by this fit are given in table 3.2. A comparison of the residuals obtained in this way with the ones given by E. R. Comben is presented in figure (3.7). (a) again gives the residuals taken from [Com86] while (b) shows the residuals obtained for the new assignment.

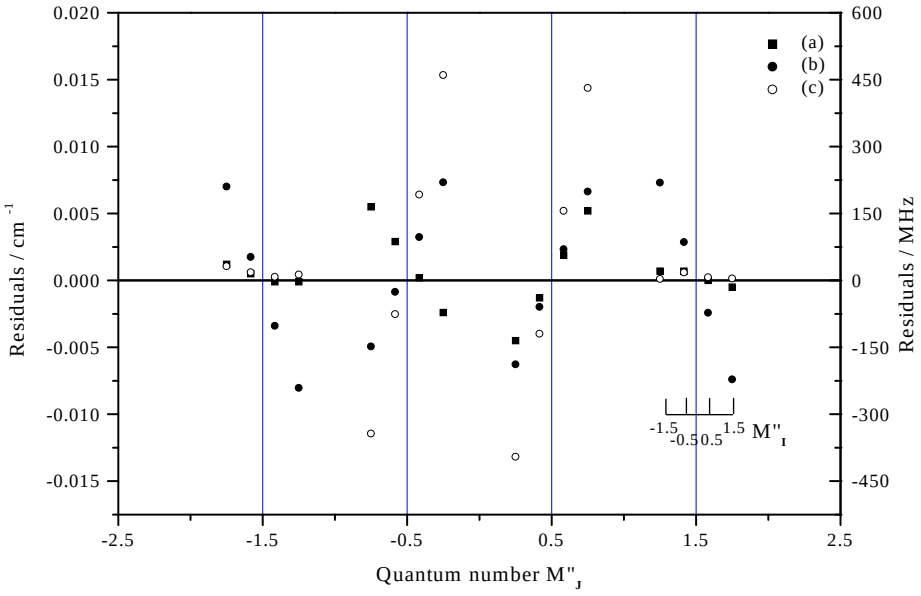

Figure 3.6: Comparison of the residuals calculated by Comben [Com86] of the observations of the test transition on the $23P_{18}$. See text for details.

Parameter	Value	Std.-Dev.	Value	Std.-Dev.	Unit
	from "Hamiltonian"		from [Com86]		
$\Delta\tilde{\nu}_0$	1494.3937	$0.64 \cdot 10^{-3}$	1494.3926	$0.4 \cdot 10^{-3}$	cm^{-1}
g'_s	2.00200	$fixed$	./.	$fixed$	
g''_s	2.00200	$fixed$	./.	$fixed$	
g'_l	0.7496	$1.5 \cdot 10^{-3}$	0.7485 [a]	$0.9 \cdot 10^{-3}$ [a]	
g''_l	0.9338	$5.3 \cdot 10^{-3}$	0.9300 [a]	$1.5 \cdot 10^{-3}$ [a]	
g'_J	1.0835 [a]	$1.0 \cdot 10^{-3}$ [a]	1.0828	$0.7 \cdot 10^{-3}$	
g''_J	1.2894 [a]	$1.5 \cdot 10^{-3}$ [a]	1.2873	$1.0 \cdot 10^{-3}$	
a'_l	$3.6 \cdot 10^{-3}$	$5.2 \cdot 10^{-3}$	$3.29 \cdot 10^{-3}$ [b]	$2.61 \cdot 10^{-3}$ [b]	cm^{-1}
a''_l	$8.2 \cdot 10^{-3}$	$0.7 \cdot 10^{-3}$	$6.94 \cdot 10^{-3}$ [c]	$0.31 \cdot 10^{-3}$ [c]	cm^{-1}
$\hat{a}'_l$ [d]	$0.3 \cdot 10^{-3}$ [b]	$0.5 \cdot 10^{-3}$ [b]	$0.29 \cdot 10^{-3}$	$0.23 \cdot 10^{-3}$	cm^{-1}
$\hat{a}''_l$ [d]	$7.2 \cdot 10^{-3}$ [c]	$0.6 \cdot 10^{-3}$ [c]	$6.12 \cdot 10^{-3}$	$0.28 \cdot 10^{-3}$	cm^{-1}
# of obs.:		62		62	
# of fitted obs.:		62		62 (?)	
# of fbated param. :		5		5	
Std.-dev. of total fit:		$5.32 \cdot 10^{-3}$		$2.88 \cdot 10^{-3}$	cm^{-1}
		$\hat{=}159.4$		$\hat{=}86.3$	MHz

[a]: Values calculated using the formulas (3.25) and (3.26) for transferring g_l to g_J and vice versa

[b]: Values calculated using the formulas from appendix A.2 and assuming a core angular momentum $J_c = 1$ since the matrix element vanishes for $J_c = 0$.

[c]: Values calculated using the formulas from appendix A.1

[d]: $\hat{a}$ are the hyperfine parameters as used in [Com86]. They are the product of a and the vector coupling coefficients that are independent of M_J and M_I and are therefore constant for the whole transition.

Table 3.1: Parameters for the test-transition $(^3P_0)4d[2]_{2\frac{1}{2}} \leftarrow (^3P)5p^2P_{\frac{3}{2}}$ of chlorine determined by a linear least-squares fit using the assignment from [Com86].

Parameter	Value	Std.-Dev.	Unit
$\Delta\tilde{\nu}_0$	1494.4911	$0.50 \cdot 10^{-3}$	cm^{-1}
g_s'	2.00200	$fixed$	
g_s''	2.00200	$fixed$	
g_l'	0.8528	$1.1 \cdot 10^{-3}$	
g_l''	0.9313	$1.7 \cdot 10^{-3}$	
g_J'	1.0835	$1.0 \cdot 10^{-3}$	
g_J''	1.2894	$1.5 \cdot 10^{-3}$	
a_l'	$not\ defined;\ fixed\ to\ zero$		
a_l''	$8.8 \cdot 10^{-3}$	$2.8 \cdot 10^{-3}$	cm^{-1}
# of obs.:	62		
# of fitted obs.:	30		
# of fbated param. :	4		
Std.-dev. of total fit:	$1.64 \cdot 10^{-3} cm^{-1}$		
	$\hat{=}49.3 MHz$		

Table 3.2: Final parameters for the test-transition $(^3P_0)4d[2]_{2\frac{1}{2}} \leftarrow (^3P)5p^2P_{\frac{3}{2}}$ of chlorine determined by a linear least-squares fit using the new assignment given in table B.1.

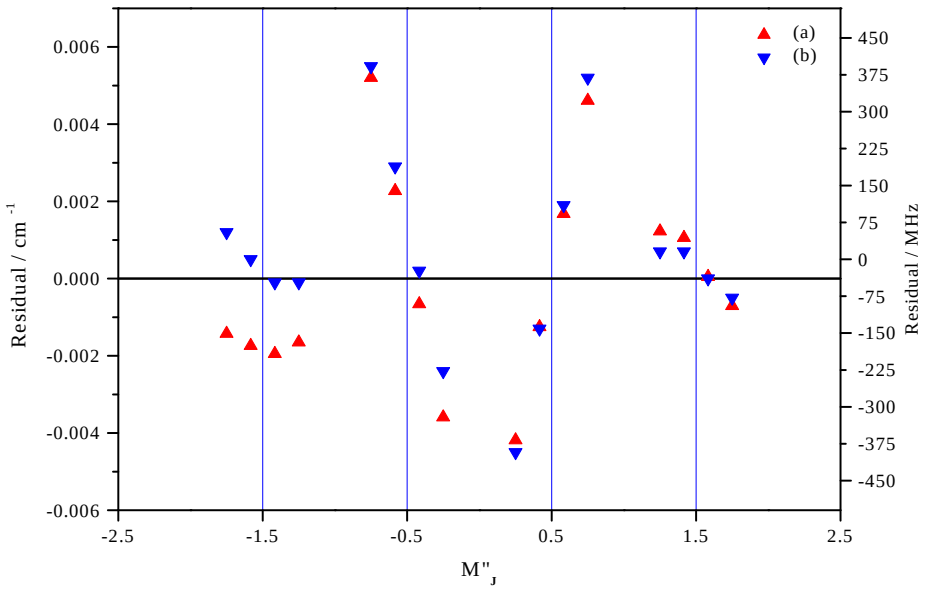

Figure 3.7: Residuals obtained with different fits of the chlorine signals observed on the $23P_{18}$. See text for details.

3.4.3 The transition $(^3P_2)9f[4]_{4\frac{1}{2}} \leftarrow (^3P_2)8d[4]_{3\frac{1}{2}}$ in I^*

Observations

This transition has been observed on two adjacent laser lines, namely the $2P_9$ at $2055.1593cm^{-1}$ (figure (3.8)) and the $2P_8$ at $2059.2090cm^{-1}$ (figure (3.9)). Due to the fairly high output power of the laser, it was possible to record frequency-shifted spectra using the acousto optic modulator. The spectra obtained in this way are shown in figures (C.1) and (C.2) of appendix C. These figures also show the unshifted spectrum as a reference.

The spectrum for the $2P_9$ line shows a very strong group of signals[6] that appear between $1.5T$ and $3.2T$. The arrows in figure (3.8) mark the positions in the spectrum where the lock-in amplifier had to be adjusted in its sensitivity due to its limited dynamic range. Later, the spectrum has been compensated for these effects so that the shown spectrum resembles the correct intensities.

As mentioned above, the group at higher fields on the $2P_9$ shows a similar collapse of the hyperfine structure as the chlorine transition used for testing purposes. The observed signals consist of a total of 8 different hyperfine patterns. A further search for signals above or below this spectrum did not show any further signals belonging to this Zeeman pattern. Therefore the number of $M_{\mathbf{J}}$ components suggests a transition with a smallest value of $J = 3\frac{1}{2}$. Furthermore, the intensity pattern suggests a transition with $\Delta J = \pm 1$ [7]. From the tuning behavior one gets the information that the zero field frequency lies above the frequency of the $2P_9$ and below that of the $2P_8$. This supports the assumption that both spectra belong together. Due to the maximum available field strength, the spectrum on the $2P_8$ shows only five of the eight possible $M_{\mathbf{J}}$ components.

A search in Minnhagen's list of energy levels [Min61] returned only the combination of the levels $(^3P_2)8d[4]_{3\frac{1}{2}}$ and $(^3P_2)9f[4]_{4\frac{1}{2}}$ with a gap of $2056.03cm^{-1}$ as possible candidates for this transition. Their termschemes are shown in figure (3.10). In the case of the $(^3P_2)9f$ state, the spin-orbit splitting is less than a wavenumber. Hence, when applying a magnetic field the spin-orbit coupling is easily decoupled and the two spin-orbit components are mixed. Therefore, this state should be described by a J_cK cou-

[6] On this laser line also another transition has been observed at about $1.0T$. This group of rather weak signals is discussed in section 3.4.6

[7] For a transition with $\Delta J = 0$ one expects the maximum intensity in the middle of the spectrum and a decrease symmetric for both wings of the spectrum (cf. section 3.4.4).

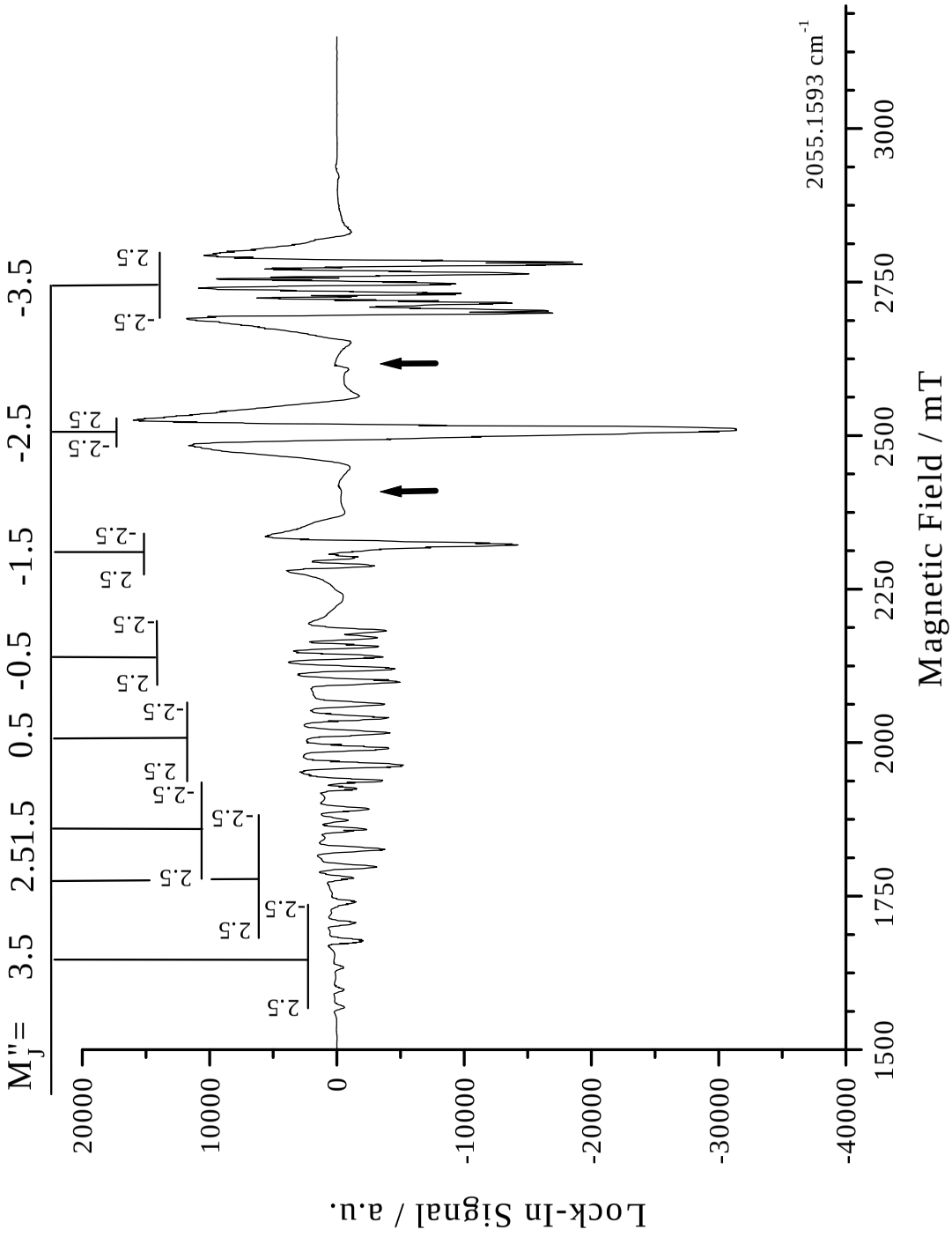

Figure 3.8: Spectrum of I* on the $2P_9$ @ $2055.1593cm^{-1}$ between $0.0T$ and $3.2T$

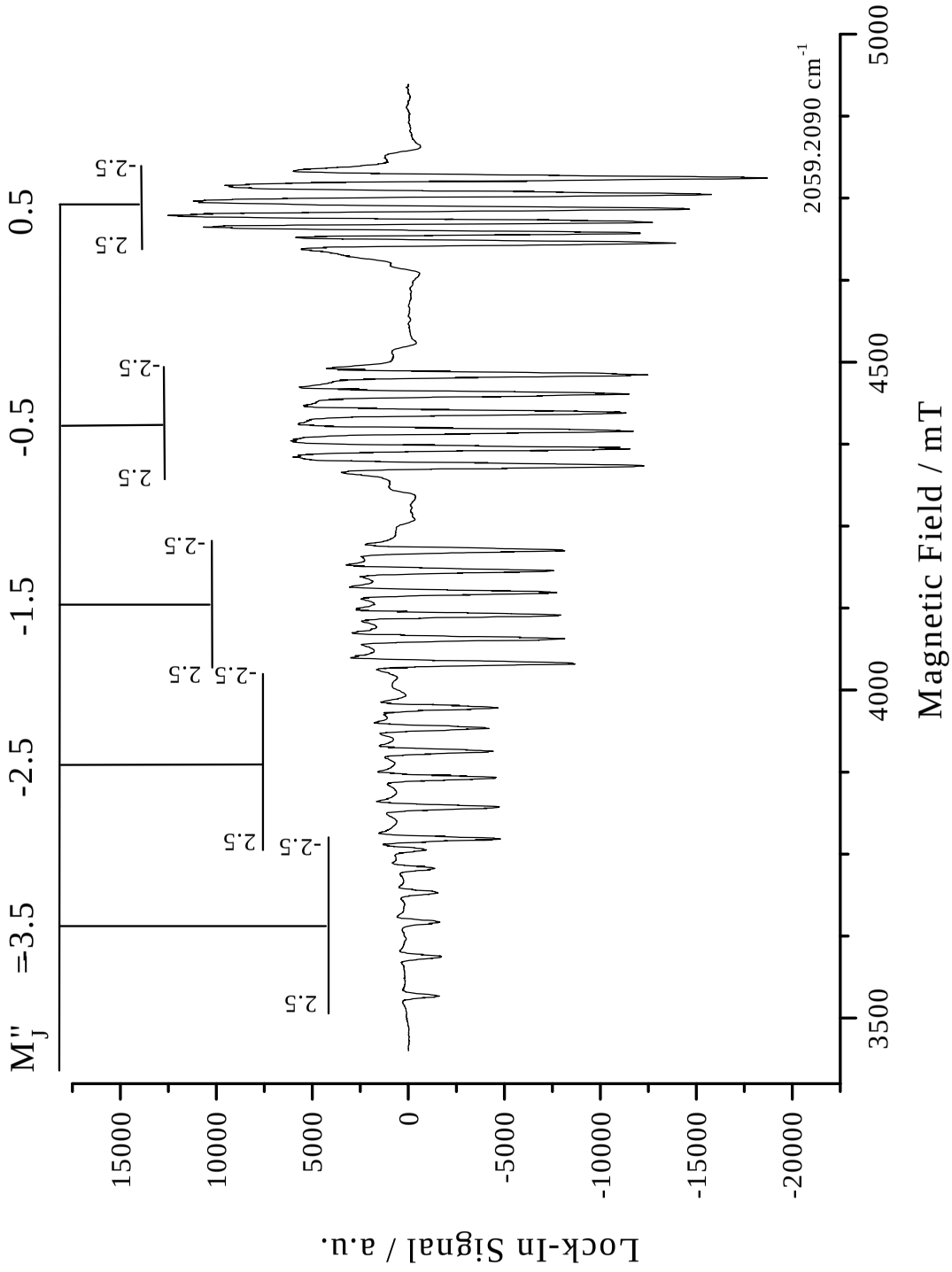

Figure 3.9: Spectrum of I* on the $2P_8$ @ $2059.2090cm^{-1}$ between $3.4T$ and $5.0T$

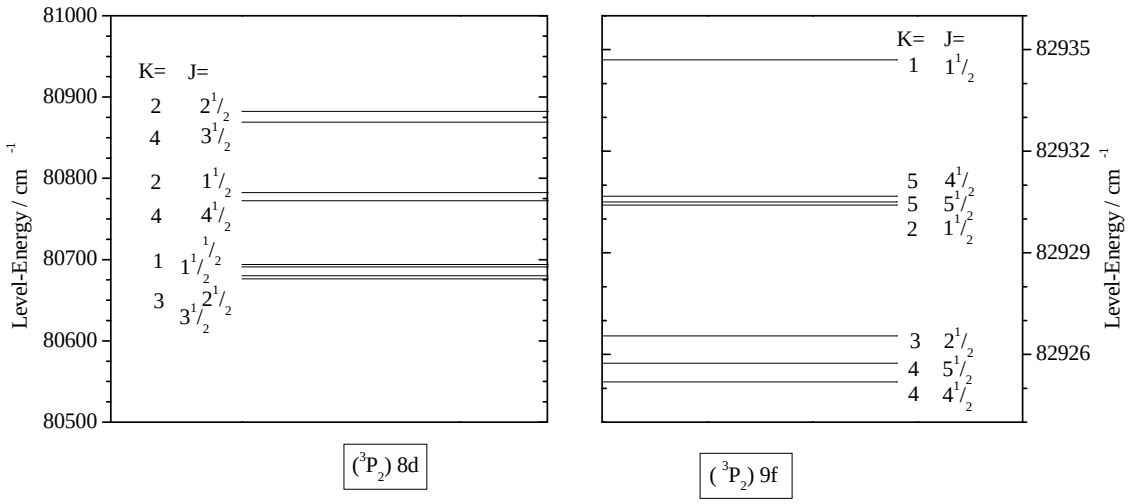

Figure 3.10: Termscheme of $(^3P_2)8d[4]_{3\frac{1}{2}}$ @ $80869.16cm^{-1}$ and $(^3P_2)9f[4]_{4\frac{1}{2}}$ @ $82925.19cm^{-1}$. Note the different energy scales.

pled, s-decoupled basis set, but since the knowledge about the spacing of the different spin-orbit components and the different K levels is not accurate enough, this description is made impossible and a linear fit based on an s-coupled basis set was used instead for the analysis. Although it is not obvious from the Grotrian diagram, the whole configuration $(^3P_2)9f$ behaves according to the theory developed in section 3.3.1. This is different for the levels arising from $(^3P_2)8d$ which are strongly perturbed by other electronic configurations nearby (cf. figure (3.10)) [Min61].

Results of the fitting procedure

From the signals on the $2P_9$ and with the experience gained from the chlorine transition the assignments given in the figures (3.8) and (3.9) have been obtained. Altogether 156 signals have been observed but several of those are blended. These lines have been omitted from the fit so that finally 106 signals were used with equal weight. The resulting parameters are given in table 3.3.

The overall quality of the fit of this transition is satisfying. The standard deviation is of the right order. The residuals of the calculation are illustrated in figures (3.11) and (3.12). Especially on the $2P_8$ a systematic trend in the $M_\mathbf{J}$ structure is observed. An explanation for this can be found in the nonlinear effects caused by the small splitting of the spin-orbit components in the $9f$-level.

Parameter	Value	Std.-Dev.	Unit
$\Delta\tilde{\nu}_0$	2056.42350	$0.24 \cdot 10^{-3}$	cm^{-1}
g_s'	2.00200	$fixed$	
g_s''	2.00200	$fixed$	
g_l'	1.05544	$0.17 \cdot 10^{-3}$	
g_l''	1.27913	$0.16 \cdot 10^{-3}$	
a_l'	0.08779	$0.72 \cdot 10^{-3}$	cm^{-1}
a_l''	0.07028	$0.40 \cdot 10^{-3}$	cm^{-1}
d_l'	-1.84	0.13	cm^{-1}
d_l''	-0.219	0.011	cm^{-1}
Number of observations:			156
Number of fitted observations:			106
Number of fbated parameters :			7
Standard deviation of total fit:			$1.8 \cdot 10^{-3} cm^{-1}$
			$\hat{=}56.9 MHz$

Table 3.3: Parameters for the transition $(^3P_2)9f[4]_{4\frac{1}{2}} \leftarrow (^3P_2)8d[4]_{3\frac{1}{2}}$ determined by a linear least-squares fit.

The accuracy of the different parameters is adequate. The value obtained for the zero field splitting $\Delta\tilde{\nu}_0$ is slightly away from the value predicted by L. Minnhagen. The g-factors are both too large. While the deviation from 1 is rather small for the upper $9f$ state, the value of 1.27913 for g_l'' indicates a mixing of the lower state with some different adjacent electronic configuration. This effect has already been observed by L. Minnhagen [Min61]. He found that the distribution of the $(^3P_2)nd$ levels can not be explained by the model developed in section 3.3.1 due to perturbations arising from other electronic configurations.

The collapse of the hyperfine structure on the $2P_9$ spectrum is modelled quite well although this is masked in the calculation. For the collapsed signals a single field position for all components has been used to calculate the residuals. Therefore the residuals contain in this case not only the statistical error but also the deviation caused by the finite hyperfine splitting.

According to the theoretical model developed above, the magnetic hyperfine constant a should be the same for both states since the core stays the same during the transition. The values obtained from the fit are significantly different which also indicates a disturbance by some other core configuration in the immediate neighborhood.

The eletrostatic hyperfine constant d appears to be even more sensitive to this influence. As a result, both values are not in agreement within their experimental accuracy. Still, the sign of the constant agrees with the observations of previous authors (eg. [LK75]). Since Luc-Koenig *et al.* [LK75] have used an LS coupling scheme for all observed states, a direct comparison between the results is not possible.

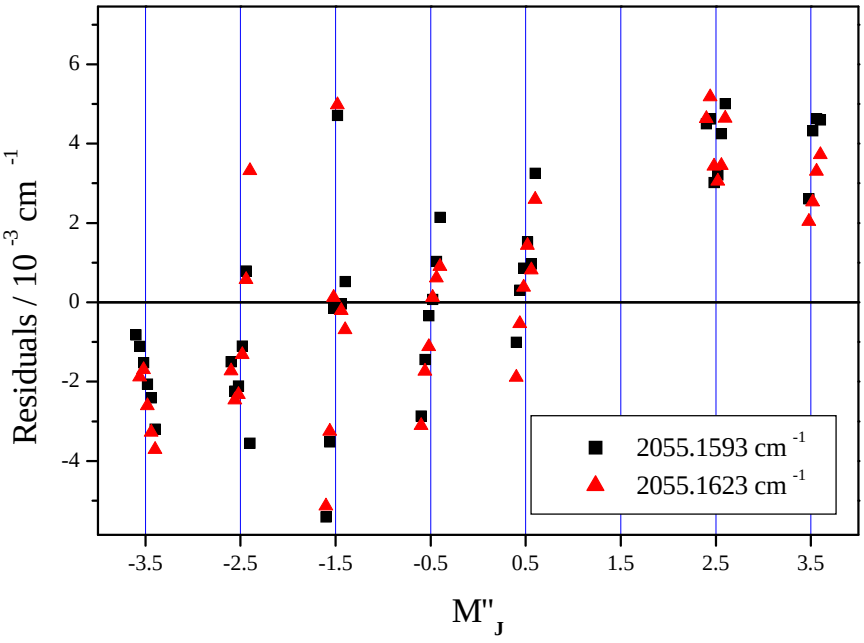

Figure 3.11: Overview of the residuals for the spectrum on the $2P_9$

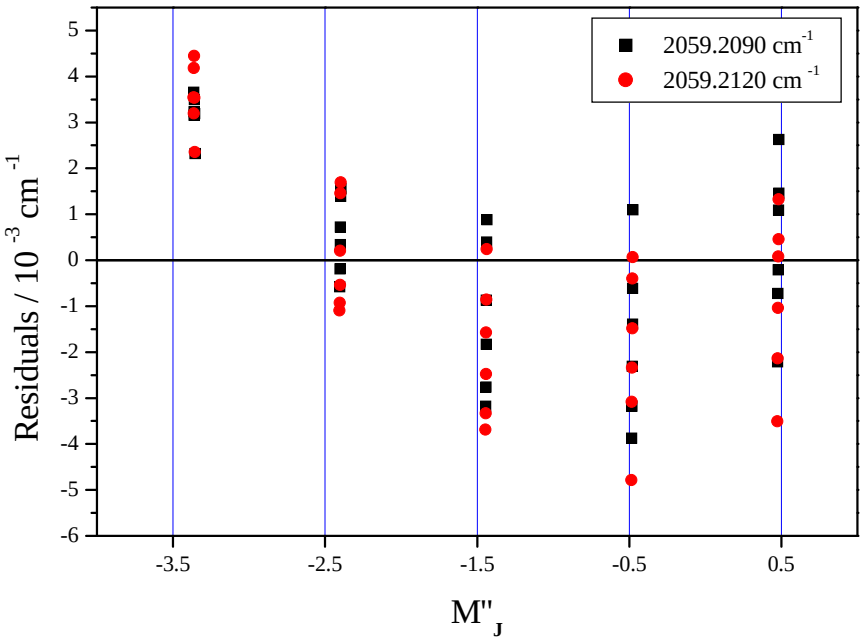

Figure 3.12: Overview of the residuals for the spectrum on the $2P_8$

3.4.4 The transition $(^3P_2)8p[2]_{\frac{3}{2}} \leftarrow (^3P_2)6d[2]_{\frac{3}{2}}$

Observations

The spectrum of this transition as it is observed on the $1P_{12}$ is shown in figure (3.13). The pattern shows three different $M_{\mathbf{J}}$-components. Although the intensity of the first group is somewhat lower than that of the last one, they are both still similar. By contrast, the middle group consists only of blended lines so that the real intensity is hard to guess but is probably somewhat larger than that of the outer ones. Surprisingly, both of the outer groups contain only five instead of six hyperfine components. In general, this can happen when two different signals happen to coincide.

The transition is only observed on this single line so that not a lot of information is made available by the experiment. Only the possibility to record the frequency shifted spectrum using the acousto optic modulator enables one to analyze the transition. This second spectrum is printed in the appendix C, figure (C.3).

Results of the fit

When an s-coupled basis set is assumed, the relative intensities of the different $M_{\mathbf{J}}$ components are proportional to the square of the 3j-symbol

$$\begin{pmatrix} J'' & 1 & J' \\ -M''_{\mathbf{J}} & p & M'_{\mathbf{J}} \end{pmatrix}$$

with $p = \pm 1$ [8]. For $\Delta J = 0$ this becomes [Edm74]:

$$\begin{pmatrix} J & J & 1 \\ M & -M-1 & 1 \end{pmatrix}^2 = \frac{(J-M)(J+M+1)\cdot 2}{(2J+2)(2J+1)(2J)} \tag{3.29}$$

This expression results in an intensity pattern symmetric around $M''_{\mathbf{J}} = \frac{1}{2}$ [9]. In contrast to this, the intensity distribution arising from a transition with $\Delta J = \pm 1$ is proportional to:

$$\begin{pmatrix} J+1 & J & 1 \\ M & -M-1 & 1 \end{pmatrix}^2 = \frac{(J-M)(J-M+1)\cdot 2}{(2J+3)(2J+2)(2J+1)} \tag{3.30}$$

The intensities described by this expression are monotonously rising or falling from one end of the Zeeman pattern to the other one[10] just as it

[8] $p = 0$ is not considered here because of the selection rules arising from the geometry of the experiment (cf. section 2.2 on page 15).

[9] This can be seen when the numerator is rewritten as $(J+\frac{1}{2})^2 - \tilde{M}^2$ where $\tilde{M} = M + \frac{1}{2}$.

[10] Rewriting the numerator using $\tilde{M} = M - J$ yields $\tilde{M}^2 - \tilde{M}$ for the numerator

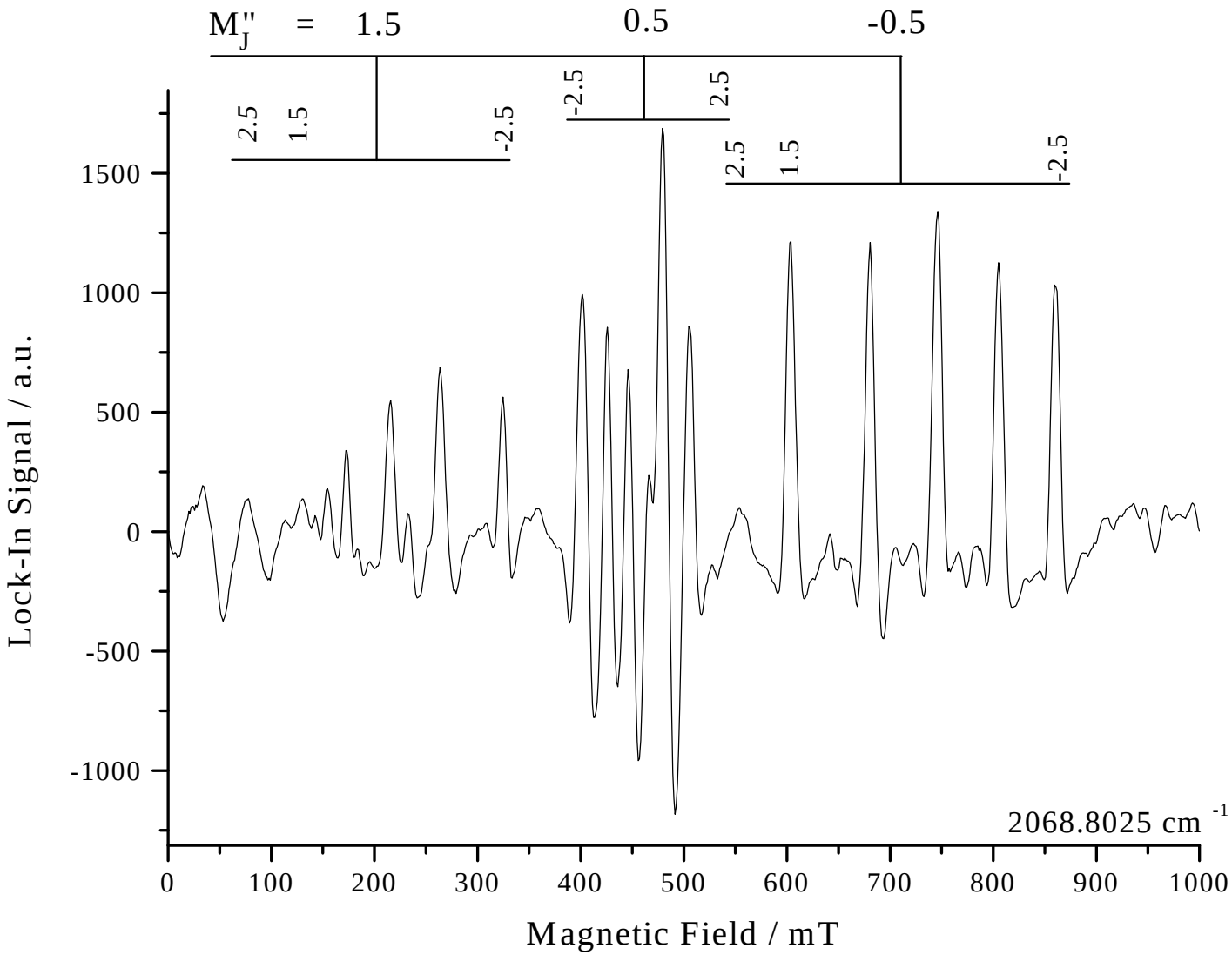

Figure 3.13: Spectrum of I^* on the $1P_{12}$ at low fi eld without AOM.

has been observed for the transition $(^3P_2)8d[4]_{3\frac{1}{2}} \rightarrow (^3P_2)9f[4]_{4\frac{1}{2}}$ in the previous section.

Parameter	Value	Std.-Dev.	Unit
$\Delta\tilde{\nu}_0$	2068.5904	$0.62 \cdot 10^{-3}$	cm^{-1}
g_s'	2.00200	$fixed$	
g_s''	2.00200	$fixed$	
g_l'	1.58	$fixed^a$	
g_l''	0.871	$1.9 \cdot 10^{-3}$	
a_l'	0.07371	$0.7 \cdot 10^{-3}$	cm^{-1}
a_l''	0.07272	$1.2 \cdot 10^{-3}$	cm^{-1}
d_l'	0.0	$fixed^b$	cm^{-1}
d_l''	0.0	$fixed^b$	cm^{-1}
Number of observations:			34
Number of fitted observations:			20
Number of floated parameters :			4
Standard deviation of total fit:			$2.08 \cdot 10^{-3} cm^{-1}$
			$\hat{=} 62.5 MHz$

[a]: Value for g-factor taken from [Moo71].

[b]: Not determinable (see text).

Table 3.4: Parameters for the transition $(^3P_2)8p[2]_{\frac{3}{2}} \leftarrow (^3P_2)6d[2]_{\frac{3}{2}}$ determined by a non-linear least-squares fit.

Hence, the intensity distribution suggests a transition with $\Delta J = 0$ and the middle component of the whole pattern is identified as $M_{\mathbf{J}}'' = \frac{1}{2}$. The three $M_{\mathbf{J}}$ components indicate a total angular momentum of $J = \frac{3}{2}$.

Looking for the right zero field splitting in the lists of known states ([Min61, Moo71]) yields the combination of the two states $(^3P_2)6d[2]_{\frac{3}{2}}$ @ $76746.95 cm^{-1}$ and $(^3P_2)8p[2]_{\frac{3}{2}}$ @ $78815.44 cm^{-1}$. The $g_{\mathbf{J}}$-factor of the upper state has been determined by C. E. Moore [Moo71] to be 1.71 which gives a g_l' factor of 1.58 when equation (3.26) is used.

Since only two different laser frequencies have been used, only two of the parameters $\tilde{\nu}_0$, g_l' and g_l'' are determinable simultaneously. The zero field splitting $\tilde{\nu}_0$ and the g-factor g_l are both known, so one is free to choose one of the two to be fixed. Due to the close correlation between the two g-factors it was decided to fix g_l' at its value of 1.58 and to float $\tilde{\nu}_0$ and g_l'' instead.

Due to the small number of observed hyperfine components the interac-

tion arising from the electric quadrupole moment is not expressed strongly enough to enable a determination of these parameters.

Under these limitations, a non-linear fit of the transition yields the parameters given in table 3.4. For this fit, matrix elements off-diagonal in K have not been taken into account. States arising from a different K-value are away far enough not to disturb the transition significantly. More important are the matrix elements directly off-diagonal in M_{I} since the degeneracy of the hyperfine components at zero field is still not broken fully.

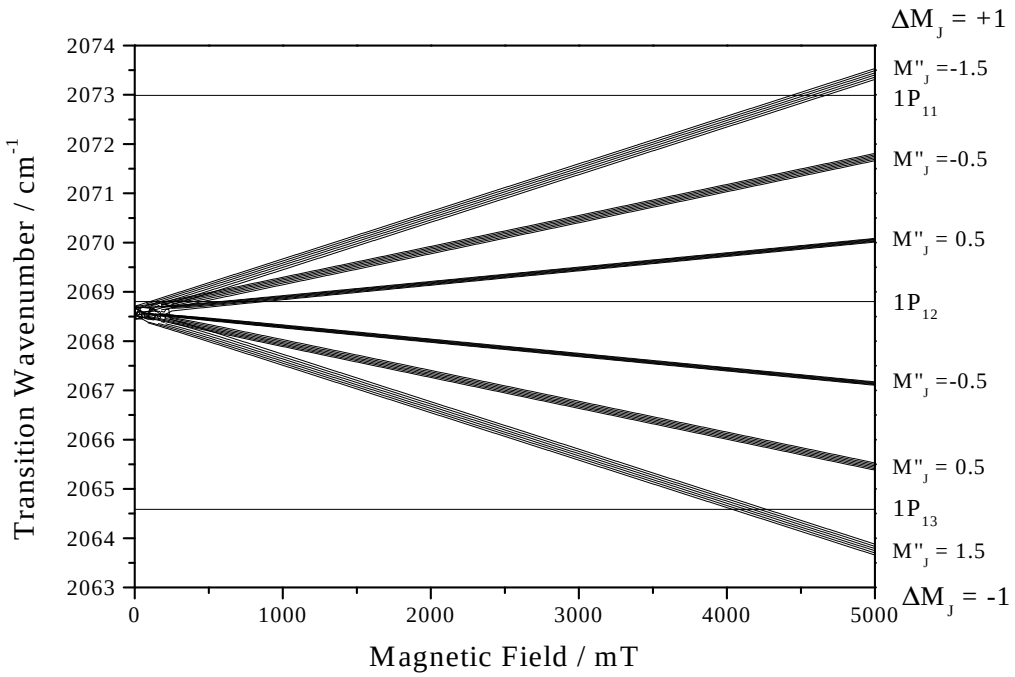

Figure 3.14: Zeeman pattern for the transition $(^3P_2)8p[2]_{\frac{3}{2}} \leftarrow (^3P_2)6d[2]_{\frac{3}{2}}$

A computation of the complete tuning pattern for the σ polarization is shown in figure (3.14). A close-up of the region where the pattern intercepts the $1P_{12}$ is shown in figure (3.15)[11]. For reference, a second trace shows the experimental LMR spectrum. It is obvious that the middle group of the spectrum is not reproduced correctly. This is also to be found in the pattern of the residuals shown in figure (3.16).

The floated parameters are determined quite well. The value of 0.871

[11]The weird looking behavior of the states at very low fields is caused by some numerical error of the computation. The degeneracy of the M_I structure at zero field makes it very difficult for the software to identify the states correctly and thus corrupts the picture at very low fields somewhat. The line of $+$'s still suggests that in the interesting region the identification was correct.

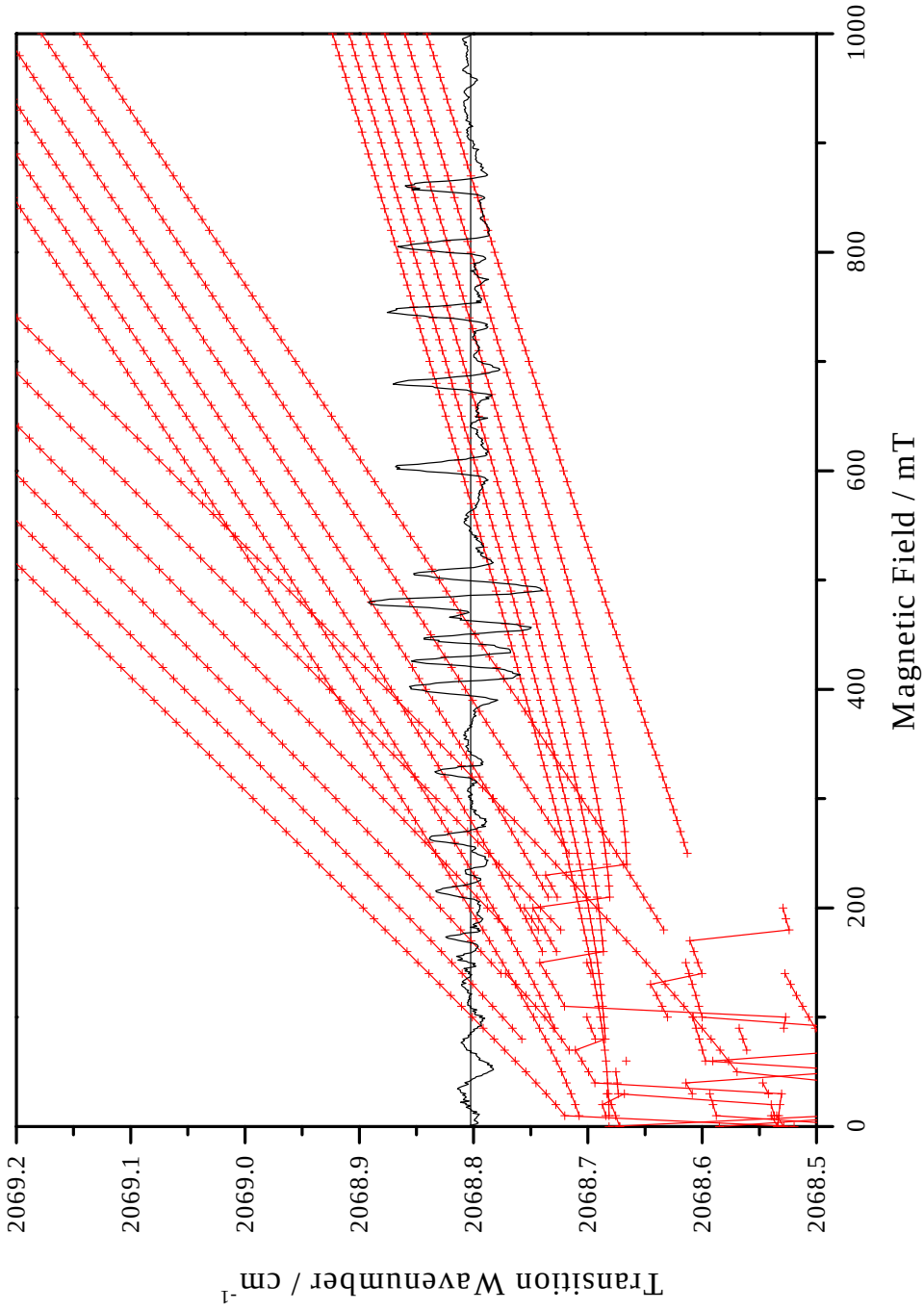

Figure 3.15: Close-up of the intersection of the transition $(^3P_2)8p[2]_{\frac{3}{2}} \leftarrow (^3P_2)6d[2]_{\frac{3}{2}}$ and the $1P_{12}$

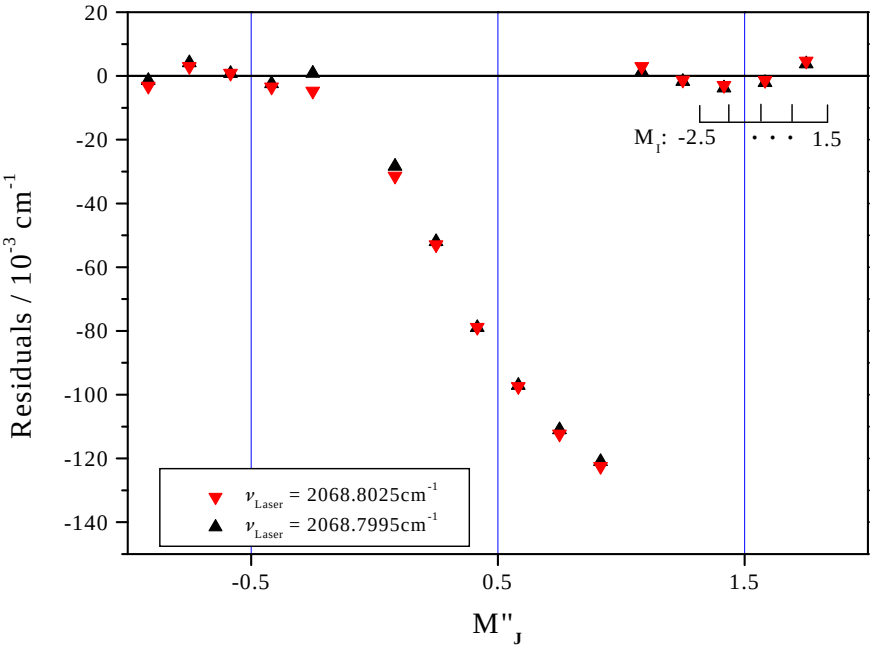

Figure 3.16: Residuals of the transition $(^3P_2)8p[2]_{\frac{3}{2}} \leftarrow (^3P_2)6d[2]_{\frac{3}{2}}$.

for the constant g_l'' is quite reasonable and indicates some disturbance of the wavefunction of the excited electron and the wavefunction of the core electrons. Such a disturbance hinders the excited electron to move freely and thus reduces its orbital g-factor.

As mentioned above, theoretically the magnetostatic hyperfine constants a' and a'' should be identical. The parameters determined for this transition support this expectation quite well for this transition.

The quality of the fit is probably limited by the available experimental data. More than one third of the information had to be rejected since 14 out of 34 lines are blended. This not only reduces the statistically significant observations but also leaves the fit with only two out of three different $M_\mathbf{J}$ components. Another weakness of the available data is the lack of observations on different laser lines. Although only the use of the AOM enables one to analyze this transition, the spectra using the shifted laser frequency are still not as reliable as an additional laser line would be. E. Bachem [Bac88] quotes a relative accuracy of 10% for the measurement of the tuning rate of a transition. This statement seems to be optimistic when comparing the measured tuning rates and the calculated ones given in the tables in appen-

dices B and C.

Furthermore, the transition occurs at very low field strengths. Although C. Pfelzer [Pfe91] tried to avoid using magnetic materials in the immediate surroundings of the solenoid, the field positions have to be considered less accurate at very low fields ($< 100mT$) due to unwanted remanences.

The question concerning the two missing signals remains unanswered. The first one may coincide with the broad, unresolved features at the very beginning of the recording. The signal occurring at higher fields could also coincide with a feature at $\approx 556mT$.

3.4.5 The transition occurring at high field strengths on the $1P_{12}$

Observations

The transition discussed in the previous section is not the only feature observed on the $1P_{12}$. At the high field end of the spectrum, a transition consisting of 3 $M_{\mathbf{J}}$-groups occurs. It is shown in figure (3.17). It is not clear wether the transition possesses further $M_{\mathbf{J}}$ components since the last visible group occurs just at the upper limit of the magnetic field available.

The intensity of the different signals points to a transition with $\Delta J = \pm 1$. Furthermore, the hyperfine structure collapses at the lowest field group. A search in the lists of L. Minnhagen [Min61] and C. E. Moore [Moo71] suggests the transition $(^3P_2)8d[2]_{\frac{5}{2}} \leftarrow (^3P_2)8p[2]_{\frac{3}{2}}$ that should occur at $2066.85cm^{-1}$.

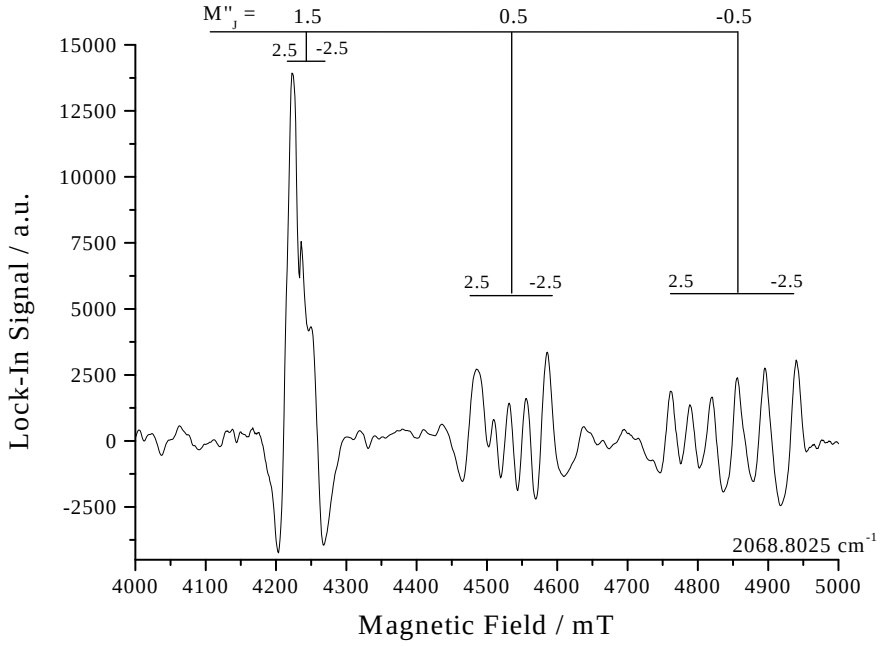

Figure 3.17: Spectrum of I^* on the $1P_{12}$ at high fi eld without AOM.

Analysis

Assuming that the transition has been identified correctly, g_{I}'' is known from Moore's table [Moo71] to be 1.58. Together with the zero field splitting of $2066.85cm^{-1}$ it is possible to fit the transition with very poor results only. Floating the zero field energy difference leads to an unreasonable value for

$\tilde{\nu}_0$ (see table 3.5) although the total standard deviation is adequate.

Parameter	Value	Std.-Dev.	Unit
$\Delta\tilde{\nu}_0$	2064.9810	$0.85 \cdot 10^{-3}$	cm^{-1}
g_s'	2.00200	$fixed$	
g_s''	2.00200	$fixed$	
g_l'	1.470	$1.1 \cdot 10^{-3}$	
g_l''	1.58	$fixed$	
a_l'	0.0625	$1.8 \cdot 10^{-3}$	cm^{-1}
a_l''	0.1257	$2.7 \cdot 10^{-3}$	cm^{-1}
Number of observations:			36
Number of fitted observations:			20
Number of fbated parameters :			4
Standard deviation of total fit:			$3.0 \cdot 10^{-3} cm^{-1}$
			$\hat{=} 90 MHz$

Table 3.5: Parameters obtained for a fit of the transition at high field on the $1P_2$ assuming the assignment $(^3P_2)8d[2]_{\frac{5}{2}} \leftarrow (^3P_2)8p[2]_{\frac{3}{2}}$

In the next attempt to analyze this transition, the g_l factors were fixed at their theoretical value of 1. Although there is no justification for it, the angular momenta were assumed to be correct[12]. Surprisingly, this simple approach leads to fit with a standard deviation of only $90MHz$ (cf. table 3.6).

Encouraged by this result, the configuration of the core was varied. Since the hyperfine structure is observed, only $^3P_1$, $^3P_2$ and $^1D_2$ have to be considered. In addition to this, the upper g_l parameter was varied as well. The different parameters obtained by these fits are given in table 3.7.

The interpretation of these parameters is difficult. The g-factors for the $^3P_2$ core are very close to the theoretical value of 1 and thus indicate a rather unperturbed state. This is contradicted by the hyperfine constant a which is quite different for both states. Basically, the same applies to the $^3P_1$ core. For the $^1D_2$ core the values for a also differ by 50% while the determined g-factor is very small.

In addition to the standard deviation, the scattering of the residuals can be taken as a measure of the quality of the fit. The diagram (3.18) shows

[12] i.e. the error in the total assignment is assumed to be only in the principal quantum number of the two states.

Parameter	Value	Std.-Dev.	Unit
$\Delta\tilde{\nu}_0$	2065.7469	$0.74 \cdot 10^{-3}$	cm^{-1}
g_s'	2.00200	$fixed$	
g_s''	2.00200	$fixed$	
g_l'	1.0	$fixed$	
g_l''	1.0	$fixed$	
a_l'	0.1057	$2.3 \cdot 10^{-3}$	cm^{-1}
a_l''	0.0478	$1.7 \cdot 10^{-3}$	cm^{-1}

Number of observations:	36
Number of fitted observations:	20
Number of fbated parameters :	3
Standard deviation of total fit:	$3.0 \cdot 10^{-3} cm^{-1}$
	$\hat{=} 90 MHz$

Table 3.6: Parameters obtained for a linear fit of the transition at high field on the $1P_{12}$ assuming $g_l = 1.0$

this distribution for the different cores. For the shifted laser frequency the picture is quite similar. Obviously, the core $^1D_2$ returns the best results here.

Now the tuning pattern has been calculated assuming a $^3P_2$ core. The complete pattern is shown in figure (3.19) while a close-up of the region where the pattern intersects the laser line $1P_{12}$ is shown in figure (3.20).

Since the origin of the transition of $2065.7522(12) cm^{-1}$ lies almost in the middle between the $1P_{12}$ $(2068.8025 cm^{-1})$ and $1P_{13}$ $(2064.5839 cm^{-1})$, one expects to find some signals on the second line as well. This situation is shown in figure (3.21) where the LMR spectrum observed on the $1P_{13}$ is also printed.

Here a group of signals occurs between $\approx 2100 mT$ and $\approx 3200 mT$ while the spectrum is predicted to occur between $\approx 1550 mT$ and $\approx 2100 mT$. Considering the amount of information known for this transition, the discrepancy between experimental and calculated spectrum is not too large.

Theoretically, the intensity ratio should be $10 : 6 : 3 : 1$ for the four groups. It is rather difficult to extract the intensity information from the spectrum since the blended lines mask the real intensity strongly. Therefore it is hardly possible to use this indicator for further inquiries into the nature of the observed states.

Param.	Value	Std.-Dev.	Value	Std.-Dev.	Unit
	$^3P_2$		$^3P_1$		
$\Delta\tilde{\nu}_0$	2065.7522	$1.2 \cdot 10^{-3}$	2066.2220	$0.98 \cdot 10^{-3}$	cm^{-1}
g_s'	2.0020	$fixed$	2.0020	$fixed$	
g_s''	2.0020	$fixed$	2.0020	$fixed$	
g_l'	0.9948	$1.0 \cdot 10^{-3}$	0.8842	$0.70 \cdot 10^{-3}$	
g_l''	1.0	$fixed$	1.0	$fixed$	
a_l'	0.1003	$2.1 \cdot 10^{-3}$	0.2545	$5.1 \cdot 10^{-3}$	cm^{-1}
a_l''	0.0499	$1.4 \cdot 10^{-3}$	0.0703	$1.9 \cdot 10^{-3}$	cm^{-1}
Std.-Dev.	$2.3 \cdot 10^{-3} cm^{-1}$ $\hat{=} 68.8 MHz$		$1.9 \cdot 10^{-3} cm^{-1}$ $\hat{=} 56.4 MHz$		

Param.	Value	Std.-Dev.	Unit
	$^1D_2$		
$\Delta\tilde{\nu}_0$	2066.9266	$0.68 \cdot 10^{-3}$	cm^{-1}
g_s'	2.0020	$fixed$	
g_s''	2.0020	$fixed$	
g_l'	0.5736	$0.45 \cdot 10^{-3}$	
g_l''	1.0	$fixed$	
a_l'	0.0308	$0.59 \cdot 10^{-3}$	cm^{-1}
a_l''	0.0153	$0.39 \cdot 10^{-3}$	cm^{-1}
Std.-Dev.	$1.3 \cdot 10^{-3} cm^{-1}$ $\hat{=} 39.3 MHz$		

Table 3.7: Comparison of linear fits of the transition at high field on the $1P_2$ using different cores. Only 20 of a total of 36 observations have been used.

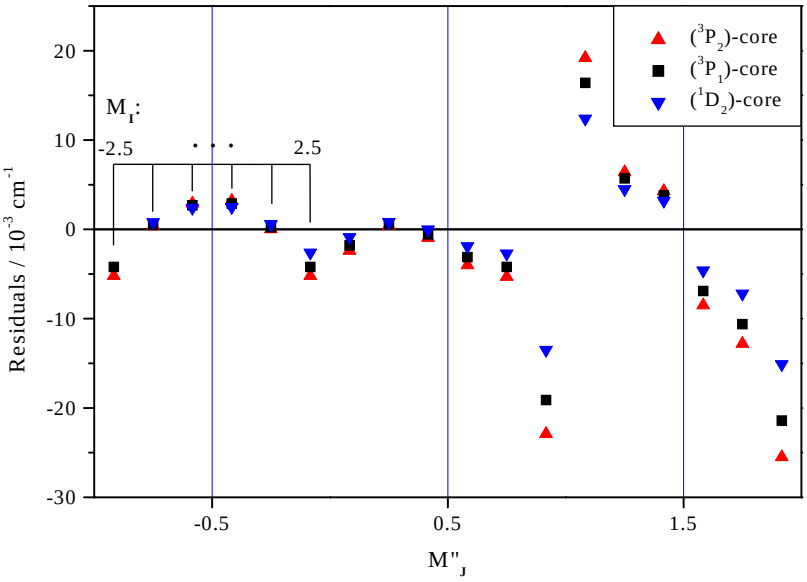

Figure 3.18: Comparison of the residuals obtained for the high fi eld feature at the $1P_{12}$ with different cores

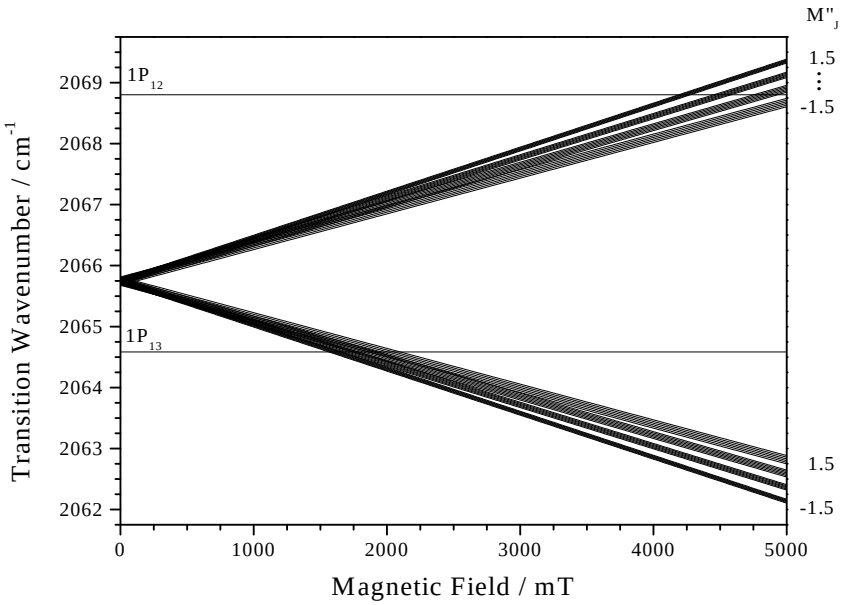

Figure 3.19: Tuning pattern of the unknown transition observed on the $1P_{12}$

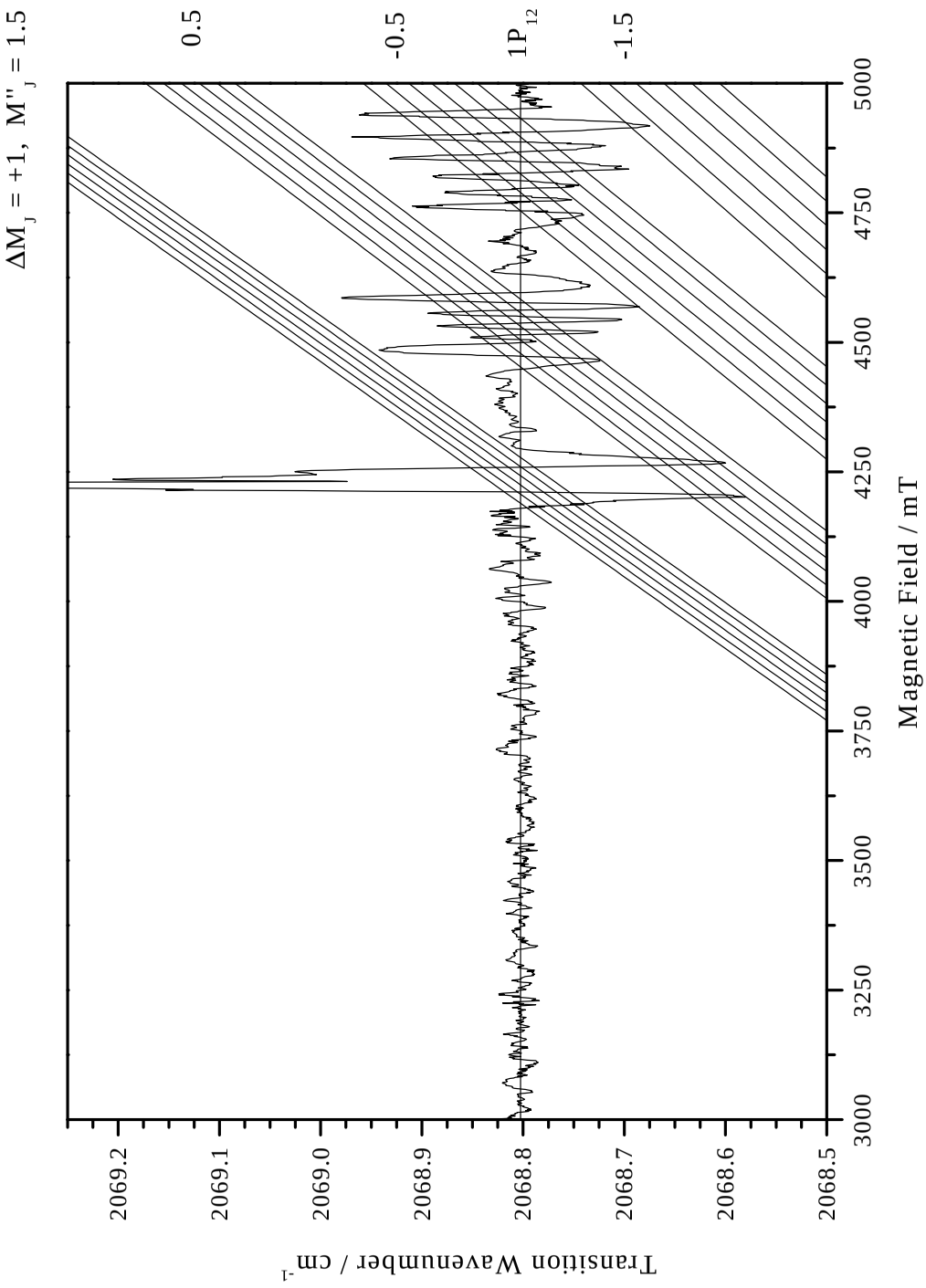

Figure 3.20: Close up of the $\Delta M_{\mathbf{J}} = +1$ tuning pattern of the unknown transition observed on the $1P_{12}$

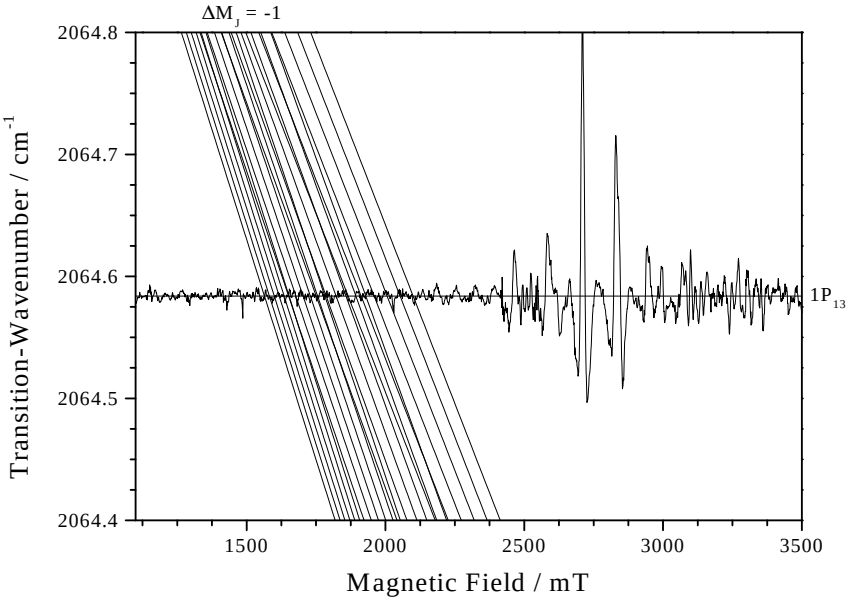

Figure 3.21: Close up of the $\Delta M_{\mathbf{J}} = -1$ tuning pattern of the unknown transition observed on the $1P_{12}$

3.4.6 Interpretation of further observations

Quite a number of further signals have been observed that have to be ascribed to atomic iodine. It turned out to be impossible to analyze these transitions mostly because of the lack of available information. In all cases no suitable states have been found in the lists of Minnhagen [Min61] and Moore [Moo71]. Also, the spectra observed on the $0P_{11}$ and $0P_{10}$ have been observed only once so that without any additional information an analysis is impossible. For future use, the next few paragraphs discuss the information on these transitions as it is available from the LMR experiments.

Further transitions of excited iodine appearing in the LMR spectrum of the $2P_9$

In section 3.4.3 a weak feature appearing on the $2P_9$ was mentioned. This group of signals is shown in figure (3.22). Their intensity is much weaker than those observed at higher fields. The lock-in sensitivity had to be decreased by a factor of 100 to see this transition. The intensity pattern looks rather symmetric thus suggesting a $\Delta J = 0$ transition. Due to the neighborhood of the transition $(^3P_2)9f[4]_{4\frac{1}{2}} \leftarrow (^3P_2)8d[4]_{3\frac{1}{2}}$ it seems reasonable to identify the transition as arising from the $3\frac{1}{2}$-spin-orbit component of the state $(^3P_2)9f[4]$. According to Minnhagen [Min61], the two components are split by $0.55cm^{-1}$ so that the transition $(^3P_2)9f[4]_{3\frac{1}{2}} \leftarrow (^3P_2)8d[4]_{3\frac{1}{2}}$ should occur at $2056.58cm^{-1}$. Using the results from section 3.4.3, the transition will be shifted to $2056.97cm^{-1}$. Both transition energies lie above the laser line $2P_9$ $(2055.1593cm^{-1})$. Therefore moving the laser frequency by $+90MHz$ using the AOM should shift the LMR spectrum to lower field strength. Instead figure (3.23) shows that the zero field transition occurs at a lower frequency. Hence, the transition can not be identified as suggested above. Since the group is strongly blended, it is not possible to characterize the transition further.

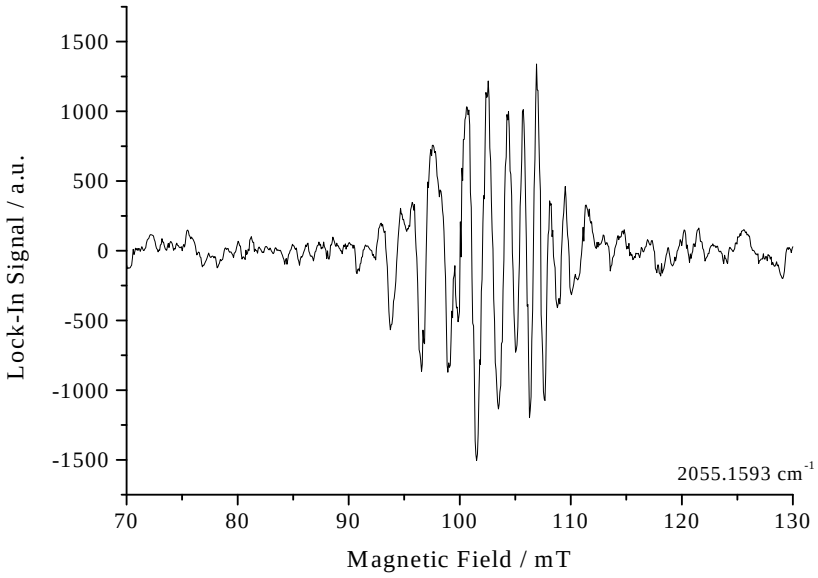

Figure 3.22: Transition at intermediate field strength on the $2P_9$

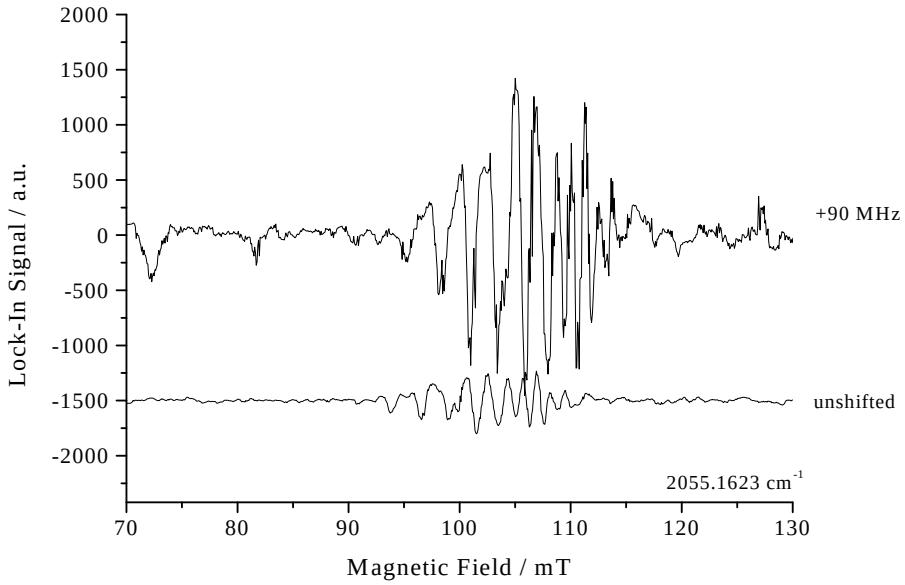

Figure 3.23: Tuning behavior of the group of signals at intermediate field strength on the $2P_9$

Further transitions of excited iodine appearing in the LMR spectrum of the $1P_{12}$

One feature showing in the spectrum of the $1P_{12}$ has not yet been discussed. At an intermediate field strength a group of strong signals appears. It is shown in figure (3.24).

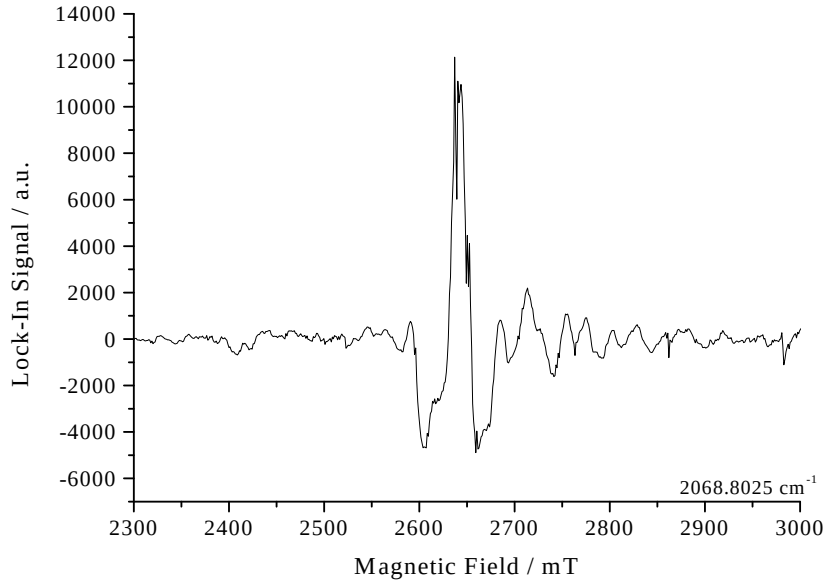

Figure 3.24: Feature at intermediate fi eld strength on the $1P12$

The signals are blended and no additional information is available for them from the lists of Moore [Moo71] and Minnhagen [Min61]. Therefore a detailed analysis is not possible. The only accessible information can be derived from the tuning behavior. When the frequency is shifted by $-90MHz$, the signals move to lower field strengths, thus indicating a zero field frequency $< 2068.8025cm^{-1}$.

Transitions of excited iodine appearing in the LMR spectrum of the $1P_{13}$

The spectrum recorded on the $1P_{13}$ is shown in figure (3.25). Two groups of signals are to be seen on this laser line. The first one occurs between 2400 and $3500mT$ while the second one is found above $3500mT$. A number of signals below $2400mT$ are not considered to belong to the first group of signals since their spacing and their intensity does not seem to fit to the remaining ones.

For both groups of signals the intensity distribution suggests a transition with $\Delta J = 0$. Interestingly, the hyperfine structure is not expressed for the first group of signals. This leads to the conclusion that the signals are either not caused by iodine but by helium or oxygen or they arise from states with a core of $^3P_0$ or $^1S_0$. Since on one hand this transition has not been found in a list of known states for helium and oxygen, while on the other hand for iodine almost nothing is known about the system of states arising from these cores, it can not be decided what species is causing these signals.

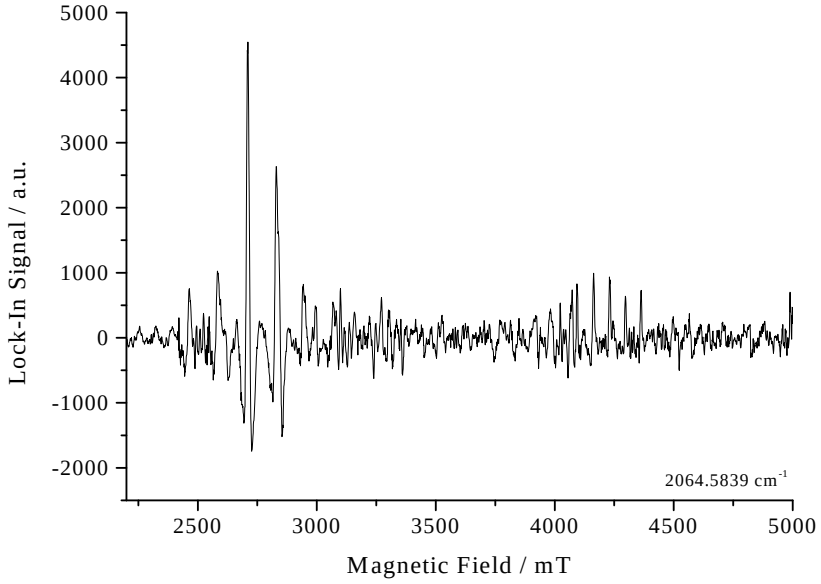

Figure 3.25: Iodine signals observed on the $1P_{13}$

Transitions of excited iodine appearing in the LMR spectrum of the $0P_{11}$

The spectrum in figure (3.26) shows a number of strong signals. Their origin is not clear since they have been observed in a discharge through helium, iodine and oxygen during the investigation of iodine monoxide as described in the next chapter. It is not easily possible to sort the signals into $M_{\mathbf{J}}$ components in a unique way. The lack of hyperfine structure again gives no hint on the origin of these signals.

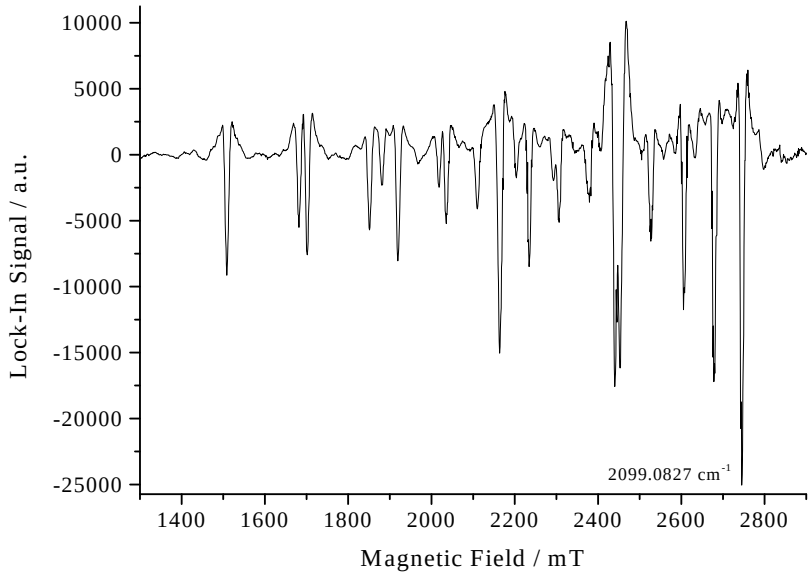

Figure 3.26: Spectrum of atomic species recorded on the $0P_{11}$

Transitions of excited iodine appearing in the LMR spectrum of the $0P_{10}$

On the $0P_{10}$ again two different groups of signals have been recorded. In the region between 3000 and $4150mT$ five groups of signals show the classical hyperfine structure for iodine atoms. The intensity distribution points to a transition with $\Delta J = \pm 1$. Since for such a transition $(2J+1)$ $M_{\mathbf{J}}$-components are expected, there must be an additional group of signals at lower field strengths. Probably, this group is masked by noise and the adjacent IO signals. Furthermore, from the number of $M_{\mathbf{J}}$-components one finds that the smaller value for J has to be $\frac{5}{2}$.

The remaining five signals belong to a transition without hyperfine structure so that again the origin of the signals is not clear.

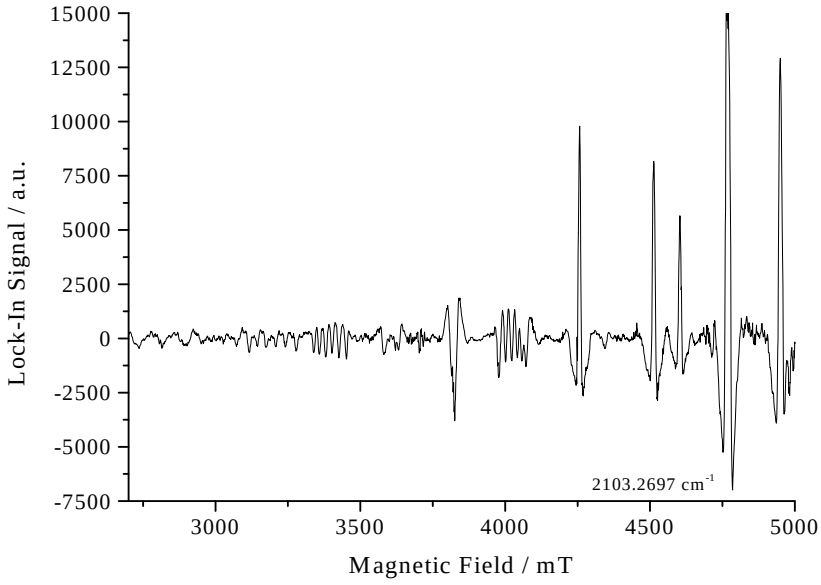

Figure 3.27: Spectrum of the $0P_{10}$

3.5 Summary of the results

In this part of the thesis, an investigation of the LMR spectrum of iodine atoms has been described. On the experimental side, the major problem consisted in injecting iodine molecules in a controlled manner into the gas discharge. Once this was achieved, the gas discharge provided a stable source of single atoms in several excited states.

For the theoretical description of the spectra, it was found necessary to refine the model used by E. R. Comben [Com86]. Besides the spin-orbit interaction, the hamiltonian derived for this purpose also included the magnetic hyperfine interaction, the electric quadrupolar hyperfine interaction, the Zeeman interaction and the interactions arising from the electronic configuration of the atomic state in the central field approximation as introduced by Condon and Shortley [Con35]. Afterwards the hamiltonian was expressed in a matrix representation using an LS, a $J_cK, s-coupled$ and a $J_cK, s-decoupled$ basis set. A software was developed that is capable of fitting the atomic parameters included in this model. In particular, the program is able to fit transitions arising from states that are best described in two different vector coupling schemes. The software was tested using data generated synthetically as well as using data from a previous investigation ([Com86]). In the later, an error in the assignment was found and corrected for.

The theory developed in this way was applied to the observed spectra. For three transitions a complete analysis was performed. While for the first of these transitions the analysis is quite satisfactory, the nature of the other two transitions is a bit dubious. For the second one a nominally good fit was obtained although some of the observed features are only poorly reproduced from theory so that the assignment of the quantum numbers is still questionable. In the third case, no information on the states involved is available. A reasonable fit was still obtained by guessing the quantum numbers of the states.

In several other cases it was not possible to analyze the LMR spectra. Some of these transitions reveal a hyperfine structure that identifies their origin to be atomic iodine. Since the grid of laser lines is to coarse in this frequency region it is not possible to gather a sufficient number of observations to enable a successful analysis of the transitions. For these transitions only qualitative results have been obtained.

Chapter 4

The fi ne structure Transition in Iodine Monoxide

In this chapter, the investigation of the Laser Magnetic Resonance spectrum of iodine monoxide in the region around $2100cm^{-1}$ is described. The first section provides an overview of the present knowledge about the vibronic ground state of iodine monoxide. In the second section of this chapter, the experimental procedure and the observed spectra are shown. There follows a brief discussion of the theoretical background necessary to understand how these spectra arise. This discussion will be much shorter than the corresponding section in chapter 3 because no contribution to this has been made by the author himself. After this, the attempt made to analyze the spectrum are described. In the final section the chapter is summarized briefly.

4.1 Previous investigations of iodine monoxide

Iodine monoxide has a long tradition in the research of small radicals. A huge number of investigations of theoretical as well as experimental nature have been performed in the past to characterize this molecule.

On the experimental side, the rotational structure of IO in its electronic ground state $X^2\Pi_{\frac{3}{2}}$ has been investigated thoroughly by EPR [Car70, Bro72] and microwave spectroscopy [Sai73]. Several investigations have been carried out on the transition $A^2\Pi_{\frac{3}{2}} \leftarrow X^2\Pi_{\frac{3}{2}}$. Especially an experiment performed by J.P. Bekooy, W. Leo Meerts and A. Dymanus [Bek83] has provided valuable information on the ro-vibrational structure of both states.

The information available on the ground state has been refined in recent times by an investigation by F. Tamassia, S. M. Kermode and J. M. Brown

where the vibrational overtone band $v = 2 \leftarrow 0$ has been observed by Laser Magnetic Resonance [Tam01].

However, all these investigations were just concerned with the $\Omega = \frac{3}{2}$-spin component of the ground state. This is caused by the huge spin-orbit splitting present in this molecule. In 1972, it was estimated by J. M. Brown *et al.*to about $-2300cm^{-1}$ [Bro72]. Due to this large splitting, it becomes difficult to populate the rovibrational levels in the $\Omega = \frac{1}{2}$ component, and thus it was impossible to record rotational data of these levels. This problem was overcome by C. E. Miller and E. A. Cohen [Mil01] by producing and exciting the molecule in a gas discharge. For the first time, their experiment provided rotational data of both spin components under high resolution.

With all these earlier studies, a fairly complete picture of the molecular ground state has been obtained. Only the magnitude of the spin-orbit splitting itself remained unknown until 1992 when M. K. Gilles *et al.* were able to determine the splitting experimentally by photoelectron spectroscopy [Gil92] to $-2091(40)cm^{-1}$. To the best knowledge of the author, a direct measurement of transitions between both spin components under high resolution has not been performed to date.

4.2 Experimental Details

4.2.1 Production of IO

For the production of iodine monoxide a similar setup of the absorption cell as for the experiment on iodine atoms has been used. It is shown in figure (4.1). The only difference is the additional inlet for oxygen close to the cathode. As before, the iodine partial pressure is not determinable here either. While this was not of much importance for the iodine atoms, here it causes a major concern. In order to establish an optimum production of IO, the iodine concentration has to be controlled very well. Several chemical reactions can occur that prevent the build up of a decent concentration of IO:

$$\begin{aligned} IO + O &\rightarrow IO_2 \\ IO + O &\rightarrow I + O_2 \\ 2IO + O &\rightarrow I_2O_5 \\ I + O_2 &\rightarrow OIO \end{aligned} \tag{4.1}$$

However, in former investigations the same problem has occurred as

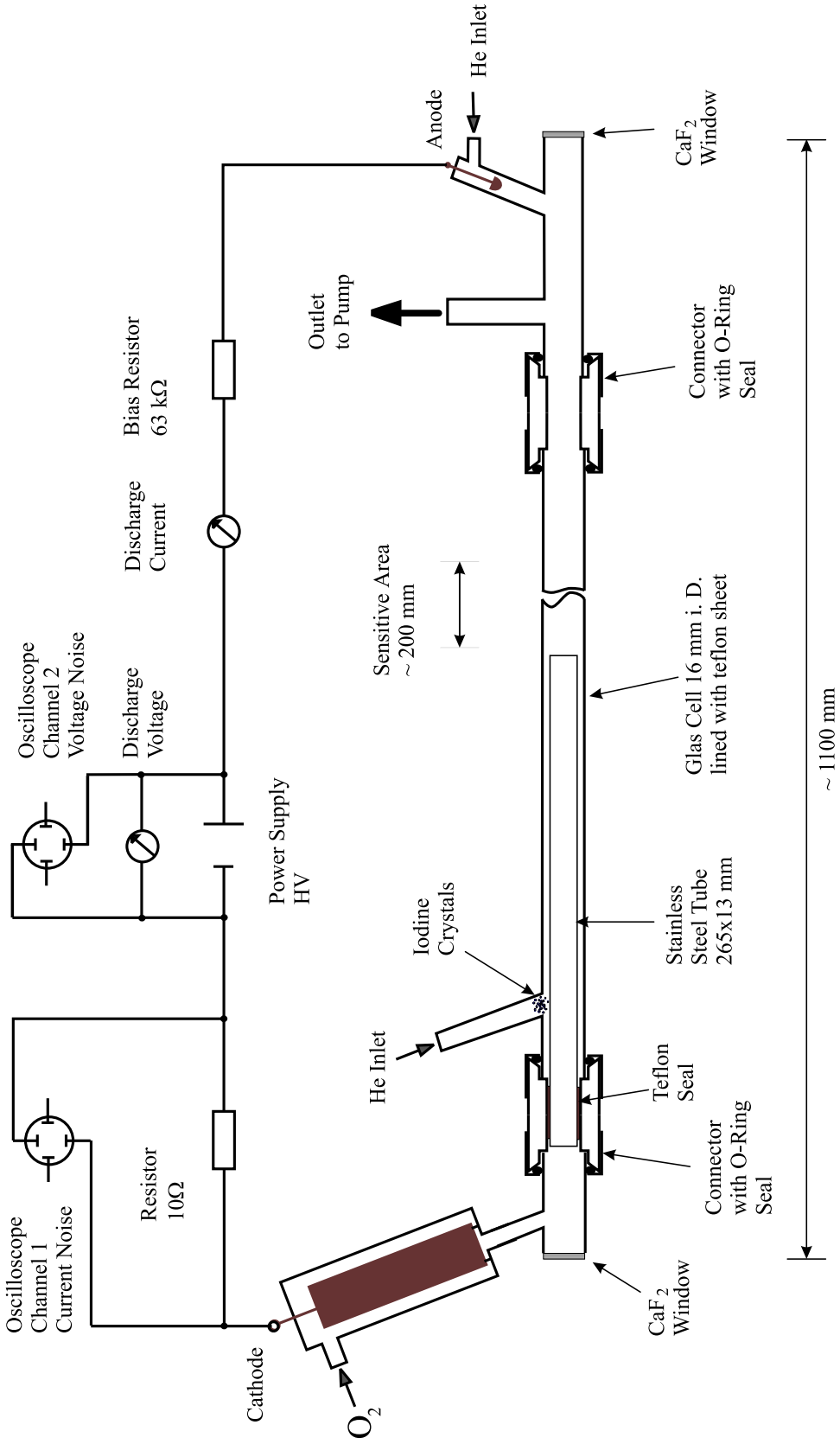

Figure 4.1: Confi guration of the absorption cell used for the detection of iodine monoxide

well. For example, C. E. Miller and E. A. Cohen [Mil01] have used a very similar way to inject the iodine into the discharge. They decided to use the bright yellow chemiluminescence as an indicator for the production of IO. As has been seen in chapter 3 this chemiluminescence is not due to iodine monoxide but due to excited iodine atoms[1]. Still, this indicator is not completely wrong. In agreement with the expectations arising from the chemical reactions (4.1) it was observed that the spectrum ascribed to IO vanishes when a certain concentration of oxygen is exceeded. This phenomenon is accompanied by a sharp change in the color of the discharge. The bright yellow glow is replaced by a dark red one of unknown origin.

This characteristic behavior has been used to establish a reproducible production of iodine monoxide. Analogous to the method described in [Mil01], the discharge was started with helium and iodine only. Then oxygen was added successively until the red glow was just about to appear. Finally, the oxygen pressure was slightly reduced to establish a constant production of IO.

In this way, spectra were recorded on the laser lines $1P_{13}$ to $1P_8$ and $0P_{13}$ to $0P_{10}$ ($2064cm^{-1}$ to $2103cm^{-1}$). An overview of them is given in figure (4.2) while the single spectra are collected in appendix D. Frequency-shifted spectra were recorded for the $1P_{10}$, $1P_{11}$ and $1P_{12}$. No attempt was made to record spectra using the AOM on the remaining laser lines since the AOM removes about 20% of the input intensity. Since the intensity especially of the laserlines at higher wavenumbers is already at the lower limit for scanning this seemed not reasonable to do.

4.3 Theoretical description of a diatomic radical

4.3.1 Effective Hamiltonian of a diatomic molecule

For modelling the energy levels of a diatomic molecule the method of an effective hamiltonian is used. It has been derived by Brown *et al.* [Bro79a, Bro79b]. The description given in this section is also guided by the previous investigation by Tamassia et al. [Tam01].

The energy of the ground state of a diatomic molecule consists of several contributions:

- Vibrational energy $\mathcal{G}$

[1] Indeed, the production of IO is accompanied by a pale green cheminoluminescence [Ker98].

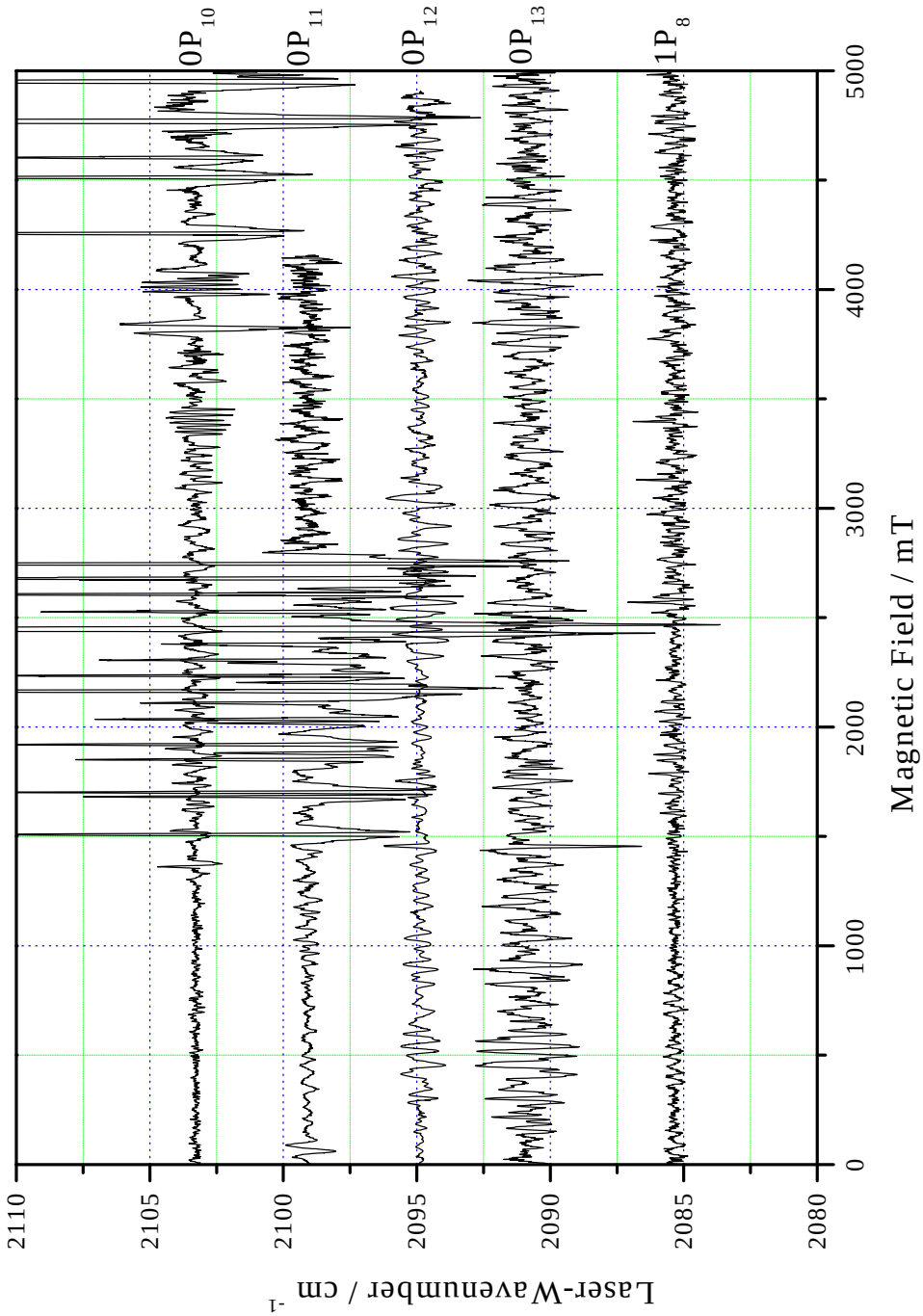

Figure 4.2 (a): Overview of the LMR spectrum of IO in the region above $2060cm^{-1}$. The baseline of the individual spectrum is placed at the observed laser wavenumber while the lock-in signal (in arbitrary units) is just added to this baseline.

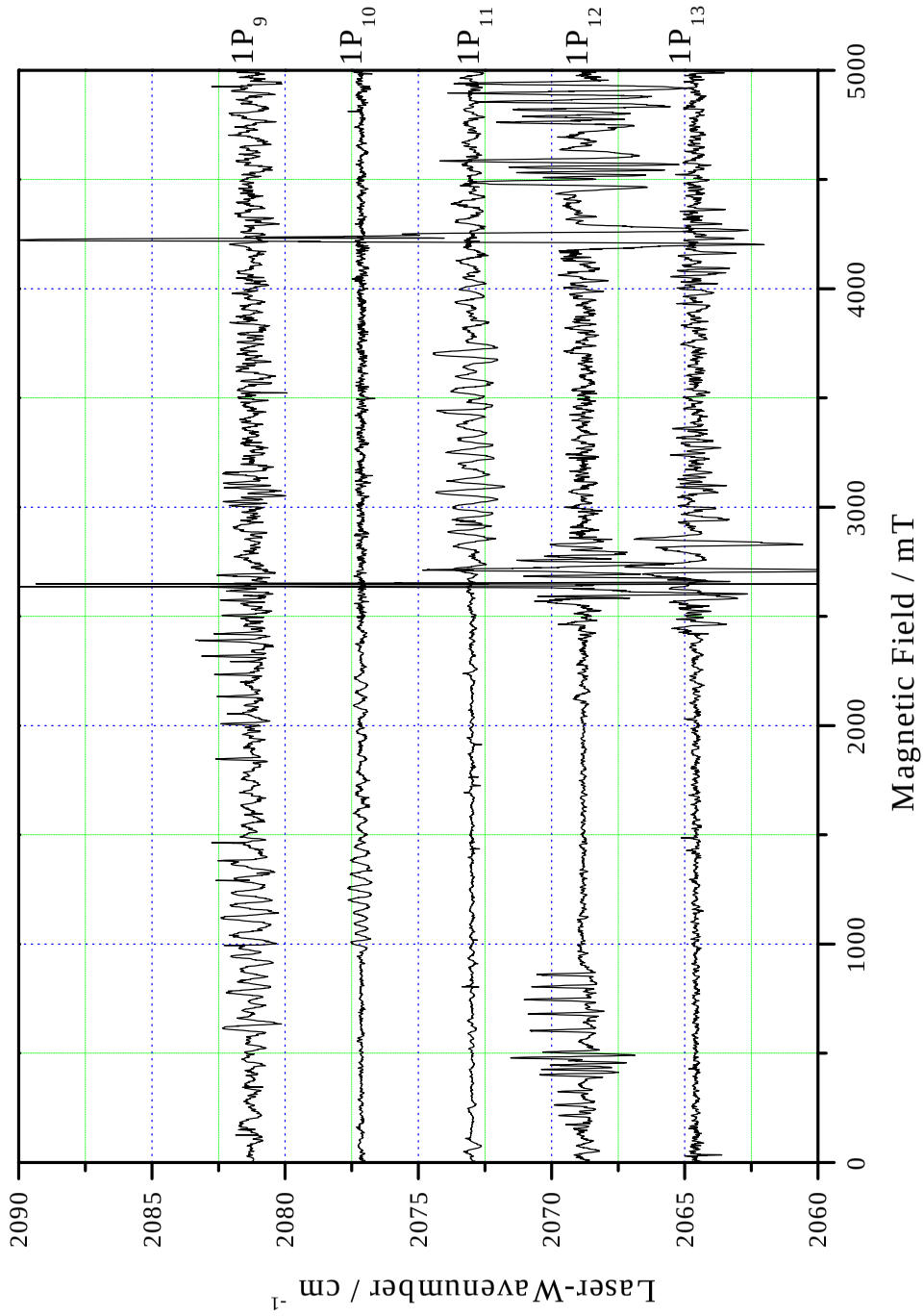

Figure 4.2 (b): Overview of the LMR spectrum of IO in the region above $2060 cm^{-1}$. (cont.)

In zero order approximation, the potential energy curve for an attractive energy level in a diatomic is $\propto r^2$ where r is the internuclear distance. Hence, the vibrational energy is treated as that of a harmonic oscillator. Deviations from this behaviour are taken into account by perturbation theory. Therefore, the vibrational energy is developed into a series and has the eigenvalues:

$$\begin{aligned}\mathcal{G}(v) &= (v+\frac{1}{2})\omega_e - (v+\frac{1}{2})^2\omega_e x_e \\ &\quad + (v+\frac{1}{2})^3\omega_e y_e + (v+\frac{1}{2})^4\omega_e z_e + \ldots \end{aligned} \quad (4.2)$$

Here v is the vibrational quantum number taking values $0, 1, 2, 3 \ldots$, ω_e the vibrational frequency and $\omega_e x_e, \ldots$ are the anharmonic correction constants to the potential energy function of first and higher orders.

- Spin-Orbit interaction $\mathcal{H}_{SO}$

  Due to the loss of spherical symmetry, the spin-orbit interaction takes a more complicated form than in the atoms (cf. 3.3.2). In a Hund's case (a) basis set[2], it can be described by:

$$\mathcal{H}_{SO} = A_0 L_z S_z + \frac{1}{2} A_D \cdot [\mathbf{N}^2, L_z S_z]_+ + \frac{1}{2} A_H \cdot [\mathbf{N}^4, L_z S_z]_+ \quad (4.3)$$

  where $\mathbf{N}$ is $\mathbf{J} - \mathbf{S}$. The little z indicates the components of $\mathbf{L}$ and $\mathbf{S}$ in the molecular fixed frame of reference and the $[.,.]_+$ are anticommutators. In a pure case (a) basis set, the expression $L_z S_z$ is diagonal in Ω so that the spin-orbit coupling constant A_0 will be equivalent to the energy difference between the $\Omega = \frac{1}{2}$- and $\Omega = \frac{3}{2}$-spin-components. A_D and A_H are the quartic and sextic centrifugal distortion terms, respectively.

- Rotational energy $\mathcal{H}_{rot}$

  The rotational energy is given by the hamiltonian:

$$\mathcal{H}_{rot} = B_0 \mathbf{N}^2 \quad (4.4)$$

  B_0 is called the rotational constant of the molecule. This constant is inversely proportional to the moment of inertia. Therefore this constant depends strongly on the expectation value of the internuclear distance and changes in the latter arising for different vibrational wave-

[2] See also section 4.3.2

functions have to be taken into account. As for several other parameters sensitive to the internucler distance, this is done by using perturbation theory to develop the parameter into a series:

$$P_v = P_e + \alpha_P(v + \frac{1}{2}) + \beta_P(v + \frac{1}{2})^2 + \dots$$

where P_e is the value of the parameter P at the equilibrium distance and $\alpha_P, \beta_P, \dots$ are the corrections in higher orders.

- Centrifugal distortion correction of the rotational energy $\mathcal{H}_{cd}$

  The centrifugal distortion term describes the deviation of the molecular behavior from that of a rigid rotor. The rotation of the molecule leads to a small stretching of the internuclear distance which effectively reduces the rotational constant. The effect is taken into account by perturbation theory and yields a contribution to the hamiltonian given by:

$$\mathcal{H}_{cd} = -D_0 \cdot \mathbf{N}^4 + H_0 \cdot \mathbf{N}^6 \tag{4.5}$$

  D_0 is the constant giving the first order correction to the rotational energy while the second order correction is given by H_0.

- Λ-doubling $\mathcal{H}_{LD}$

  In the expression for the spin-orbit coupling, $A_0 L_z S_z$ the additional term $(L_+ S_- + L_- S_+)$ was neglected since it connects different electronic states. In Hund's case (a), it is assumed that these states are far enough apart not to influence each other. However, especially in the case of a molecule in an electronic Π state this effect can become significant since it leads to a decoupling of the orbital angular momentum from the molecular axis. In the theory this is described as a perturbation by an adjacent Σ state. The corresponding expressions have been derived by J. M. Brown and A. J. Merer [Bro79b]:

$$\mathcal{H}_{LD} = \frac{1}{2}(p+2q)\left(e^{2i\Phi} S_- J_- + e^{-2i\Phi} S_+ J_+\right) - \frac{1}{2} q \left(e^{2i\Phi} J_-^2 + e^{-2i\Phi} J_+^2\right) \tag{4.6}$$

  The coordinate Φ is the electron azimuthal angle introduced by Brown *et al.* [Bro78].

- Centrifugal distortion of Λ-doubling $\mathcal{H}_{cdLD}$

Analogous as for the case of the rotational energy, the Λ doubling is subject to centrifugal distortion. This contribution is given by:

$$\mathcal{H}_{cdLD} = \frac{1}{4}(p_D + 2q_D) \cdot \left[\mathbf{N}^2, \left(e^{2i\Phi} S_- J_- + e^{-2i\Phi} S_+ J_+\right)\right]_+ \quad (4.7)$$

- Hyperfine interaction $\mathcal{H}_{hfs}$

  As for the spin-orbit coupling, the lack of spherical symmetry complicates matters for the hyperfine interaction as well. The full hamiltonian dealing with this is [Tam01]:

$$\begin{aligned}
\mathcal{H}_{hfs} &= aI_zL_z + b(I_xS_x + I_yS_y) + (b+c)I_zS_z \\
&+\frac{1}{2}d\left(e^{-2i\Phi} I_+S_+ + e^{2i\Phi} I_-S_-\right) \\
&+\frac{1}{4}d_D\left[\mathbf{N}^2, e^{-2i\Phi} I_+S_+ + e^{2i\Phi} I_-S_-\right]_+ \\
&+C_I\mathbf{I}.\mathbf{N} + \frac{1}{2}C_I'\left(e^{-2i\Phi} I_+N_+ + e^{2i\Phi} I_-N_-\right) \\
&+\frac{eQq_0}{4I(2I-1)}\left(3I_z^2 - \mathbf{I}^2\right) + \frac{eQq_2}{8I(2I-1)}\left(I_+^2 + I_-^2\right) \\
&+\frac{eQq_{0D}}{4I(2I-1)}\mathbf{N}^2\left(3I_z^2 - \mathbf{I}^2\right) \\
&+\frac{eQq_\Omega}{4I(2I-1)}\left(3I_z^2 - \mathbf{I}^2\right)S_z \qquad (4.8)
\end{aligned}$$

  Here the parameters a,b,c and d represent the magnetic interactions of the nuclear spin $\mathbf{I}$ with $\mathbf{L}$ or $\mathbf{S}$ and are defined in [Fro52]. d_D is the centrifugal distortion correction to d. $C_\mathbf{I}$ and $C_\mathbf{I}'$ are the nuclear spin-rotation coupling parameters describing the magnetic interaction between the nuclear spin and the rotating electric dipole moment of the whole molecule. Similar to the parameter d, $C_\mathbf{I}'$ describes the second order contribution connecting states of different parity.

  The parameters $eQq_{...}$ describe interactions arising from the nuclear quadrupole moment. Due to the reduced symmetry, instead of the single constant d or $b_\mathbf{J}$ two different coupling constants, eQq_0 and eQq_2 give the axial and the off-axial component of the electric quadrupolar interaction respectively. The rotation of the molecule just affects the axial component leading to the centrifugal correction constant $eQq_{0\,D}$. Since the internuclear distance is quite different for both spin

components of the ground state[3], the axial coupling constant eQq_0 changes significantly in both spin-components of the ground state and it becomes necessary to introduce the parameter $eQq_\Omega = eQq_0(\Omega = \frac{3}{2}) - eQq_0(\Omega = \frac{1}{2})$ ([Tam01, Mil01]).

- Zeeman Effect $\mathcal{H}_Z$

  In addition to the above contributions, in the presence of an outer magnetic field the Zeeman effect has to be added as well. It is described by the hamiltonian:

$$\begin{aligned}\mathcal{H}_Z &= g_L\mu_{Bohr}B_0L_Z + g_S\mu_{Bohr}B_0S_Z - g_r\mu_{Bohr}B_0N_Z \\ &+ g_l\mu_{Bohr}\left(S_xB_x + S_yB_y\right) - g_N\mu_{nuc}B_0I_Z \\ &+ g_r^{'}\mu_{Bohr}\left(e^{-2i\Phi}N_+B_+ + e^{2i\Phi}N_-B_-\right) \\ &+ g_l^{'}\mu_{Bohr}\left(e^{-2i\Phi}S_+B_+ + e^{2i\Phi}S_-B_-\right) \qquad (4.9)\end{aligned}$$

  As before, the first two terms describe the contribution arising from the interaction of the magnetic field with the orbital and the spin angular momentum of the electrons, respectively. The corresponding interaction with the rotation of the molecular framework is contributing the third term while the fifth arises from the nuclear spin. The remaining terms represent second order effects which appear because of the mixing with different electronic states (e.g. Λ doubling).

4.3.2 Hund's case (a) basis set for diatomic molecules

As mentioned previously it is necessary to express the hamilton operator of the molecular system in some basis set in order to calculate its energy levels. F. Hund has systematically investigated such basis sets [Hun26]. Iodine monoxide is usually described in Hund's basis set (a) shown in figure (4.3). In this coupling scheme it is assumed that the electronic orbital angular momentum $\mathbf{L}$ and the electronic spin angular momentum $\mathbf{S}$ are strongly coupled to the molecular axis by the electric field of the nuclei. Independently of each other both angular momenta precess about the internuclear axis. Correspondingly, their z-components[4], called Λ and Σ respectively, are well defined quantum numbers.

[3] $r_e^{expt}(^2\Pi_{\frac{3}{2}}) = 186.76188(2)pm$ and $r_e^{expt}(^2\Pi_{\frac{1}{2}}) = 188.46802(6)pm$ [Mil01]

[4] Capital letters are used for coordinates referring to the laboratory fi xed frame of reference, while small letters are referring to the molecular fi xed frame of reference.

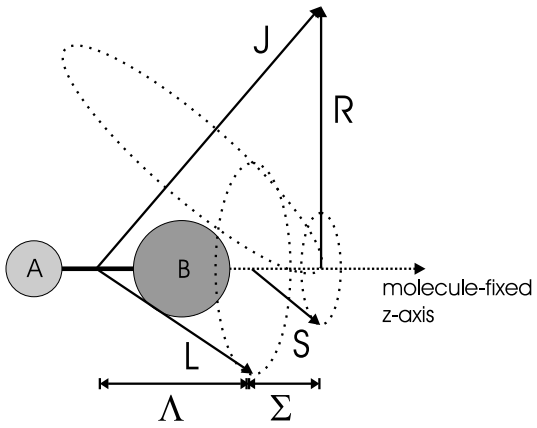

Figure 4.3: Vector model for Hund's case (a)

The spin-orbit coupling is the next strongest interaction. This causes the sum of Λ and Σ, designated Ω, to be a good quantum number as well. Together with the angular momentum $\mathbf{R}$ arising from the rotation of the nuclei about each other, the total angular momentum $\mathbf{J}$ is built. Since $\mathbf{R}$ is always perpendicular to the internuclear axis, this angular momentum has no z-component. Finally, if a nuclear spin is present this couples to the total angular momentum $\mathbf{J}$. Similar to the hyperfine interaction in atoms, this coupling is easily broken when an outer magnetic field is present. Since the magnetic field also defines a frame of reference fixed in the laboratory, the Z-components $M_{\mathbf{J}}$ and $M_{\mathbf{I}}$ become good quantum numbers as well.

Therefore the hamilton operator can be represented in the basis set:

$$|\Lambda\Sigma, J\Omega M_{\mathbf{J}} > \otimes |I, M_{\mathbf{I}} >$$

If Λ doubling is present, the quantum number Λ is only approximately a good quantum number due to the mixing with the Σ state. Instead of this, the degeneracy of the two possible parities of a state is lifted. Therefore the parity becomes an additional property characterizing a state which is then described by:

$$|\Lambda\Sigma, J\Omega M_{\mathbf{J}} > \otimes |I, M_{\mathbf{I}} > \otimes |P >$$

where P takes either the value $+1$ or -1.[5] As before, the selection rules for the transitions are closely related to the basis set. In contrast to the previous chapter, the transition $X^2\Pi_{\frac{1}{2}} \leftarrow X^2\Pi_{\frac{3}{2}}$ is not electric dipole allowed since the selection rule $\Delta\Omega = 0$, valid for this kind of transitions, is violated.

[5] Although Λ ceases to be a good quantum number, the mixing with the Σ state due to the Λ doubling is considered to be small so that the state mainly keeps its previous character and Λ can still be used as an additional attribute of the state.

Instead the weaker magnetic dipole transitions are allowed. For these the selection rules are:

$$\begin{aligned}
\Delta\Lambda &= 0 \\
\Delta\Sigma &= 0, \pm 1 \\
\Delta\Omega &= \pm 1 \\
\Delta J &= 0, \pm 1 \\
\Delta M_J &= 0, \pm 1 \\
\Delta I &= 0 \\
\Delta M_I &= 0 \\
\Delta P &= 0
\end{aligned}$$

4.4 Interpretation and qualitative analysis

4.4.1 Observations

Although the spectra are quite noisy due to the low laser intensity available, on all lines reproducible features are observed. These features are rather weak as expected for magnetic dipole transitions. Furthermore all signals are blended by adjacent features. Thus a rich hyperfine structure is indicated as expected for an iodine containing species.

Another reason to ascribe the observed spectrum to iodine monoxide is found in the dependency on special chemical conditions. The signals become weaker when the present concentration of oxygen is reduced. When the iodine partial pressure is reduced[6] the spectrum is not observed as well. Hence, the observed species contains oxygen as well as iodine. Now the fact described above that an excess of oxygen reduces the signal strength suggests that only a single oxygen atom is present since an increase of the oxygen concentration will favor the production of higher iodine oxides, $I_x O_y$, with $y \geq 1$. Furthermore, a literature search shows that these higher oxides do not possess the right vibrational energies for a spectrum to occur in this frequency region. Hence, the spectrum has to be ascribed to iodine monoxide.

A closer look at the different recordings (fig. (4.2)) reveals a gap on the $1P_{10}$ and the $1P_{11}$, as shown in fig. (4.4) and (4.5)[7]. While on the $1P_{10}$ the region below $1.0T$ is free of any strong signals, the first strong signal on

[6] e.g. when the iodine supplies are spent

[7] cf. also appendix D, pages 130 / 131

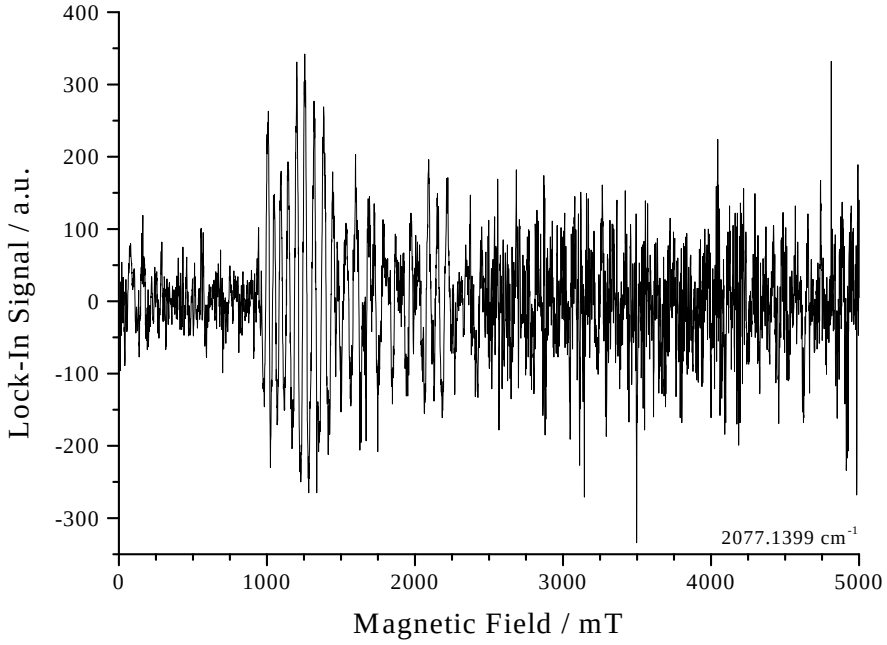

Figure 4.4: Spectrum of IO on the $1P_{10}$ @ $2077.1399cm^{-1}$

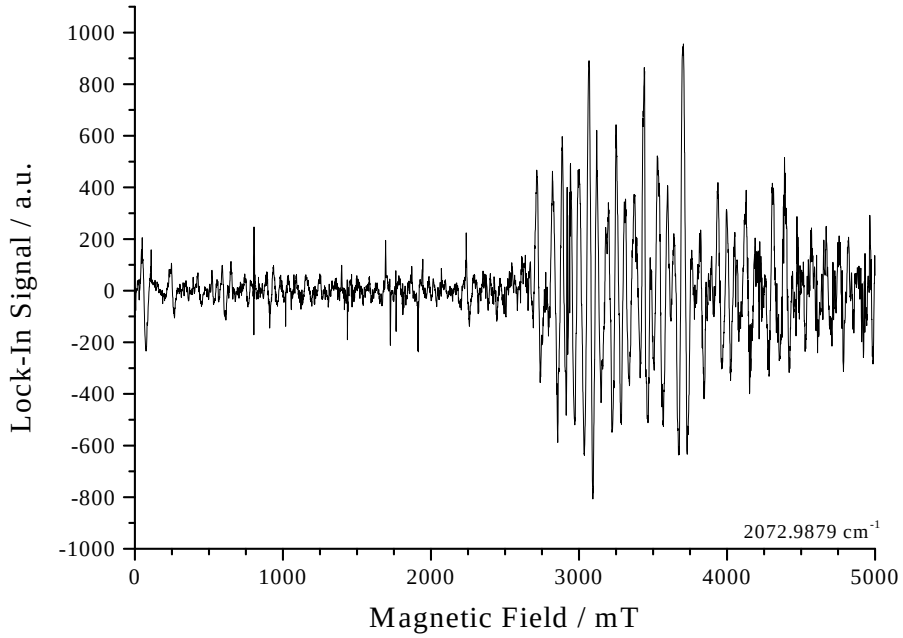

Figure 4.5: Spectrum of IO on the $1P_{11}$ @ $2072.9879cm^{-1}$

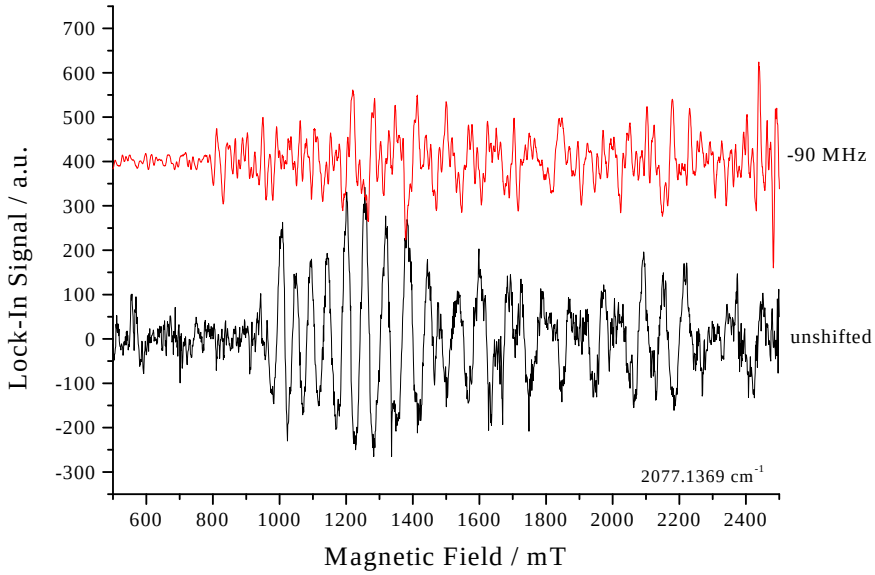

Figure 4.6: Spectrum of IO on the $1P_{10}$ shifted by $-90MHz$ to $2077.1369cm^{-1}$ between $0.5T$ and $2.5T$

the $1P_{11}$ occurs above $2.5T$. Intuitively, this can be interpreted as the band origin.

The AOM-spectra shown in figures (4.6) and (4.7) are not as easy to interpret as in the case of the iodine transitions. Instead, some of the lines appear to be shifted to higher fields while some seem to be shifted to lower ones. This indicates that several different transitions occur in the same region.

4.4.2 Evaluation of previous investigations and simulation of the LMR spectrum

Due to the unresolved hyperfine structure a quantitative analysis of the recorded data is made very difficult. Since no signal positions are available, a different approach from before is necessary. On the other hand, the major effect of the fine structure splitting will be a shift of the total spectrum. Therefore it is a possible approach to simulate the observed spectrum using the parameters obtained from previous investigations and to shift this simulation until it coincides with the observed spectrum.

In order to do this, the rotational data from [Mil01] were used. Since a wide variety of slightly different hamilton operators is in use throughout the

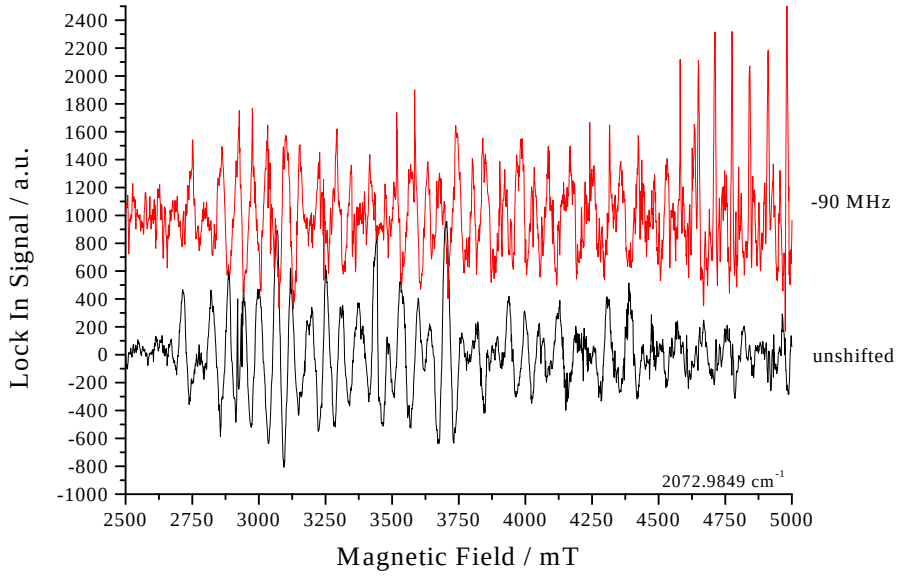

Figure 4.7: Spectrum of IO on the $1P_{11}$ shifted by $-90MHz$ to $2072.9849cm^{-1}$ between $2.5T$ and $5.0T$

spectroscopic community, the first step consisted in repeating the fit from Miller and Cohen in order to obtain the best set of parameters available for the present purpose.

This fit was performed using the software ”Hunda” and yielded the parameter set given in table 4.1. The spin-orbit splitting was kept fixed at a value of $-2075cm^{-1}$ [8] that was estimated from the overview of the spectra as suggested above. Several parameters have not been determined since their standard deviation was larger than their actual value obtained by the fit.

The fit finishes with a standard deviation of less than $\approx 0.5MHz$ which is far below experimental resolution for the LMR experiment. Therefore this inaccuracy is not expected to affect the quality of the simulation too much.

The parameters obtained in this way were fed back into ”Hunda” in order to calculate the Zeeman pattern of the first few transitions of P-, Q- and R-branch. For $A_0 = -2073.5cm^{-1}$ the result of a calculation excluding

[8] The fit of the pure rotational data is rather insensitive to the spin-orbit splitting so that the precise value is of no real concern at this stage of the analysis.

Parameter	Fitted Value	Standard Deviation	Unit
A_0	-2075.0	*estimated*	cm^{-1}
ω_e	672.86038	$0.42 \cdot 10^{-3}$ [a]	cm^{-1}
$\omega_e x_e$	4.32508	$0.40 \cdot 10^{-3}$ [a]	cm^{-1}
$\omega_e y_e$	-0.01	[a]	cm^{-1}
B_0	0.3357728	$0.65 \cdot 10^{-6}$	cm^{-1}
α_B	$-2.7074 \cdot 10^{-3}$	$2.5 \cdot 10^{-6}$ [a]	cm^{-1}
D_0	$0.347 \cdot 10^{-6}$	$1.3 \cdot 10^{-9}$	cm^{-1}
α_D	$0.013 \cdot 10^{-6}$	[a]	cm^{-1}
H_0	$-1.09 \cdot 10^{-12}$	$0.68 \cdot 10^{-12}$	cm^{-1}
A_D	$6.178 \cdot 10^{-3}$	$0.9 \cdot 10^{-6}$	cm^{-1}
A_H	$-18.06 \cdot 10^{-9}$	$0.96 \cdot 10^{-9}$	cm^{-1}
q	0.0	$fixed$[c]	cm^{-1}
$(p+2q)$	0.108846	$23 \cdot 10^{-6}$	cm^{-1}
$(p+2q)_D$	$0.039 \cdot 10^{-6}$	$0.037 \cdot 10^{-6}$	cm^{-1}
a	0.0254	$0.12 \cdot 10^{-3}$	cm^{-1}
α_a	$-0.212 \cdot 10^{-3}$	[a]	cm^{-1}
b	0.0	$fixed$[c]	cm^{-1}
$(b+c)$	-0.01189	$0.24 \cdot 10^{-3}$	cm^{-1}
d	0.03687	$0.066 \cdot 10^{-3}$	cm^{-1}
$C_{\mathbf{I}}$	$9.02 \cdot 10^{-6}$	$0.74 \cdot 10^{-6}$	cm^{-1}
eQq_0	-0.0632	$0.15 \cdot 10^{-3}$	cm^{-1}
α_{eQq_0}	$-2.8519 \cdot 10^{-3}$	[a]	cm^{-1}
eQq_2	0.097	0.044	cm^{-1}
eQq_Ω	$-8.04 \cdot 10^{-3}$	$0.75 \cdot 10^{-3}$	cm^{-1}
g_S	2.002	[a]	
g_L	1.002515	$71 \cdot 10^{-6}$ [a]	
g_N	1.12531	[a]	
Std.-Dev.			69
Std.-Dev. of typ. Observ.			$0.016 cm^{-1}$ $\hat{=} 0.48 MHz$

[a]: Value taken from reference [Tam01].

[c]: Value for parameter less than its uncertainty.

Table 4.1: Molecular parameters of the ground state $X^2\Pi_i$ of iodine monoxide determined from the microwave data of [Mil01]

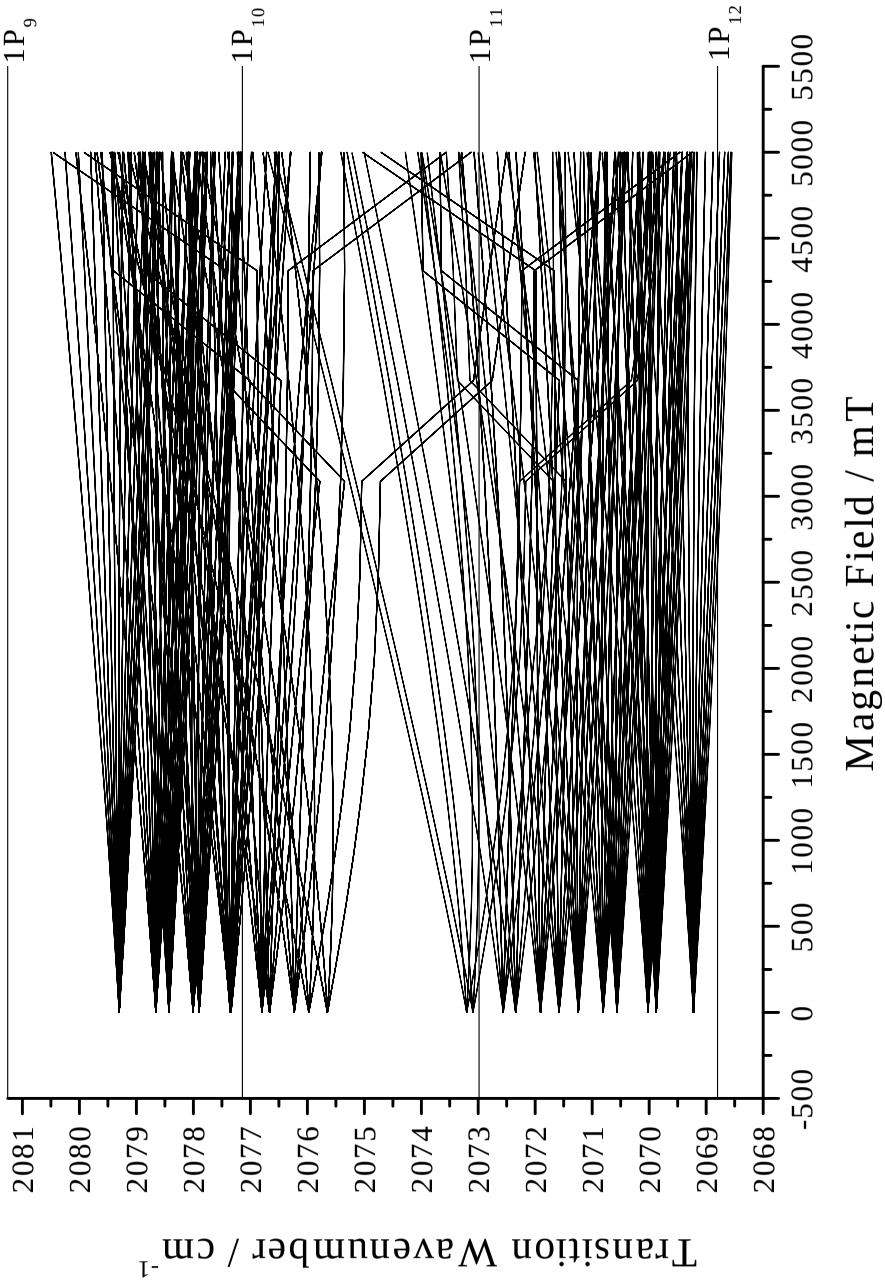

Figure 4.8: Zeeman pattern of the fine structure transitions in the ground state of iodine monoxide ($A_0 = -2073.5cm^{-1}$).

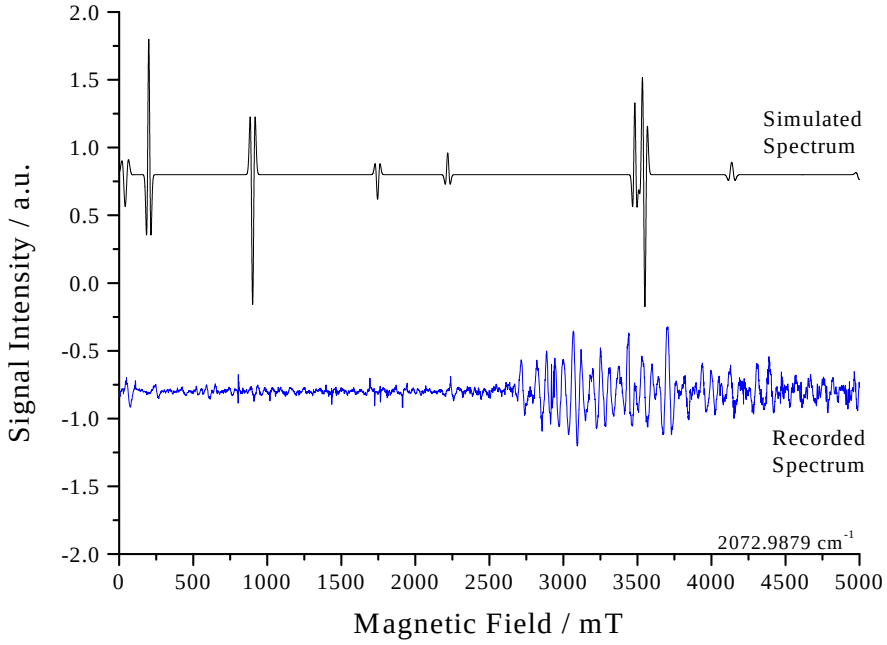

Figure 4.9: Simulated LMR spectrum of the fi ne structure transitions in the ground state of iodine monoxide ($A_0 = -2073.5cm^{-1}$) for the laser line $1P_{10}$.

the hyperfine structure is shown in figure (4.8)[9]. The horizontal lines mark the positions of the laser lines used for the experiment. In figure (4.8) the Q branch has not been included since the tuning rates for this kind of transition are rather low[10]. Due to this, the resulting signals would be very broad and the total intensity of the lines is distributed over a wide field region. In turn this leads to very weak signals so that usually the Q branch is not observed.

From these predictions, detailed simulations of the expected LMR spectra for the $1P_{10}$ (fig. (4.9)) and the $1P_{11}$ (fig. (4.10)) have been calculated. Since the large number of states leads to computational problems, it became necessary to limit I to $\frac{1}{2}$ and M_I to $\pm\frac{1}{2}$ in order to indicate the hyperfine structure at least. Furthermore no population factors are included in this simulation. Since the discharge plasma can be quite hot[11] this might indeed influence the intensity distribution significantly.

Comparing the spectra observed on the $1P_{10}$ and $1P_{11}$ with the calcu-

[9] More detailed graphs of P-, Q- and R-branch can be found in section D.2.

[10] cf. fi g. (D.23), page 139

[11] It is rather diffi cult to measure the temperature of the plasma itself but it can be estimated to be of the order of 400 to $500K$.

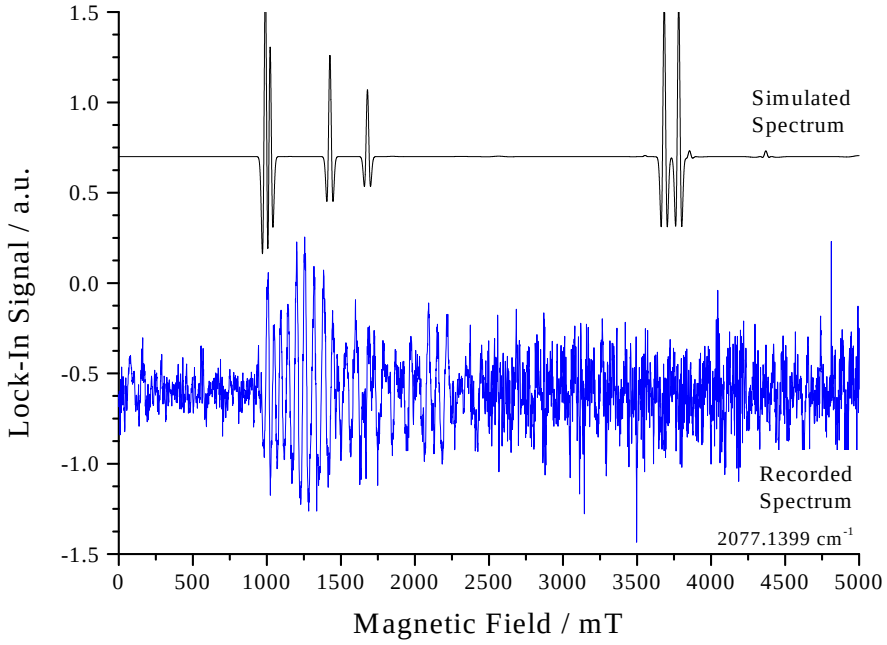

Figure 4.10: Simulated LMR spectrum of the fine structure transitions in the ground state of iodine monoxide ($A_0 = -2073.5cm^{-1}$) for the laser line $1P_{11}$.

lated patterns, one finds some similarities. First of all the gap observed on the $1P_{10}$ and $1P_{11}$ occurs in more or less the right region. Furthermore, the group of strong signals on the $1P_{10}$ between 1.0 and $2.2T$ is reproduced not too badly as well.

On the other hand, this interpretation is contradicted somewhat by several signals predicted for the $1P_{11}$. Especially the signals arising from the resonance of the $1P_{11}$ laser line and the $P_{\frac{3}{2}}$ transition in the region below $1000mT$ disturb the picture described above. As already indicated, this could well be caused by the population distribution that is not reproduced correctly. It is possible that states with very low J values are not populated strong enough to yield the intensity indicated by the simulation. This would affect the spectrum on the $1P_{11}$ where the resonance with the $P_{\frac{3}{2}}$ transition occurs at low field strengths. For these signals the intensity would be reduced. The same would be observed for the signals on the $1P_{10}$ laser line. Especially the signals above $3000mT$ would be reduced in intensity since they arise from the $R_{\frac{3}{2}}$ transition while the signals around $1000mT$ belong to the $R_{\frac{5}{2}}$.

Furthermore it was pointed out by E. A. Cohen that the $X^2\Pi_{\frac{1}{2}}(v=0)$ state may be perturbed by the $X^2\Pi_{\frac{3}{2}}(v=3)$ state [Coh01]. The $X^2\Pi_{\frac{3}{2}}(v=3)$ state is found at $1992.35cm^{-1}$ [Dur60, New98] above the vibrational ground state $X^2\Pi_{\frac{3}{2}}(v=0)$ so that the $X^2\Pi_{\frac{1}{2}}(v=0)$ state is less than $100cm^{-1}$ away. It also has got the right parity to perturb levels in the $\frac{1}{2}$ spin component of the electronic ground state. Therefore such a perturbation is indeed possible although it is expected to be rather weak because of Franck-Condon (vibrational overlap) effects.

In any case, the biggest source for the discrepancy between the simulations and the observed spectra remains the arbitrarily chosen value for A_0 but because of the previously mentioned unknown influences it seems virtually impossible to refine this value.

4.5 Summary of results

In the previous sections, the first observation of transitions combining both finestructure components of the electronic ground state $X^2\Pi_i$ of iodine monoxide has been reported. The observed spectra have been ascribed to IO because of the chemical characteristics of the reaction used for the production of the radical and because of the rich hyperfine structure. This hyperfine structure and the low rotational constant together result in blended signals that make the analysis by a least squares procedure impossible. Instead of this a simulation of the observed spectra was attempted. The quality of this simulation is limited by the computational effort necessary.

Despite of this the spin-orbit coupling constant A_0 can be estimated to a value between $-2072.5cm^{-1}$ and $-2074.5cm^{-1}$. Although the analysis remains somewhat unsatisfying, this result still resembles a substantial improvement compared with the previous known value of $-2091(40)cm^{-1}$.

Chapter 5

Conclusions

The LMR experiments on iodine have shown that this atom is a rather complex quantum mechanical system. All its excited states are obviously best described in J_cK vector coupling schemes. For an $s-coupled$ and an $s-decoupled$ basis set the necessary matrix elements were newly derived and a program was developed for analyzing the observed spectra.

As a first result of this derivation it was found that the characteristic hyperfine multiplet of an atom can vanish for excited states if the core angular momenta cancel each other to give a total core angular momentum of zero. This effect was found while analyzing a transition in chlorine atoms that was described by E. R. Comben in a previous study [Com86]. The simple model used by her did not take account of this effect so that her analysis became faulty. Therefore the analysis of this transition was corrected.

For the data newly presented in this study, it was possible to analyze three of the observed transitions ascribed to iodine. The analysis of the first of these transitions results in a parameter set that describes the observations quite satisfyingly. Here, the g factors and the hyperfine constants have been determined for the first time and were found to be very sensitive to perturbations of the electronic configuration. The nature of the other two transitions remains somewhat unclear.

High resolution spectroscopy of an atomic species in the mid infra-red has proven to be very sensitive to perturbations and thus can provide valuable information on excited states and their mutual perturbations.

For the investigation of iodine monoxide it was necessary to develop a suitable method for the production of iodine monoxide. Due to the rather high absorption frequency, it was furthermore necessary to use the CO-$v = (1 \rightarrow 0)$ laser. For the first time this type of laser was used in an LMR

experiment and introduced an additional difficulty to this experiment.

Due to the rich hyperfine structure of the molecule, a thorough analysis of the recorded spectra in form of a least squares fit was frustrated. The huge number of ro-vibrational states in combination with the hyperfine components leads to LMR spectra in which almost no signals are resolved. Instead a highly complicated pattern of signals that partially pile up and partially cancel each other is obtained.

In contrast to the previous determination of the spin-orbit splitting by M. K. Gilles *et al.* [Gil92], the transitions between the two spin-orbit components were observed directly for the first time. Although only a rather coarse value for the splitting has been obtained, this will still be useful to lead the way for future investigations. Since the technique of Laser Magnetic Resonance multiplies the number of observed transitions due to the Zeeman splitting, the use of different, field-free techniques might be able to resolve the hyperfine structure and would thus allow an accurate determination of the spin-orbit splitting.

Appendix A

Matrix Elements of Angular Momentum Operators

A.1 LS-coupled, I-decoupled Representation

- Simple Tensor Operators

  1. $T^1_p(\mathbf{L})$

     $< (L,S)J, M_J; I, M_I | T^1_p(\mathbf{L}) | (L',S')J', M'_{J'}; I', M'_{I'} >=$

     $$(-1)^{J-M_J+J'+L+S+1} \cdot \sqrt{(2J+1)(2J'+1)} \cdot \sqrt{L(L+1)(2L+1)} \cdot \begin{pmatrix} J & 1 & J' \\ -M_{\mathbf{J}} & p & M'_{\mathbf{J}} \end{pmatrix} \cdot \begin{Bmatrix} S & L & J \\ 1 & J' & L \end{Bmatrix} \cdot \delta_{LL'} \cdot \delta_{SS'} \cdot \delta_{II'} \cdot \delta_{M_{\mathbf{I}} M'_{\mathbf{I}}}$$

  2. $T^1_p(\mathbf{S})$

     $< (L,S)J, M_J; I, M_I | T^1_p(\mathbf{S}) | (L',S')J', M'_{J'}; I', M'_{I'} >=$

     $$(-1)^{2J-M_J+L+S+1} \cdot \sqrt{(2J+1)(2J'+1)} \cdot \sqrt{S(S+1)(2S+1)} \begin{pmatrix} J & 1 & J' \\ -M_{\mathbf{J}} & p & M'_{\mathbf{J}} \end{pmatrix} \cdot \begin{Bmatrix} L & S & J \\ 1 & J' & S \end{Bmatrix} \cdot \delta_{LL'} \cdot \delta_{SS'} \cdot \delta_{II'} \cdot \delta_{M_{\mathbf{I}} M'_{\mathbf{I}}}$$

- Scalar Products of Tensor Operators

  1. $T^1(\mathbf{L}).T^1(\mathbf{S})$

     $< (L,S)J, M_J; I, M_I | T^1(\mathbf{L}).T^1(\mathbf{S}) | (L',S')J', M'_{J'}; I', M'_{I'} >=$

     $$(-1)^{2J+2L+2S+1} \cdot \tfrac{1}{2} \cdot [L(L+1) + S(S+1) - J(J+1)] \cdot \delta_{LL'} \cdot \delta_{SS'} \cdot \delta_{JJ'} \cdot \delta_{M_{\mathbf{J}} M'_{\mathbf{J}}} \cdot \delta_{II'} \cdot \delta_{M_{\mathbf{I}} M'_{\mathbf{I}}}$$

2. $T^1(\mathbf{I}).T^1(\mathbf{L})$

$$< (L,S)J, M_J; I, M_I | T^1(\mathbf{I}).T^1(\mathbf{L}) | (L',S')J', M'_{J'}; I', M'_{I'} >=$$

$$\sum_{p=0,\pm1} (-1)^p \cdot (-1)^{I-M_I} \cdot (-1)^{J-M_J+J'+L+S+1} \cdot \sqrt{I(I+1)(2I+1)} \cdot \sqrt{(2J+1)(2J'+1)} \cdot \sqrt{L(L+1)(2L+1)} \cdot$$
$$\begin{pmatrix} I & 1 & I \\ -M_{\mathbf{I}} & p & M'_{\mathbf{I}} \end{pmatrix} \cdot \begin{pmatrix} J & 1 & J' \\ -M_{\mathbf{J}} & -p & M'_{\mathbf{J}} \end{pmatrix} \cdot \begin{Bmatrix} S & L & J \\ 1 & J' & L \end{Bmatrix} \cdot \delta_{LL'} \cdot \delta_{SS'} \cdot \delta_{II'}$$

3. $T^1(\mathbf{I}).T^1(\mathbf{S})$

$$< (L,S)J, M_J; I, M_I | T^1(\mathbf{I}).T^1(\mathbf{S}) | (L',S')J', M'_{J'}; I', M'_{I'} >=$$

$$\sum_{p=0,\pm1} (-1)^p \cdot (-1)^{I-M_I} \cdot (-1)^{2J-M_J+L+S+1} \cdot \sqrt{I(I+1)(2I+1)} \cdot \sqrt{(2J+1)(2J'+1)} \cdot \sqrt{S(S+1)(2S+1)} \cdot$$
$$\begin{pmatrix} I & 1 & I \\ -M_{\mathbf{I}} & p & M'_{\mathbf{I}} \end{pmatrix} \cdot \begin{pmatrix} J & 1 & J' \\ -M_{\mathbf{J}} & -p & M'_{\mathbf{J}} \end{pmatrix} \cdot \begin{Bmatrix} L & S & J \\ 1 & J' & S \end{Bmatrix} \cdot \delta_{LL'} \cdot \delta_{SS'} \cdot \delta_{II'}$$

4. $T^1(\mathbf{I}).T^1(\mathbf{S}, C^2)$

$$< (L,S)J, M_J; I, M_I | T^1(\mathbf{I}).T^1(\mathbf{S}, C^2) | (L',S')J', M'_{J'}; I', M'_{I'} >=$$

$$\sum_{p=0,\pm1} (-1)^p \cdot (-1)^{I-M_I+J-M_J+L} \cdot \sqrt{3} \cdot \sqrt{I(I+1)(2I+1)} \cdot \sqrt{S(S+1)(2S+1)} \cdot \sqrt{(2L+1)(2L'+1)} \cdot \sqrt{(2J+1)(2J'+1)} \cdot$$
$$\begin{pmatrix} I & 1 & I \\ -M_{\mathbf{I}} & p & M'_{\mathbf{I}} \end{pmatrix} \cdot \begin{pmatrix} J & 1 & J' \\ -M_{\mathbf{J}} & -p & M'_{\mathbf{J}} \end{pmatrix} \cdot \begin{pmatrix} L & 2 & L' \\ 0 & 0 & 0 \end{pmatrix} \cdot \begin{Bmatrix} L & L' & 2 \\ S & S & 1 \\ J & J' & 1 \end{Bmatrix} \cdot \delta_{SS'} \cdot \delta_{II'}$$

5. $T^2(\mathbf{Q}).T^2(\nabla\mathbf{E})$

$$< (L,S)J, M_J; I, M_I|T^2(\mathbf{Q}).T^2(\nabla\mathbf{E})|(L',S')J', M'_{J'}; I', M'_{I'} >=$$

$$\sum_{p=0,\pm1}(-1)^{p+I-M_\mathbf{I}+J-M_\mathbf{J}}\cdot(2J+1)\cdot\begin{pmatrix} I & 2 & I \\ M_\mathbf{I} & p & -M'_\mathbf{I}\end{pmatrix}\cdot\begin{pmatrix} J & 2 & J \\ M_\mathbf{J} & -p & -M'_\mathbf{J}\end{pmatrix}\begin{Bmatrix} S & L & J \\ 2 & J & L\end{Bmatrix}\cdot < I||T^2(\mathbf{Q})||I > \cdot < L||T^2(\nabla\mathbf{E})||L >$$
$$\cdot\delta_{LL'}\cdot\delta_{SS'}\cdot\delta_{JJ'}$$

A.2 $\mathbf{J}_c K$-coupled, s-coupled, I-decoupled Representation

- Basis Set

  The basis set used for the calculations in this coupling scheme is given by:
  $|(((L_c, S_c)J_c, l)K, s)J, M_J > \otimes |I, M_I >$

- Simple Tensor Operators

  1. $T^1_p(\mathbf{L}_c)$

     $< (((L_c, S_c)J_c, l)K, s)J, M_{\mathbf{J}}; I, M_{\mathbf{I}}|T^1_p(\mathbf{L}_c)|(((L'_c, S'_c)J'_c, l')K', s')J', M'_{\mathbf{J}}; I', M'_{\mathbf{I}} >=$

     $$(-1)^{J+J'-M_{\mathbf{J}}+K+K'+l+s+J_c+J'_c+L_c+S_c+3} \cdot \sqrt{(2J+1)(2J'+1)} \cdot \sqrt{(2K+1)(2K'+1)} \cdot \sqrt{(2J_c+1)(2J'_c+1)} \cdot \sqrt{L_c(L_c+1)(2L_c+1)} \cdot$$
     $$\begin{pmatrix} J & 1 & J' \\ -M_{\mathbf{J}} & p & M'_{\mathbf{J}} \end{pmatrix} \cdot \begin{Bmatrix} s & K & J \\ 1 & J' & K' \end{Bmatrix} \cdot \begin{Bmatrix} l & J_c & K \\ 1 & K' & J'_c \end{Bmatrix} \cdot \begin{Bmatrix} S_c & L_c & J_c \\ 1 & J'_c & L'_c \end{Bmatrix} \cdot \delta_{L_c L'_c} \cdot \delta_{S_c S'_c} \cdot \delta_{ll'} \cdot \delta_{ss'} \cdot \delta_{II'} \cdot \delta_{M_{\mathbf{I}} M'_{\mathbf{I}}}$$

  2. $T^1_p(\mathbf{S}_c)$

     $< (((L_c, S_c)J_c, l)K, s)J, M_{\mathbf{J}}; I, M_{\mathbf{I}}|T^1_p(\mathbf{S}_c)|(((L'_c, S'_c)J'_c, l')K', s')J', M'_{\mathbf{J}}; I', M'_{\mathbf{I}} >=$

     $$(-1)^{J+J'-M_{\mathbf{J}}+K+K'+l+s+2J_c+L_c+S_c+3} \cdot \sqrt{(2J+1)(2J'+1)} \cdot \sqrt{(2K+1)(2K'+1)} \cdot \sqrt{(2J_c+1)(2J'_c+1)} \cdot \sqrt{S_c(S_c+1)(2S_c+1)} \cdot$$
     $$\begin{pmatrix} J & 1 & J' \\ -M_{\mathbf{J}} & p & M'_{\mathbf{J}} \end{pmatrix} \cdot \begin{Bmatrix} s & K & J \\ 1 & J' & K' \end{Bmatrix} \cdot \begin{Bmatrix} l & J_c & K \\ 1 & K' & J'_c \end{Bmatrix} \cdot \begin{Bmatrix} L_c & S_c & J_c \\ 1 & J'_c & S_c \end{Bmatrix} \cdot \delta_{L_c L'_c} \cdot \delta_{S_c S'_c} \cdot \delta_{ll'} \cdot \delta_{ss'} \cdot \delta_{II'} \cdot \delta_{M_{\mathbf{I}} M'_{\mathbf{I}}}$$

3. $T^1_p(\mathbf{l})$

$$< (((L_c,S_c)J_c,l)K,s)J,M_{\mathbf{J}};I,M_{\mathbf{I}}|T^1_p(\mathbf{l})|(((L'_c,S'_c)J'_c,l')K',s')J',M'_{\mathbf{J}};I',M'_{\mathbf{I}}>=$$

$$(-1)^{J+J'-M_{\mathbf{J}}+2K+s+J_c+l+2}\cdot\sqrt{(2J+1)(2J'+1)}\cdot\sqrt{(2K+1)(2K'+1)}\cdot\sqrt{(l(l+1)(2l+1)}\cdot$$
$$\begin{pmatrix} J & 1 & J' \\ -M_{\mathbf{J}} & p & M'_{\mathbf{J}} \end{pmatrix}\cdot\begin{Bmatrix} s & K & J \\ 1 & J' & K' \end{Bmatrix}\cdot\begin{Bmatrix} J_c & l & K \\ 1 & K' & l \end{Bmatrix}\cdot\delta_{L_cL'_c}\cdot\delta_{S_cS'_c}\cdot\delta_{J_cJ'_c}\cdot\delta_{ll'}\cdot\delta_{ss'}\cdot\delta_{II'}\cdot\delta_{M_{\mathbf{I}}M'_{\mathbf{I}}}$$

4. $T^1_p(\mathbf{s})$

$$< (((L_c,S_c)J_c,l)K,s)J,M_{\mathbf{J}};I,M_{\mathbf{I}}|T^1_p(\mathbf{s})|(((L'_c,S'_c)J'_c,l')K',s')J',M'_{\mathbf{J}};I',M'_{\mathbf{I}}>=$$

$$(-1)^{2J-M_{\mathbf{J}}+K'+s+1}\cdot\sqrt{(2J+1)(2J'+1)}\cdot\sqrt{s(s+1)(2s+1)}\cdot$$
$$\begin{pmatrix} J & 1 & J' \\ -M_{\mathbf{J}} & p & M'_{\mathbf{J}} \end{pmatrix}\cdot\begin{Bmatrix} K & s & J \\ 1 & J' & s \end{Bmatrix}\cdot\delta_{L_cL'_c}\cdot\delta_{S_cS'_c}\cdot\delta_{J_cJ'_c}\cdot\delta_{ll'}\cdot\delta_{ss'}\cdot\delta_{KK'}\cdot\delta_{II'}\cdot\delta_{M_{\mathbf{I}}M'_{\mathbf{I}}}$$

- Scalar Products of Tensor Operators

1. $T^1(\mathbf{l}).T^1(\mathbf{s})$

$$< (((L_c,S_c)J_c,l)K,s)J,M_{\mathbf{J}};I,M_{\mathbf{I}}|T^1(\mathbf{l}).T^1(\mathbf{s})|(((L'_c,S'_c)J'_c,l')K',s')J',M'_{\mathbf{J}};I',M'_{\mathbf{I}}>=$$

$$(-1)^{J+K+K'+J_c+l+s+1}\cdot\sqrt{s(s+1)(2s+1)}\cdot\sqrt{l(l+1)(2l+1)}\cdot\sqrt{(2K+1)(2K'+1)}\cdot$$
$$\begin{Bmatrix} J & s & K \\ 1 & K' & s \end{Bmatrix}\cdot\begin{Bmatrix} J_c & l & K \\ 1 & K' & l \end{Bmatrix}\cdot\delta_{L_cL'_c}\cdot\delta_{S_cS'_c}\cdot\delta_{J_cJ'_c}\cdot\delta_{ll'}\cdot\delta_{ss'}\cdot\delta_{JJ'}\cdot\delta_{II'}\cdot\delta_{M_{\mathbf{I}}M'_{\mathbf{I}}}$$

2. $T^1(\mathbf{I}).T^1(\mathbf{L}_c)$

$$< (((L_c,S_c)J_c,l)K,s)J,M_{\mathbf{J}};I,M_{\mathbf{I}}|T^1(\mathbf{I}).T^1(\mathbf{L}_c)|(((L'_c,S'_c)J'_c,l')K',s')J',M'_{\mathbf{J}};I',M'_{\mathbf{I}}>=$$

$$\sum_{p=0,\pm1}(-1)^{p+I-M_{\mathbf{I}}+J+J'-M_{\mathbf{J}}+K+K'+J_c+J'_c+L_c+S_c+l+s+3}\cdot\sqrt{I(I+1)(2I+1)}\cdot\sqrt{L_c(L_c+1)(2L_c+1)}\cdot$$
$$\sqrt{(2J+1)(2J'+1)}\cdot\sqrt{(2K+1)(2K'+1)}\cdot\sqrt{(2J_c+1)(2J'_c+1)}\cdot\begin{pmatrix} I & 1 & I \\ -M_{\mathbf{I}} & p & M'_{\mathbf{I}}\end{pmatrix}\cdot\begin{pmatrix} J & 1 & J' \\ -M_{\mathbf{J}} & -p & M'_{\mathbf{J}}\end{pmatrix}\cdot$$
$$\begin{Bmatrix} s & K & J \\ 1 & J' & K'\end{Bmatrix}\cdot\begin{Bmatrix} l & J_c & K \\ 1 & K' & J'_c\end{Bmatrix}\cdot\begin{Bmatrix} S_c & L_c & J_c \\ 1 & J'_c & L_c\end{Bmatrix}\cdot\delta_{L_cL'_c}\cdot\delta_{S_cS'_c}\cdot\delta_{ll'}\cdot\delta_{ss'}\cdot\delta_{II'}$$

3. $T^1(\mathbf{I}).T^1(\mathbf{S}_c)$

$$< (((L_c,S_c)J_c,l)K,s)J,M_{\mathbf{J}};I,M_{\mathbf{I}}|T^1(\mathbf{I}).T^1(\mathbf{S}_c)|(((L'_c,S'_c)J'_c,l')K',s')J',M'_{\mathbf{J}};I',M'_{\mathbf{I}}>=$$

$$\sum_{p=0,\pm1}(-1)^{p+I-M_{\mathbf{I}}+J+J'-M_{\mathbf{J}}+K+K'+2J_c+L'_c+S'_c+l+s+3}\cdot\sqrt{I(I+1)(2I+1)}\cdot\sqrt{S_c(S_c+1)(2S_c+1)}\cdot$$
$$\sqrt{(2J+1)(2J'+1)}\cdot\sqrt{(2K+1)(2K'+1)}\cdot\sqrt{(2J_c+1)(2J'_c+1)}\cdot\begin{pmatrix} I & 1 & I \\ -M_{\mathbf{I}} & p & M'_{\mathbf{I}}\end{pmatrix}\cdot\begin{pmatrix} J & 1 & J' \\ -M_{\mathbf{J}} & -p & M'_{\mathbf{J}}\end{pmatrix}\cdot$$
$$\begin{Bmatrix} s & K & J \\ 1 & J' & K'\end{Bmatrix}\cdot\begin{Bmatrix} l & J_c & K \\ 1 & K' & J'_c\end{Bmatrix}\cdot\begin{Bmatrix} L_c & S_c & J_c \\ 1 & J'_c & S_c\end{Bmatrix}\cdot\delta_{L_cL'_c}\cdot\delta_{S_cS'_c}\cdot\delta_{ll'}\cdot\delta_{ss'}\cdot\delta_{II'}$$

4. $T^1(\mathbf{I}).T^1(\mathbf{S}_c, C^2)$

$$< (((L_c, S_c)J_c, l)K, s)J, M_{\mathbf{J}}; I, M_{\mathbf{I}}|T^1(\mathbf{I}).T^1(\mathbf{S}_c, C^2)|(((L'_c, S'_c)J'_c, l')K', s')J', M'_{\mathbf{J}}; I', M'_{\mathbf{I}} >=$$

$$\sum_{p=0,\pm1}(-1)^{p+I-M_{\mathbf{I}}+J-M_{\mathbf{J}}+J'+K+K'+l+s+J_c}\cdot\sqrt{I(I+1)(2I+1)}\cdot\sqrt{S_c(S_c+1)(2S_c+1)}\cdot\sqrt{(2J+1)(2J'+1)}\cdot$$
$$\sqrt{(2K+1)(2K'+1)}\cdot\sqrt{(2L_c+1)(2L'_c+1)}\cdot\sqrt{(2J_c+1)(2J'_c+1)}\cdot\sqrt{3}\cdot\begin{pmatrix} I & 1 & I \\ -M_{\mathbf{I}} & p & M'_{\mathbf{I}}\end{pmatrix}\cdot\begin{pmatrix} J & 1 & J' \\ -M_{\mathbf{J}} & -p & M'_{\mathbf{J}}\end{pmatrix}\cdot$$
$$\begin{pmatrix} L_c & 2 & L'_c \\ 0 & 0 & 0\end{pmatrix}\cdot\begin{Bmatrix} s & K & J \\ 1 & J' & K'\end{Bmatrix}\cdot\begin{Bmatrix} l & J_c & K \\ 1 & K' & J'_c\end{Bmatrix}\cdot\begin{Bmatrix} L_c & L'_c & 2 \\ S_c & S'_c & 1 \\ J_c & J'_c & 1\end{Bmatrix}\cdot\delta_{S_cS'_c}\cdot\delta_{ll'}\cdot\delta_{ss'}\cdot\delta_{II'}$$

5. $T^2(\mathbf{Q}).T^2(\nabla\mathbf{E})$

$$< (((L_c, S_c)J_c, l)K, s)J, M_{\mathbf{J}}; I, M_{\mathbf{I}}|T^2(\mathbf{Q}).T^2(\nabla\mathbf{E})|(((L'_c, S'_c)J'_c, l')K', s')J', M'_{\mathbf{J}}; I', M'_{\mathbf{I}} >=$$

$$\sum_{p=0,\pm1}(-1)^{p+I-M_{\mathbf{I}}+J-M_{\mathbf{J}}+J'+K+K'+l+s+L_c+S_c+2J_c}\cdot\sqrt{(2J+1)(2J'+1)}\cdot\sqrt{(2K+1)(2K'+1)}\cdot(2J_c+1)\cdot$$
$$\begin{pmatrix} I & 2 & I \\ M_{\mathbf{I}} & p & -M'_{\mathbf{I}}\end{pmatrix}\cdot\begin{pmatrix} J & 2 & J \\ M_{\mathbf{J}} & -p & -M'_{\mathbf{J}}\end{pmatrix}\cdot\begin{Bmatrix} s & K & J \\ 2 & J' & K'\end{Bmatrix}\cdot\begin{Bmatrix} l & J_c & K \\ 2 & K' & J_c\end{Bmatrix}\cdot\begin{Bmatrix} S_c & L_c & J_c \\ 2 & J_c & L_c\end{Bmatrix}$$
$$\cdot < I||T^2(\mathbf{Q})||I > \cdot < L_c||T^2(\nabla\mathbf{E})||L_c > \cdot\delta_{L_cL'_c}\cdot\delta_{S_cS'_c}\cdot\delta_{J_cJ'_c}\cdot\delta_{ll'}\cdot\delta_{ss'}\cdot\delta_{II'}$$

A.3 $\mathbf{J}_c K$-coupled, s-decoupled, I-decoupled Representation

- Basis Set

  The basis set used for the calculations in this coupling scheme is given by:
  $|((L_c, S_c)J_c, l)K, M_K > \otimes |s, m_s > \otimes |I, M_I >$

- Simple Tensor Operators

  1. $T^1_p(\mathbf{L}_c)$

     $< ((L_c, S_c)J_c, l)K, M_K; s, m_s; I, M_I | T^1_p(\mathbf{L}_c) | ((L'_c, S'_c)J'_c, l')K', M'_K; s', m'_s; I, M'_I >=$

     $$(-1)^{K-M_{\mathbf{K}}+K'+J_c+J'_c+L_c+S_c+l+2} \cdot \sqrt{L_c(L_c+1)(2L_c+1)} \cdot \sqrt{(2K+1)(2K'+1)} \cdot \sqrt{(2J_c+1)(2J'_c+1)} \cdot \begin{pmatrix} K & 1 & K' \\ -M_{\mathbf{K}} & p & M'_{\mathbf{K}} \end{pmatrix} \cdot \begin{Bmatrix} l & J_c & K \\ 1 & K' & J'_c \end{Bmatrix} \cdot \begin{Bmatrix} S_c & L_c & J_c \\ 1 & J'_c & L_c \end{Bmatrix} \cdot \delta_{L_c L'_c} \cdot \delta_{S_c S'_c} \cdot \delta_{ll'} \cdot \delta_{II'} \cdot \delta_{M_{\mathbf{I}} M'_{\mathbf{I}}} \cdot \delta_{ss'} \cdot \delta_{m_{\mathbf{s}} m'_{\mathbf{s}}}$$

  2. $T^1_p(\mathbf{S}_c)$

     $< ((L_c, S_c)J_c, l)K, M_K; s, m_s; I, M_I | T^1_p(\mathbf{S}_c) | ((L'_c, S'_c)J'_c, l')K', M'_K; s', m'_s; I, M'_I >=$

     $$(-1)^{K-M_{\mathbf{K}}+K'+2J_c+L_c+S_c+l+2} \cdot \sqrt{S_c(S_c+1)(2S_c+1)} \cdot \sqrt{(2K+1)(2K'+1)} \cdot \sqrt{(2J_c+1)(2J'_c+1)} \cdot \begin{pmatrix} K & 1 & K' \\ -M_{\mathbf{K}} & p & M'_{\mathbf{K}} \end{pmatrix} \cdot \begin{Bmatrix} l & J_c & K \\ 1 & K' & J'_c \end{Bmatrix} \cdot \begin{Bmatrix} L_c & S_c & J_c \\ 1 & J'_c & S_c \end{Bmatrix} \cdot \delta_{L_c L'_c} \cdot \delta_{S_c S'_c} \cdot \delta_{ll'} \cdot \delta_{II'} \cdot \delta_{M_{\mathbf{I}} M'_{\mathbf{I}}} \cdot \delta_{ss'} \cdot \delta_{m_{\mathbf{s}} m'_{\mathbf{s}}}$$

3. $T^1_p(\mathbf{l})$

$$< ((L_c,S_c)J_c,l)K,M_K;s,m_s;I,M_I|T^1_p(\mathbf{l})|((L'_c,S'_c)J'_c,l')K',M'_K;s',m'_s;I,M'_I >=$$

$$(-1)^{2K-M_{\mathbf{K}}+J'_c+l'+1}\cdot\sqrt{l(l+1)(2l+1)}\cdot\sqrt{(2K+1)(2K'+1)}\cdot \begin{pmatrix} K & 1 & K' \\ -M_{\mathbf{K}} & p & M'_{\mathbf{K}} \end{pmatrix}\cdot\begin{Bmatrix} J_c & l & K \\ 1 & K' & l \end{Bmatrix}\cdot\delta_{L_cL'_c}\cdot\delta_{S_cS'_c}\cdot\delta_{J_cJ'_c}\cdot\delta_{ll'}\cdot\delta_{II'}\cdot\delta_{M_{\mathbf{I}}M'_{\mathbf{I}}}\cdot\delta_{ss'}\cdot\delta_{m_{\mathbf{s}}m'_{\mathbf{s}}}$$

4. $T^1_p(\mathbf{s})$

$$< ((L_c,S_c)J_c,l)K,M_K;s,m_s;I,M_I|T^1_p(\mathbf{s})|((L'_c,S'_c)J'_c,l')K',M'_K;s',m'_s;I,M'_I >=$$

$$(-1)^{s-m_{\mathbf{s}}}\cdot\sqrt{s(s+1)(2s+1)}\cdot\begin{pmatrix} s & 1 & s' \\ -m_{\mathbf{s}} & p & m'_{\mathbf{s}} \end{pmatrix}\cdot\delta_{L_cL'_c}\cdot\delta_{S_cS'_c}\cdot\delta_{J_cJ'_c}\cdot\delta_{ll'}\cdot\delta_{II'}\cdot\delta_{M_{\mathbf{I}}M'_{\mathbf{I}}}\cdot\delta_{KK'}\cdot\delta_{M_{\mathbf{K}}M'_{\mathbf{K}}}$$

- Scalar Products of Tensor Operators

1. $T^1(\mathbf{l}).T^1(\mathbf{s})$

$$< ((L_c,S_c)J_c,l)K,M_K;s,m_s;I,M_I|T^1(\mathbf{l}).T1^1(\mathbf{s})|((L'_c,S'_c)J'_c,l')K',M'_K;s',m'_s;I,M'_I >=$$

$$\sum_{p=0,\pm1}(-1)^{p+2K-M_{\mathbf{K}}+s-m_{\mathbf{s}}+J'_c+l'+1}\cdot\sqrt{(2K+1)(2K'+1)}\cdot\sqrt{l(l+1)(2l+1)}\cdot\sqrt{s(s+1)(2s+1)}\cdot \begin{pmatrix} K & 1 & K' \\ -M_{\mathbf{K}} & p & M'_{\mathbf{K}} \end{pmatrix}\cdot\begin{pmatrix} s & 1 & s \\ -m_{\mathbf{s}} & -p & m'_{\mathbf{s}} \end{pmatrix}\cdot\begin{Bmatrix} J_c & l & K \\ 1 & K' & l \end{Bmatrix}\cdot\delta_{L_cL'_c}\cdot\delta_{S_cS'_c}\cdot\delta_{J_cJ'_c}\cdot\delta_{ll'}\cdot\delta_{ss'}\cdot\delta_{II'}\cdot\delta_{M_{\mathbf{I}}M'_{\mathbf{I}}}$$

2. $T^1(\mathbf{I}).T^1(\mathbf{L}_c)$

$< ((L_c, S_c)J_c, l)K, M_K; s, m_s; I, M_I | T^1(\mathbf{I}).T1^1(\mathbf{L}_c) | ((L'_c, S'_c)J'_c, l')K', M'_K; s', m'_s; I, M'_I >=$

$$\sum_{p=0,\pm1} (-1)^{p+I-M_{\mathbf{I}}+K+K'-M_{\mathbf{K}}+J_c+J'_c+L_c+S_c+l+2} \cdot \sqrt{(2K+1)(2K'+1)} \cdot \sqrt{(2J_c+1)(2J'_c+1)} \cdot \sqrt{I(I+1)(2I+1)} \cdot$$
$$\sqrt{L_c(L_c+1)(2L_c+1)} \cdot \begin{pmatrix} I & 1 & I \\ -M_{\mathbf{I}} & p & M'_{\mathbf{I}} \end{pmatrix} \cdot \begin{pmatrix} K & 1 & K' \\ -M_{\mathbf{K}} & -p & M'_{\mathbf{K}} \end{pmatrix} \cdot \begin{Bmatrix} l & J_c & K \\ 1 & K' & J'_c \end{Bmatrix} \cdot \begin{Bmatrix} S_c & L_c & J_c \\ 1 & J'_c & L_c \end{Bmatrix} \cdot$$
$$\delta_{L_c L'_c} \cdot \delta_{S_c S'_c} \cdot \delta_{ll'} \cdot \delta_{II'} \cdot \delta_{ss'} \cdot \delta_{m_{\mathbf{s}} m'_{\mathbf{s}}}$$

3. $T^1(\mathbf{I}).T^1(\mathbf{S}_c)$

$< ((L_c, S_c)J_c, l)K, M_K; s, m_s; I, M_I | T^1(\mathbf{I}).T1^1(\mathbf{S}_c) | ((L'_c, S'_c)J'_c, l')K', M'_K; s', m'_s; I, M'_I >=$

$$\sum_{p=0,\pm1} (-1)^{p+I-M_{\mathbf{I}}+K+K'-M_{\mathbf{K}}+2J_c+L_c+S_c+l+2} \cdot \sqrt{(2K+1)(2K'+1)} \cdot \sqrt{(2J_c+1)(2J'_c+1)} \cdot \sqrt{I(I+1)(2I+1)} \cdot$$
$$\sqrt{S_c(S_c+1)(2S_c+1)} \cdot \begin{pmatrix} I & 1 & I \\ -M_{\mathbf{I}} & p & M'_{\mathbf{I}} \end{pmatrix} \cdot \begin{pmatrix} K & 1 & K' \\ -M_{\mathbf{K}} & -p & M'_{\mathbf{K}} \end{pmatrix} \cdot \begin{Bmatrix} l & J_c & K \\ 1 & K' & J'_c \end{Bmatrix} \cdot \begin{Bmatrix} L_c & S_c & J_c \\ 1 & J'_c & S_c \end{Bmatrix}$$
$$\cdot \delta_{L_c L'_c} \cdot \delta_{S_c S'_c} \cdot \delta_{ll'} \cdot \delta_{II'} \cdot \delta_{ss'} \cdot \delta_{m_{\mathbf{s}} m'_{\mathbf{s}}}$$

4. $T^1(\mathbf{I}).T^1(\mathbf{S}_c, C^2)$

$$< ((L_c, S_c)J_c, l)K, M_K; s, m_s; I, M_I|T^1(\mathbf{l}).T1^1(\mathbf{s})|((L'_c, S'_c)J'_c, l')K', M'_K; s', m'_s; I, M'_I >=$$

$$\sum_{p=0,\pm1}(-1)^{p+I-M_{\mathbf{I}}+K-M_{\mathbf{K}}+K'+J_c+L_c+l+1}\cdot\sqrt{I(I+1)(2I+1)}\cdot\sqrt{S_c(S_c+1)(2S_c+1)}\cdot\sqrt{(2K+1)(2K'+1)}\cdot$$
$$\sqrt{(2J_c+1)(2J'_c+1)}\cdot\sqrt{(2L_c+1)(2L'_c+1)}\cdot\begin{pmatrix} I & 1 & I \\ -M_{\mathbf{I}} & p & M'_{\mathbf{I}}\end{pmatrix}\cdot\begin{pmatrix} K & 1 & K' \\ -M_{\mathbf{K}} & -p & M'_{\mathbf{K}}\end{pmatrix}\cdot\begin{pmatrix} L_c & 2 & L'_c \\ 0 & 0 & 0\end{pmatrix}\cdot$$
$$\begin{Bmatrix} l & J_c & K \\ 1 & K' & J'_c\end{Bmatrix}\cdot\begin{Bmatrix} L_c & L'_c & 2 \\ S_c & S_c & 1 \\ J_c & J'_c & 1\end{Bmatrix}\cdot\delta_{S_cS'_c}\cdot\delta_{ll'}\cdot\delta_{ss'}\cdot\delta_{m_{\mathbf{s}}m'_{\mathbf{s}}}\cdot\delta_{II'}$$

5. $T^2(\mathbf{Q}).T^2(\nabla\mathbf{E})$

$$< ((L_c, S_c)J_c, l)K, M_K; s, m_s; I, M_I|T^2(\mathbf{Q}).T^2(\nabla\mathbf{E})|((L'_c, S'_c)J'_c, l')K', M'_K; s', m'_s; I, M'_I >=$$

$$\sum_{p=0,\pm1}(-1)^{p+I-M_{\mathbf{I}}+K-M_{\mathbf{K}}+l+L_c+S_c+2J_c}\cdot\sqrt{(2K+1)(2K'+1)}\cdot(2J_c+1)\cdot$$
$$\begin{pmatrix} I & 2 & I \\ M_{\mathbf{I}} & p & M'_{\mathbf{I}}\end{pmatrix}\cdot\begin{pmatrix} K & 2 & K' \\ M_{\mathbf{K}} & -p & M'_{\mathbf{K}}\end{pmatrix}\cdot\begin{Bmatrix} l & J_c & K \\ 2 & K' & J_c\end{Bmatrix}\cdot\begin{Bmatrix} S_c & L_c & J_c \\ 2 & J_c & L_c\end{Bmatrix}\cdot$$
$$< I||T^2(\mathbf{Q})|I > \cdot < L_c||T^2(\nabla\mathbf{E})||L_c > \cdot\delta_{L_cL'_c}\cdot\delta_{S_cS'_c}\cdot\delta_{J_cJ'_c}\cdot\delta_{ll'}\cdot\delta_{ss'}\cdot\delta_{m_{\mathbf{s}}m'_{\mathbf{s}}}\cdot\delta_{II'}$$

Appendix B

Test Transition of Chlorine Atoms

B.1.1 Signals of the test transition in chlorine

M'_J	M''_J	$M_{\mathbf{I}}$	$M_{\mathbf{I}}$	$\tilde{\nu}_{Laser}$	B	Wgt	$obs.-calc.$	$calc.TR$
		[Com86]	corr.	cm^{-1}	mT		$10^{-3}cm^{-1}$	$\frac{MHz}{mT}$
0.5	1.5	1.5	1.5	1493.5011	1351.7	1	-0.71	-1.95
0.5	1.5	0.5	0.5	1493.5011	1366.4	1	0.05	-1.95
0.5	1.5	-0.5	-0.5	1493.5011	1381.5	1	1.06	-1.95
0.5	1.5	-1.5	-1.5	1493.5011	1395.3	1	1.23	-1.95
-0.5	0.5	1.5	1.5	1493.5011	1611.6	0	4.61	-1.66
-0.5	0.5	0.5	0.5	1493.5011	1611.6	0	1.68	-1.66
-0.5	0.5	-0.5	-0.5	1493.5011	1611.6	0	-1.25	-1.66
-0.5	0.5	-1.5	-1.5	1493.5011	1611.6	0	-4.18	-1.66
-1.5	-0.5	1.5	1.5	1493.5011	1951.0	0	-3.59	-1.37
-1.5	-0.5	0.5	0.5	1493.5011	1951.0	0	-0.66	-1.37
-1.5	-0.5	-0.5	-0.5	1493.5011	1951.0	0	2.27	-1.37
-1.5	-0.5	-1.5	-1.5	1493.5011	1951.0	0	5.20	-1.37
-2.5	-1.5	1.5	-1.5	1493.5011	2425.7	1	-1.65	-1.08
-2.5	-1.5	0.5	-0.5	1493.5011	2449.2	1	-1.95	-1.08
-2.5	-1.5	-0.5	0.5	1493.5011	2474.1	1	-1.74	-1.08
-2.5	-1.5	-1.5	1.5	1493.5011	2499.3	1	-1.43	-1.08

Table B.1: Observations of the transition $(^3P_0)4d[2]_{2^1/_2} \leftarrow (^3P)5p^2P_{3/_2}$ in chlorine atoms according to [Com86]. This transition has been used for testing the software "Hamiltonian" developed for analyzing the transitions in I *. The original assignment of the hyperfine quantum numbers is given in the third column while the corrected assignment is given in column #4.

M_J'	M_J''	$M_{\mathbf{I}}$	$M_{\mathbf{I}}$	$\tilde{\nu}_{Laser}$	B	Wgt	$obs.-calc.$	$calc.TR$
		[Com86]	corr.	cm^{-1}	mT		$10^{-3}cm^{-1}$	$\frac{MHz}{mT}$
0.5	1.5	1.5	1.5	1493.8128	871.3	1	-0.97	-1.95
0.5	1.5	0.5	0.5	1493.8128	886.1	1	-0.16	-1.95
0.5	1.5	-0.5	-0.5	1493.8128	900.9	1	0.66	-1.95
0.5	1.5	-1.5	-1.5	1493.8128	914.3	1	0.57	-1.95
-0.5	0.5	1.5	1.5	1493.8128	1047.9	0	4.35	-1.66
-0.5	0.5	0.5	0.5	1493.8128	1047.9	0	1.42	-1.66
-0.5	0.5	-0.5	-0.5	1493.8128	1047.9	0	-1.52	-1.66
-0.5	0.5	-1.5	-1.5	1493.8128	1047.9	0	-4.45	-1.66
-1.5	-0.5	1.5	1.5	1493.8128	1266.5	0	-5.02	-1.37
-1.5	-0.5	0.5	0.5	1493.8128	1266.5	0	-2.08	-1.37
-1.5	-0.5	-0.5	-0.5	1493.8128	1266.5	0	0.85	-1.37
-1.5	-0.5	-1.5	-1.5	1493.8128	1266.5	0	3.78	-1.37
-2.5	-1.5	1.5	-1.5	1493.8128	1562.3	1	-2.05	-1.08
-2.5	-1.5	0.5	-0.5	1493.8128	1585.9	1	-2.31	-1.08
-2.5	-1.5	-0.5	0.5	1493.8128	1610.5	1	-2.21	-1.08
-2.5	-1.5	-1.5	1.5	1493.8128	1635.7	1	-1.90	-1.08
0.5	1.5	1.5	1.5	1493.8280	846.6	1	-1.81	-1.95
0.5	1.5	0.5	0.5	1493.8280	861.6	1	-0.87	-1.95
0.5	1.5	-0.5	-0.5	1493.8280	876.4	1	-0.05	-1.95
0.5	1.5	-1.5	-1.5	1493.8280	890.2	1	0.12	-1.95
-0.5	0.5	1.5	1.5	1493.8280	1021.8	0	5.10	-1.66
-0.5	0.5	0.5	0.5	1493.8280	1021.8	0	2.17	-1.66
-0.5	0.5	-0.5	-0.5	1493.8280	1021.8	0	-0.76	-1.66
-0.5	0.5	-1.5	-1.5	1493.8280	1021.8	0	-3.69	-1.66

Table B.1: Observations of the transition: $(^3P_0)4d[2]_{2^1/_2} \leftarrow (^3P)5p^2P_{3/_2}$ in chlorine atoms according to [Com86]. (continued)

M'_J	M''_J	$M_{\mathbf{I}}$	$M_{\mathbf{I}}$	$\tilde{\nu}_{Laser}$	B	Wgt	$obs.-calc.$	$calc.TR$
		[Com86]	corr.	cm^{-1}	mT		$10^{-3}cm^{-1}$	$\frac{MHz}{mT}$
-1.5	-0.5	1.5	1.5	1493.8280	1240.2	0	-1.85	-1.37
-1.5	-0.5	0.5	0.5	1493.8280	1240.2	0	1.09	-1.37
-1.5	-0.5	-0.5	-0.5	1493.8280	1240.2	0	4.02	-1.37
-1.5	-0.5	-1.5	-1.5	1493.8280	1240.2	0	6.95	-1.37
-2.5	-1.5	0.5	-1.5	1493.8280	1543.6	1	6.39	-1.08
-2.5	-1.5	-0.5	-0.5	1493.8280	1568.6	1	6.63	-1.08
-2.5	-1.5	-1.5	0.5	1493.8280	1589.6	1	5.43	-1.08
-0.5	-1.5	1.5	1.5	1494.5332	195.5	1	0.27	1.95
-0.5	-1.5	0.5	0.5	1494.5332	208.3	1	0.76	1.95
-0.5	-1.5	-0.5	-0.5	1494.5332	223.1	1	-0.06	1.95
0.5	-0.5	1.5	1.5	1494.5332	247.5	0	-0.95	1.66
0.5	-0.5	0.5	0.5	1494.5332	247.5	0	1.98	1.66
0.5	-0.5	-0.5	-0.5	1494.5332	247.5	0	4.92	1.66
0.5	-0.5	-1.5	-1.5	1494.5332	247.5	0	7.85	1.66
1.5	0.5	1.5	1.5	1494.5332	305.9	0	4.88	1.37
1.5	0.5	0.5	0.5	1494.5332	305.9	0	1.95	1.37
1.5	0.5	-0.5	-0.5	1494.5332	305.9	0	-0.98	1.37
1.5	0.5	-1.5	-1.5	1494.5332	305.9	0	-3.91	1.37
2.5	1.5	1.5	-1.5	1494.5332	354.1	1	-0.77	1.08
2.5	1.5	0.5	-0.5	1494.5332	379.7	1	-1.23	1.08
2.5	1.5	-0.5	0.5	1494.5332	403.3	1	-0.97	1.08
2.5	1.5	-1.5	1.5	1494.5332	425.9	1	-0.34	1.08

Table B.1: Observations of the transition: $(^3P_0)4d[2]_{2^1/_2} \leftarrow (^3P)5p^2P_{3/_2}$ in chlorine atoms according to [Com86]. (continued)

B.1.2 LMR-spectra of the test transition in chlorine

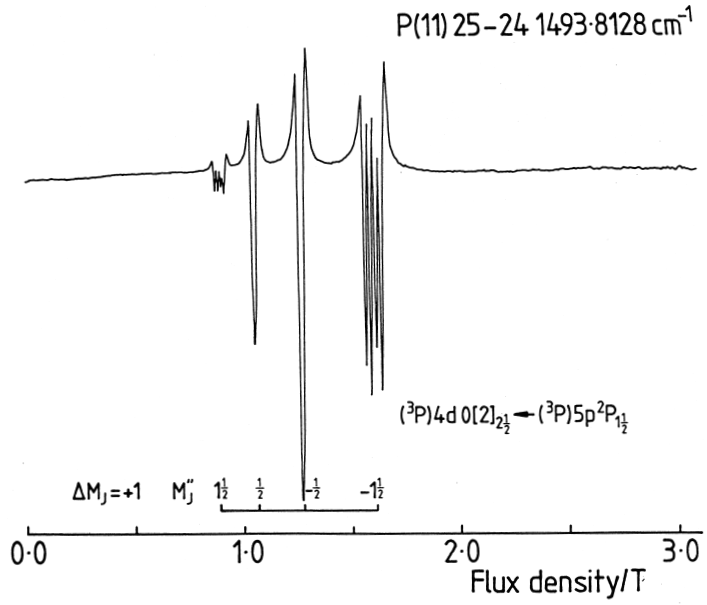

Figure B.1: LMR spectrum of the chlorine test tansition at $\tilde{\nu}_{Laser} = 1493.8128 cm^{-1}$(from [Com86])

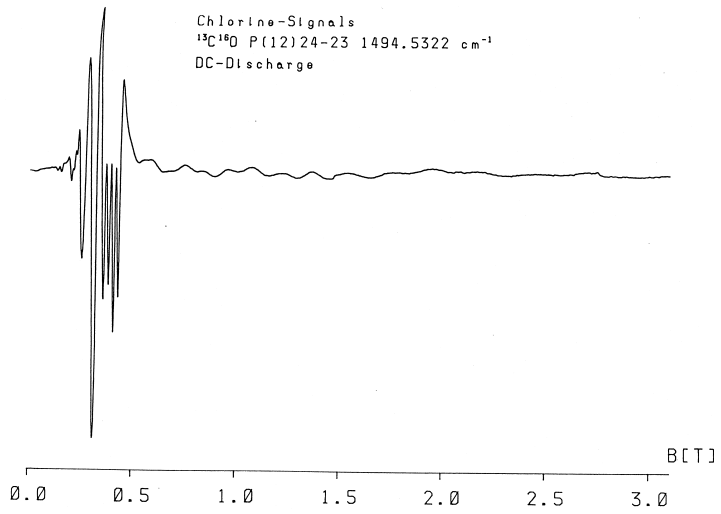

Figure B.2: LMR spectrum of the chlorine test tansition at $\tilde{\nu}_{Laser} = 1494.5322 cm^{-1}$(from [Com86])

Appendix C

Experimental Spectra of Iodine Atoms

C.1 $(^3P_2)9f[4]_{4\frac{1}{2}} \leftarrow (^3P_2)8d[4]_{3\frac{1}{2}}$

C.1.1 Table of resonances

M'_J	M''_J	M_I	$\tilde{\nu}_{Laser}$	B	$exp.TR$	$Weight$	$obs.-calc.$	$calc.TR$
			cm^{-1}	mT	$\frac{MHz}{mT}$		$10^{-3}cm^{-1}$	$\frac{MHz}{mT}$
2.5	3.5	2.5	2055.1593	1569.4	-17.6	1	4.60	-22.8
2.5	3.5	1.5	2055.1593	1598.1	-15.8	1	4.63	-22.8
2.5	3.5	0.5	2055.1593	1634.5	-14.3	1	4.32	-22.8
2.5	3.5	-0.5	2055.1593	1677.2	-19.1	0	2.61	-22.8
2.5	3.5	-1.5	2055.1593	1706.5	-17.3	0	-15.5	-22.8
2.5	3.5	-2.5	2055.1593	1740.1	-20.5	0	-36.5	-22.8
1.5	2.5	2.5	2055.1593	1677.2	-19.1	0	5.01	-21.5
1.5	2.5	1.5	2055.1593	1706.6	-17.0	0	4.25	-21.5
1.5	2.5	0.5	2055.1593	1740.1	-20.5	0	3.21	-21.5
1.5	2.5	-0.5	2055.1593	1779.3	-25.0	0	3.02	-21.5
1.5	2.5	-1.5	2055.1593	1825.5	-26.5	0	4.62	-21.5
1.5	2.5	-2.5	2055.1593	1873.8	-22.5	0	4.50	-21.5

Table C.1: Observed signals of the transition:
$(^3P_2)9f[4]_{4\frac{1}{2}} \leftarrow (^3P_2)8d[4]_{3\frac{1}{2}}$ @ $2056.4234(2)cm^{-1}$

M'_J	M''_J	M_I	$\tilde{\nu}_{Laser}$	B	$exp.TR$	$Weight$	$obs.-calc.$	$calc.TR$
			cm^{-1}	mT	$\frac{MHz}{mT}$		$10^{-3}cm^{-1}$	$\frac{MHz}{mT}$
0.5	1.5	2.5	2055.1593	1779.3	-25.0	0	-8.85	-20.2
0.5	1.5	1.5	2055.1593	1798.2	-18.4	0	-16.6	-20.2
0.5	1.5	0.5	2055.1593	1825.5	-26.5	0	-19.6	-20.2
0.5	1.5	-0.5	2055.1593	1857.7	-22.5	0	-20.4	-20.2
0.5	1.5	-1.5	2055.1593	1891.2	-20.0	0	-21.2	-20.2
0.5	1.5	-2.5	2055.1593	1924.9	-20.0	0	-22.9	-20.2
-0.5	0.5	2.5	2055.1593	1938.2	-15.5	1	3.25	-18.9
-0.5	0.5	1.5	2055.1593	1962.6	-18.0	1	0.97	-18.9
-0.5	0.5	0.5	2055.1593	1990.6	-18.5	1	1.52	-18.9
-0.5	0.5	-0.5	2055.1593	2015.8	-16.4	1	0.86	-18.9
-0.5	0.5	-1.5	2055.1593	2040.3	-14.8	1	0.31	-18.9
-0.5	0.5	-2.5	2055.1593	2062.7	-15.0	1	-1.01	-18.9
-1.5	-0.5	2.5	2055.1593	2099.8	-12.5	1	2.14	-17.7
-1.5	-0.5	1.5	2055.1593	2120.8	-15.5	1	1.03	-17.7
-1.5	-0.5	0.5	2055.1593	2139.7	-18.0	1	0.07	-17.7
-1.5	-0.5	-0.5	2055.1593	2157.2	-14.1	1	-0.34	-17.7
-1.5	-0.5	-1.5	2055.1593	2171.2	-16.1	1	-1.44	-17.7
-1.5	-0.5	-2.5	2055.1593	2182.3	-16.4	1	-2.87	-17.7
-2.5	-1.5	2.5	2055.1593	2288.0	-11.7	1	0.52	-16.4
-2.5	-1.5	1.5	2055.1593	2301.3	-15.5	1	-0.04	-16.4
-2.5	-1.5	0.5	2055.1593	2321.6	-18.0	0	4.71	-16.4
-2.5	-1.5	-0.5	2055.1593	2321.6	-18.0	0	-0.15	-16.4
-2.5	-1.5	-1.5	2055.1593	2321.6	-18.0	0	-3.52	-16.4
-2.5	-1.5	-2.5	2055.1593	2321.6	-18.0	0	-5.41	-16.4
-3.5	-2.5	-2.5	2055.1593	2509.8	-14.1	0	-3.55	-15.1
-3.5	-2.5	-1.5	2055.1593	2509.8	-14.1	0	0.79	-15.1
-3.5	-2.5	-0.5	2055.1593	2509.8	-14.1	0	-1.10	-15.1
-3.5	-2.5	0.5	2055.1593	2509.8	-14.1	0	-2.11	-15.1
-3.5	-2.5	1.5	2055.1593	2509.8	-14.1	0	-2.24	-15.1
-3.5	-2.5	2.5	2055.1593	2509.8	-14.1	0	-1.50	-15.1

Table C.1: Observed signals of the transition:
$(^3P_2)9f[4]_{4\frac{1}{2}} \leftarrow (^3P_2)8d[4]_{3\frac{1}{2}}$ @ $2056.4235(2)cm^{-1}$
(continued)

M'_J	M''_J	M_I	$\tilde{\nu}_{Laser}$	B	$exp.TR$	$Weight$	$obs.-calc.$	$calc.TR$
			cm^{-1}	mT	$\frac{MHz}{mT}$		$10^{-3}cm^{-1}$	$\frac{MHz}{mT}$
-4.5	-3.5	-2.5	2055.1593	2701.5	-11.8	1	-3.20	-13.8
-4.5	-3.5	-1.5	2055.1593	2716.2	-10.7	1	-2.41	-13.8
-4.5	-3.5	-0.5	2055.1593	2730.9	-11.7	1	-2.06	-13.8
-4.5	-3.5	0.5	2055.1593	2747.0	-13.0	1	-1.52	-13.8
-4.5	-3.5	1.5	2055.1593	2763.8	-11.0	1	-1.11	-13.8
-4.5	-3.5	2.5	2055.1593	2781.3	-11.1	1	-0.82	-13.8
2.5	3.5	2.5	2055.1623	1564.3	-17.6	1	3.72	-22.8
2.5	3.5	1.5	2055.1623	1592.4	-15.8	1	3.30	-22.8
2.5	3.5	0.5	2055.1623	1628.2	-14.3	1	2.53	-22.8
2.5	3.5	-0.5	2055.1623	1672.5	-19.1	0	2.04	-22.8
2.5	3.5	-1.5	2055.1623	1701.3	-17.3	0	-16.5	-22.8
2.5	3.5	-2.5	2055.1623	1735.7	-20.5	0	-36.9	-22.8
1.5	2.5	2.5	2055.1623	1672.5	-19.1	0	4.64	-21.5
1.5	2.5	1.5	2055.1623	1701.3	-17.0	0	3.45	-21.5
1.5	2.5	0.5	2055.1623	1735.7	-20.5	0	3.05	-21.5
1.5	2.5	-0.5	2055.1623	1775.7	-25.0	0	3.43	-21.5
1.5	2.5	-1.5	2055.1623	1822.1	-26.5	0	5.18	-21.5
1.5	2.5	-2.5	2055.1623	1869.8	-22.5	0	4.63	-21.5
0.5	1.5	2.5	2055.1623	1775.7	-25.0	0	-8.28	-20.2
0.5	1.5	1.5	2055.1623	1793.3	-18.4	0	-16.9	-20.2
0.5	1.5	0.5	2055.1623	1822.1	-26.5	0	-18.9	-20.2
0.5	1.5	-0.5	2055.1623	1853.7	-22.5	0	-20.1	-20.2
0.5	1.5	-1.5	2055.1623	1886.7	-20.0	0	-21.2	-20.2
0.5	1.5	-2.5	2055.1623	1920.4	-20.0	0	-22.9	-20.2
-0.5	0.5	2.5	2055.1623	1932.4	-15.5	1	2.59	-18.9
-0.5	0.5	1.5	2055.1623	1957.6	-18.0	1	0.81	-18.9
-0.5	0.5	0.5	2055.1623	1985.7	-18.4	1	1.43	-18.9
-0.5	0.5	-0.5	2055.1623	2010.3	-16.4	1	0.38	-18.9
-0.5	0.5	-1.5	2055.1623	2034.2	-14.8	1	-0.54	-18.9
-0.5	0.5	-2.5	2055.1623	2056.7	-15.0	1	-1.89	-18.9

Table C.1: Observed signals of the transition:
$(^3P_2)9f[4]_{4\frac{1}{2}} \leftarrow (^3P_2)8d[4]_{3\frac{1}{2}}$ @ $2056.4234(2)cm^{-1}$
(continued)

M'_J	M''_J	M_I	$\tilde{\nu}_{Laser}$	B	$exp.TR$	$Weight$	$obs.-calc.$	$calc.TR$
			cm^{-1}	mT	$\frac{MHz}{mT}$		$10^{-3}cm^{-1}$	$\frac{MHz}{mT}$
-1.5	-0.5	2.5	2055.1623	2092.6	-12.5	1	0.90	-17.7
-1.5	-0.5	1.5	2055.1623	2115.0	-15.5	1	0.61	-17.7
-1.5	-0.5	0.5	2055.1623	2134.7	-18.0	1	0.12	-17.7
-1.5	-0.5	-0.5	2055.1623	2150.8	-14.1	1	-1.12	-17.7
-1.5	-0.5	-1.5	2055.1623	2165.6	-16.1	1	-1.74	-17.7
-1.5	-0.5	-2.5	2055.1623	2176.8	-16.4	1	-3.11	-17.7
-2.5	-1.5	2.5	2055.1623	2280.3	-11.7	1	-0.69	-16.4
-2.5	-1.5	1.5	2055.1623	2295.5	-15.5	1	-0.21	-16.4
-2.5	-1.5	0.5	2055.1623	2316.6	-18.0	0	4.98	-16.4
-2.5	-1.5	-0.5	2055.1623	2316.6	-18.0	0	0.12	-16.4
-2.5	-1.5	-1.5	2055.1623	2316.6	-18.0	0	-3.25	-16.4
-2.5	-1.5	-2.5	2055.1623	2316.6	-18.0	0	-5.14	-16.4
-3.5	-2.5	-2.5	2055.1623	2503.4	-14.1	0	3.32	-15.1
-3.5	-2.5	-1.5	2055.1623	2503.4	-14.1	0	0.57	-15.1
-3.5	-2.5	-0.5	2055.1623	2503.4	-14.1	0	-1.32	-15.1
-3.5	-2.5	0.5	2055.1623	2503.4	-14.1	0	-2.33	-15.1
-3.5	-2.5	1.5	2055.1623	2503.4	-14.1	0	-2.46	-15.1
-3.5	-2.5	2.5	2055.1623	2503.4	-14.1	0	-1.73	-15.1
-4.5	-3.5	-2.5	2055.1623	2693.9	-11.8	1	-3.71	-13.8
-4.5	-3.5	-1.5	2055.1623	2707.8	-10.7	1	-3.28	-13.8
-4.5	-3.5	-0.5	2055.1623	2723.2	-11.7	1	-2.61	-13.8
-4.5	-3.5	0.5	2055.1623	2740.1	-13.0	1	-1.70	-13.8
-4.5	-3.5	1.5	2055.1623	2755.6	-11.0	1	-1.88	-13.8
-4.5	-3.5	2.5	2055.1623	2773.2	-11.1	1	-1.55	-13.8
-2.5	-3.5	2.5	2059.2090	3533.7	23.1	1	2.32	22.8
-2.5	-3.5	1.5	2059.2090	3593.8	25.7	1	3.19	22.8
-2.5	-3.5	0.5	2059.2090	3646.5	33.3	1	3.50	22.8
-2.5	-3.5	-0.5	2059.2090	3691.8	22.5	1	3.23	22.8
-2.5	-3.5	-1.5	2059.2090	3728.7	34.6	1	3.16	22.8
-2.5	-3.5	-2.5	2059.2090	3756.7	22.0	1	3.66	22.8

Table C.1: Observed signals of the transition:
$(^3P_2)9f[4]_{4\frac{1}{2}} \leftarrow (^3P_2)8d[4]_{3\frac{1}{2}}$ @ $2056.4234(2)cm^{-1}$
(continued)

M_J'	M_J''	M_I	$\tilde{\nu}_{Laser}$	B	$exp.TR$	$Weight$	$obs.-calc.$	$calc.TR$
			cm^{-1}	mT	$\frac{MHz}{mT}$		$10^{-3}cm^{-1}$	$\frac{MHz}{mT}$
-1.5	-2.5	2.5	2059.2090	3773.0	22.5	1	1.56	21.5
-1.5	-2.5	1.5	2059.2090	3821.7	22.0	1	1.39	21.5
-1.5	-2.5	0.5	2059.2090	3866.6	18.4	1	0.72	21.5
-1.5	-2.5	-0.5	2059.2090	3906.6	16.7	1	0.34	21.5
-1.5	-2.5	-1.5	2059.2090	3942.3	17.3	1	-0.19	21.5
-1.5	-2.5	-2.5	2059.2090	3973.3	18.4	1	-0.58	21.5
-0.5	-1.5	2.5	2059.2090	4040.8	16.7	1	0.88	20.2
-0.5	-1.5	1.5	2059.2090	4077.7	14.3	1	0.40	20.2
-0.5	-1.5	0.5	2059.2090	4114.3	16.4	1	-0.87	20.2
-0.5	-1.5	-0.5	2059.2090	4149.0	16.7	1	-1.83	20.2
-0.5	-1.5	-1.5	2059.2090	4182.2	17.0	1	-2.76	20.2
-0.5	-1.5	-2.5	2059.2090	4213.2	17.3	1	-3.18	20.2
0.5	-0.5	2.5	2059.2090	4341.6	14.1	1	1.10	18.9
0.5	-0.5	1.5	2059.2090	4368.8	20.5	1	-0.61	18.9
0.5	-0.5	0.5	2059.2090	4395.4	18.4	1	-1.39	18.9
0.5	-0.5	-0.5	2059.2090	4423.1	18.8	1	-2.31	18.9
0.5	-0.5	-1.5	2059.2090	4451.6	19.6	1	-3.18	18.9
0.5	-0.5	-2.5	2059.2090	4480.7	14.5	1	-3.87	18.9
1.5	0.5	2.5	2059.2090	4681.9	12.3	1	2.63	17.7
1.5	0.5	1.5	2059.2090	4697.4	13.3	1	1.46	17.7
1.5	0.5	0.5	2059.2090	4713.9	13.3	1	1.09	17.7
1.5	0.5	-0.5	2059.2090	4734.3	13.8	1	-0.21	17.7
1.5	0.5	-1.5	2059.2090	4755.7	12.0	1	-0.72	17.7
1.5	0.5	-2.5	2059.2090	4781.1	12.3	1	-2.21	17.7
-2.5	-3.5	2.5	2059.2120	3537.6	23.1	1	2.35	22.8
-2.5	-3.5	1.5	2059.2120	3597.3	25.7	1	3.53	22.8
-2.5	-3.5	0.5	2059.2120	3649.2	33.3	1	4.44	22.8
-2.5	-3.5	-0.5	2059.2120	3695.8	22.5	1	3.19	22.8
-2.5	-3.5	-1.5	2059.2120	3731.3	34.6	1	4.18	22.8
-2.5	-3.5	-2.5	2059.2120	3760.8	22.0	1	3.54	22.8

Table C.1: Observed signals of the transition:
$(^3P_2)9f[4]_{4\frac{1}{2}} \leftarrow (^3P_2)8d[4]_{3\frac{1}{2}}$ @ $2056.4234(2)cm^{-1}$
(continued)

M'_J	M''_J	M_I	$\tilde{\nu}_{Laser}$	B	$exp.TR$	$Weight$	$obs.-calc.$	$calc.TR$
			cm^{-1}	mT	$\frac{MHz}{mT}$		$10^{-3}cm^{-1}$	$\frac{MHz}{mT}$
-1.5	-2.5	2.5	2059.2120	3777.0	22.5	1	1.69	21.5
-1.5	-2.5	1.5	2059.2120	3825.8	22.0	1	1.45	21.5
-1.5	-2.5	0.5	2059.2120	3871.5	18.4	1	0.20	21.5
-1.5	-2.5	-0.5	2059.2120	3912.0	16.7	1	-0.54	21.5
-1.5	-2.5	-1.5	2059.2120	3947.5	17.3	1	-0.93	21.5
-1.5	-2.5	-2.5	2059.2120	3978.2	18.4	1	-1.10	21.5
-0.5	-1.5	2.5	2059.2120	4046.2	16.7	1	0.24	20.2
-0.5	-1.5	1.5	2059.2120	4084.0	14.3	1	-0.86	20.2
-0.5	-1.5	0.5	2059.2120	4119.8	16.4	1	-1.58	20.2
-0.5	-1.5	-0.5	2059.2120	4154.4	16.7	1	-2.48	20.2
-0.5	-1.5	-1.5	2059.2120	4187.5	17.0	1	-3.34	20.2
-0.5	-1.5	-2.5	2059.2120	4218.4	17.3	1	-3.69	20.2
0.5	-0.5	2.5	2059.2120	4348.0	14.1	1	0.06	18.9
0.5	-0.5	1.5	2059.2120	4373.2	20.5	1	-0.40	18.9
0.5	-0.5	0.5	2059.2120	4400.3	18.4	1	-1.49	18.9
0.5	-0.5	-0.5	2059.2120	4427.9	18.8	1	-2.34	18.9
0.5	-0.5	-1.5	2059.2120	4456.2	19.6	1	-3.09	18.9
0.5	-0.5	-2.5	2059.2120	4486.9	14.5	1	-4.79	18.9
1.5	0.5	2.5	2059.2120	4689.2	12.3	1	1.32	17.7
1.5	0.5	1.5	2059.2120	4704.2	13.3	1	0.45	17.7
1.5	0.5	0.5	2059.2120	4720.7	13.3	1	0.08	17.7
1.5	0.5	-0.5	2059.2120	4740.8	13.8	1	-1.04	17.7
1.5	0.5	-1.5	2059.2120	4763.2	12.0	1	-2.14	17.7
1.5	0.5	-2.5	2059.2120	4788.4	12.3	1	-3.51	17.7

Table C.1: Observed signals of the transition:
$(^3P_2)9f[4]_{4\frac{1}{2}} \leftarrow (^3P_2)8d[4]_{3\frac{1}{2}}$ @ $2056.4234(2)cm^{-1}$
(continued)

C.1.2 AOM-Spectra of $2P_9$ and $2P_8$

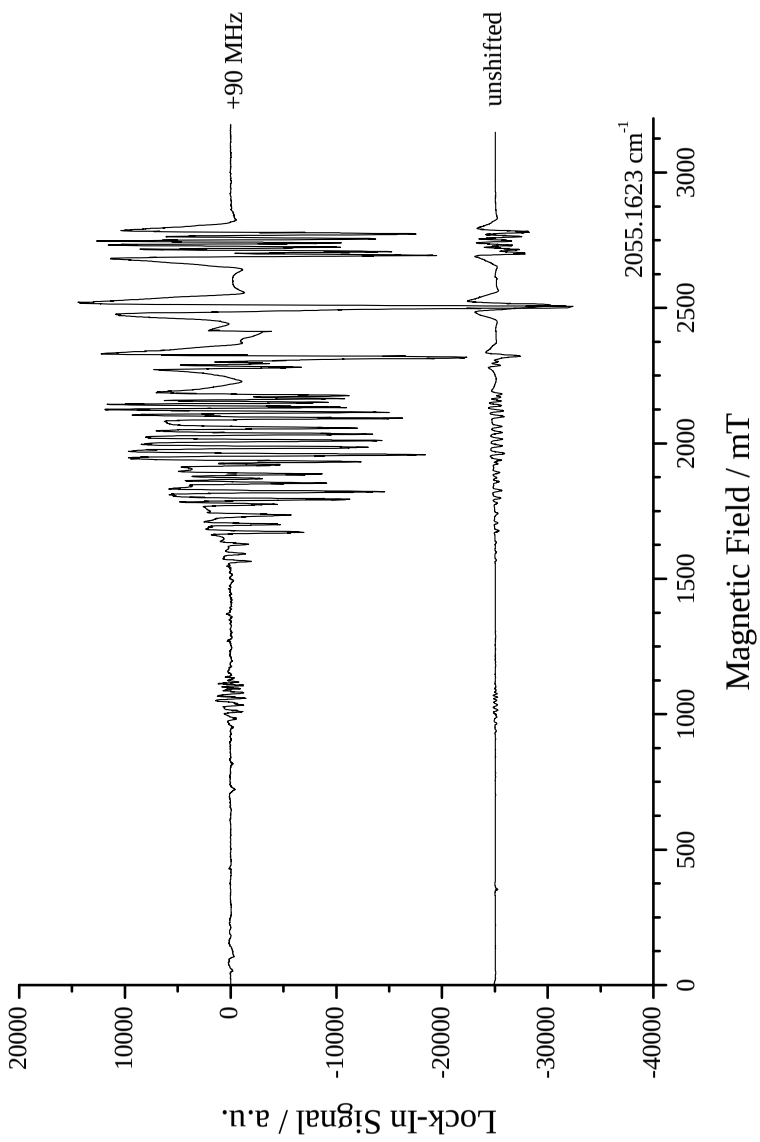

Figure C.1: AOM-Spectrum of I* on the $2P_9$ @ $2055.1623cm^{-1}$ between $0.0T$ and $3.2T$

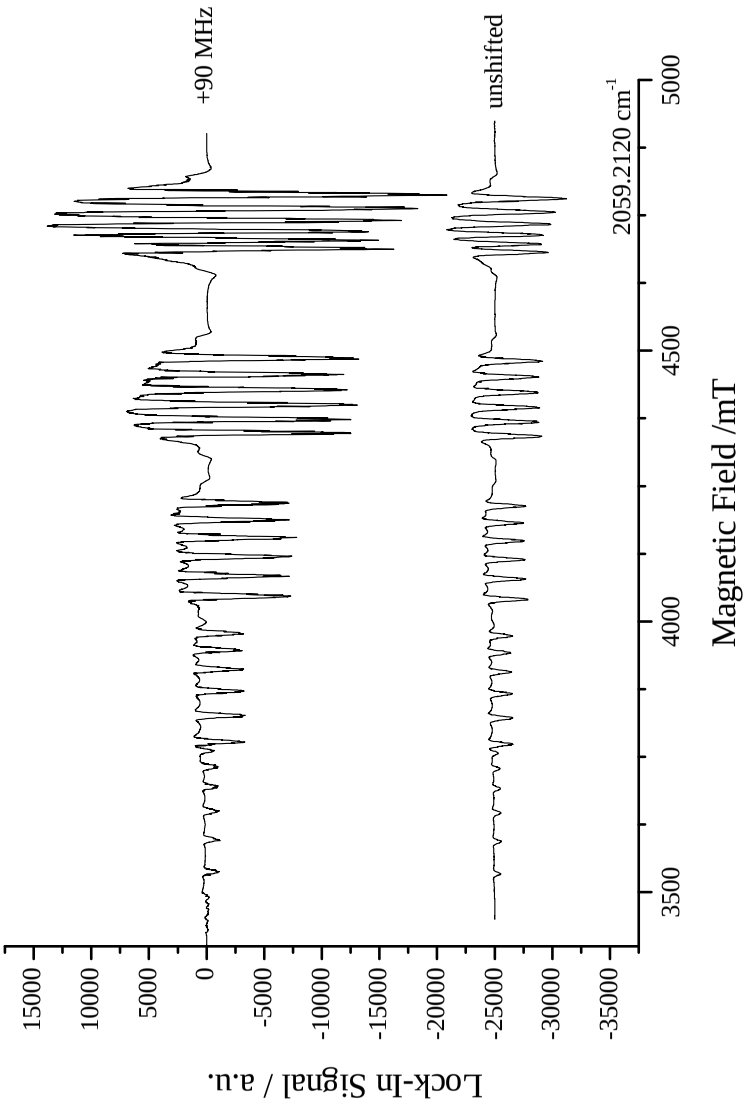

Figure C.2: AOM-Spectrum of I* on the $2P_8$ @ $2059.2120cm^{-1}$ between $3.4T$ and $5.0T$

C.2 $(^3P_2)8p[2]_{\frac{3}{2}} \leftarrow (^3P_2)6d[2]_{\frac{3}{2}}$

C.2.1 Table of resonances

M'_J	M''_J	M_I	$\tilde{\nu}_{Laser}$	B	$exp.TR$	$Weight$	$obs.-calc.$	$calc.TR$
			cm^{-1}	mT	$\frac{MHz}{mT}$		$10^{-3}cm^{-1}$	$\frac{MHz}{mT}$
-1.5	-0.5	1.5	2068.7995	127.4	33.3	1	0.81	29.1
-1.5	-0.5	0.5	2068.7995	169.7	20.0	1	-2.47	29.1
-1.5	-0.5	-0.5	2068.7995	212.0	28.1	1	0.77	29.1
-1.5	-0.5	-1.5	2068.7995	259.2	20.0	1	4.11	29.1
-1.5	-0.5	-2.5	2068.7995	319.6	17.6	1	-1.45	29.1
-0.5	0.5	2.5	2068.7995	396.1	15.0	0	-121	18.6
-0.5	0.5	1.5	2068.7995	419.0	12.5	0	-111	18.6
-0.5	0.5	0.5	2068.7995	441.3	16.1	0	-97.1	18.6
-0.5	0.5	-0.5	2068.7995	461.6	18.8	0	-79.0	18.6
-0.5	0.5	-1.5	2068.7995	473.1	13.8	0	-52.0	18.6
-0.5	0.5	-2.5	2068.7995	496.5	9.3	0	-28.3	18.6
0.5	1.5	1.5	2068.7995	595.8	11.5	1	3.78	8.1
0.5	1.5	0.5	2068.7995	672.1	10.7	1	-2.10	8.1
0.5	1.5	-0.5	2068.7995	738.3	11.7	1	-3.81	8.1
0.5	1.5	-1.5	2068.7995	796.2	10.1	1	-1.76	8.1
0.5	1.5	-2.5	2068.7995	852.3	11.0	1	2.39	8.1
-1.5	-0.5	1.5	2068.8025	131.0	33.3	1	0.60	29.1
-1.5	-0.5	0.5	2068.8025	174.2	20.0	1	-3.47	29.1
-1.5	-0.5	-0.5	2068.8025	215.2	28.1	1	0.88	29.1
-1.5	-0.5	-1.5	2068.8025	263.7	20.0	1	2.99	29.1
-1.5	-0.5	-2.5	2068.8025	324.7	17.6	1	-3.18	29.1

Table C.2: Observed signals of the transition:
$(^3P_2)8p[2]_{\frac{3}{2}} \leftarrow (^3P_2)6d[2]_{\frac{3}{2}}$ @ $2068.6106(10)cm^{-1}$

M'_J	M''_J	M_I	$\tilde{\nu}_{Laser}$	B	$exp.TR$	$Weight$	$obs.-calc.$	$calc.TR$
			cm^{-1}	mT	$\frac{MHz}{mT}$		$10^{-3}cm^{-1}$	$\frac{MHz}{mT}$
-0.5	0.5	2.5	2068.8025	402.1	15.0	0	-123	18.6
-0.5	0.5	1.5	2068.8025	426.2	12.5	0	-112	18.6
-0.5	0.5	0.5	2068.8025	446.9	16.1	0	-97.5	18.6
-0.5	0.5	-0.5	2068.8025	466.4	18.8	0	-78.9	18.6
-0.5	0.5	-1.5	2068.8025	479.6	13.8	0	-53.0	18.6
-0.5	0.5	-2.5	2068.8025	506.2	9.3	0	-31.4	18.6
0.5	1.5	1.5	2068.8025	603.6	11.5	1	4.65	8.1
0.5	1.5	0.5	2068.8025	680.5	10.7	1	-1.41	8.1
0.5	1.5	-0.5	2068.8025	746.0	11.7	1	-2.97	8.1
0.5	1.5	-1.5	2068.8025	805.1	10.1	1	-1.32	8.1
0.5	1.5	-2.5	2068.8025	860.5	11.0	1	2.95	8.1

Table C.2: Observed signals of the transition:
$(^3P_2)8p[2]_{\frac{3}{2}} \leftarrow (^3P_2)6d[2]_{\frac{3}{2}}$ @ $2068.6106(10)cm^{-1}$
(continued)

C.2.2 AOM-Spectrum of the transition $(^3P_2)8p[2]_{\frac{3}{2}} \leftarrow (^3P_2)6d[2]_{\frac{3}{2}}$

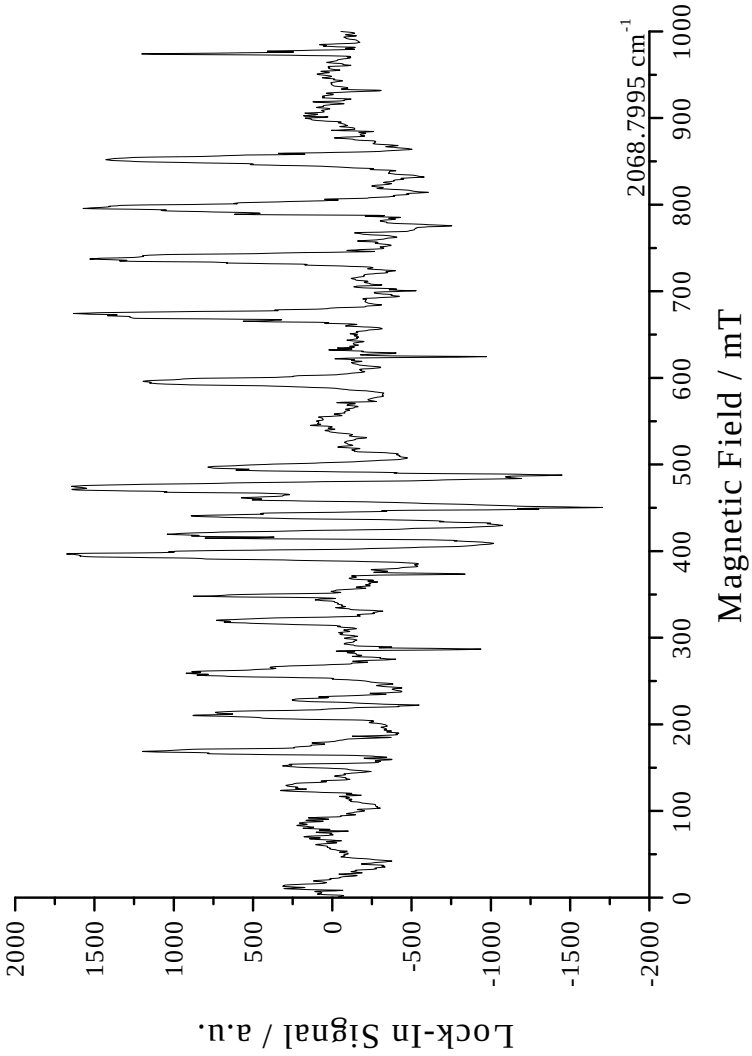

Figure C.3: Spectrum of I^* on the $1P_{12}$ at low fi eld with AOM ($\Delta\nu = -90MHz$) showing the transition $(^3P_2)8p[2]_{\frac{3}{2}} \leftarrow (^3P_2)6d[2]_{\frac{3}{2}}$ @ $2068.6106(10)cm^{-1}$.

C.3 The transition declared as $(^3P_2)nd[2]_{\frac{5}{2}} \leftarrow (^3P_2)np[2]_{\frac{3}{2}}$

C.3.1 Table of resonances

M'_J	M''_J	M_I	$\tilde{\nu}_{Laser}$	B	$exp.TR$	$Weight$	$obs. - calc.$	$calc.TR$
			cm^{-1}	mT	$\frac{MHz}{mT}$		$10^{-3}cm^{-1}$	$\frac{MHz}{mT}$
2.5	1.5	2.5	2068.7995	4219.3	16.4	0	-21.3	13.3
2.5	1.5	1.5	2068.7995	4219.3	16.4	0	-160	13.3
2.5	1.5	0.5	2068.7995	4227.5	8.1	0	4.60	13.3
2.5	1.5	-0.5	2068.7995	4227.5	8.1	0	4.60	13.3
2.5	1.5	-1.5	2068.7995	4231.6	8.1	0	4.60	13.3
2.5	1.5	-2.5	2068.7995	4231.6	8.1	0	4.60	13.3
1.5	0.5	2.5	2068.7995	4480.2	14.5	0	-13.9	12.4
1.5	0.5	1.5	2068.7995	4480.2	14.5	0	-3.09	12.4
1.5	0.5	0.5	2068.7995	4496.3	6.3	1	1.06	12.4
1.5	0.5	-0.5	2068.7995	4523.5	10.3	1	0.60	12.4
1.5	0.5	-1.5	2068.7995	4549.9	14.0	1	0.48	12.4
1.5	0.5	-2.5	2068.7995	4577.6	10.1	1	-0.18	12.4
0.5	-0.5	2.5	2068.7995	4754.7	12.7	1	-2.89	11.6
0.5	-0.5	1.5	2068.7995	4781.0	11.0	1	0.76	11.6
0.5	-0.5	0.5	2068.7995	4813.5	14.1	1	2.01	11.6
0.5	-0.5	-0.5	2068.7995	4850.9	17.6	1	1.36	11.6
0.5	-0.5	-1.5	2068.7995	4889.5	14.3	1	0.24	11.6
0.5	-0.5	-2.5	2068.7995	4932.4	11.3	1	-2.54	11.6

Table C.3: Observed signals of the transition declared as:
$(^3P_2)np[2]_{\frac{3}{2}} \leftarrow (^3P_2)nd[2]_{\frac{5}{2}}$ @ $2066.9266(7)cm^{-1}$

M_J'	M_J''	M_I	$\tilde{\nu}_{Laser}$	B	$exp.TR$	$Weight$	$obs.-calc.$	$calc.TR$
			cm^{-1}	mT	$\frac{MHz}{mT}$		$10^{-3}cm^{-1}$	$\frac{MHz}{mT}$
2.5	1.5	2.5	2068.8025	4224.8	16.4	0	4.60	13.3
2.5	1.5	1.5	2068.8025	4224.8	16.4	0	4.60	13.3
2.5	1.5	0.5	2068.8025	4236.5	8.1	0	4.60	13.3
2.5	1.5	-0.5	2068.8025	4236.5	8.1	0	4.60	13.3
2.5	1.5	-1.5	2068.8025	4251.2	8.1	0	4.60	13.3
2.5	1.5	-2.5	2068.8025	4251.2	8.1	0	4.60	13.3
1.5	0.5	2.5	2068.8025	4486.4	14.5	0	-13.5	12.4
1.5	0.5	1.5	2068.8025	4486.4	14.5	0	-2.66	12.4
1.5	0.5	0.5	2068.8025	4510.6	6.3	1	-1.87	12.4
1.5	0.5	-0.5	2068.8025	4532.2	10.3	1	-0.00	12.4
1.5	0.5	-1.5	2068.8025	4556.3	14.0	1	0.82	12.4
1.5	0.5	-2.5	2068.8025	4586.5	10.1	1	-0.88	12.4
0.5	-0.5	2.5	2068.8025	4761.8	12.7	1	-2.63	11.6
0.5	-0.5	1.5	2068.8025	4789.2	11.0	1	0.59	11.6
0.5	-0.5	0.5	2068.8025	4819.9	14.1	1	2.53	11.6
0.5	-0.5	-0.5	2068.8025	4856.0	17.6	1	2.38	11.6
0.5	-0.5	-1.5	2068.8025	4895.8	14.3	1	0.80	11.6
0.5	-0.5	-2.5	2068.8025	4940.4	11.3	1	-2.64	11.6

Table C.3: Observed signals of the transition declared as:
$(^3P_2)np[2]_{\frac{3}{2}} \leftarrow (^3P_2)nd[2]_{\frac{5}{2}}$ @ $2066.9266(7)cm^{-1}$
(continued)

C.3.2 AOM-Spectrum of the transition $(^3P_2)nd[2]_{\frac{5}{2}} \leftarrow (^3P_2)np[2]_{\frac{3}{2}}$

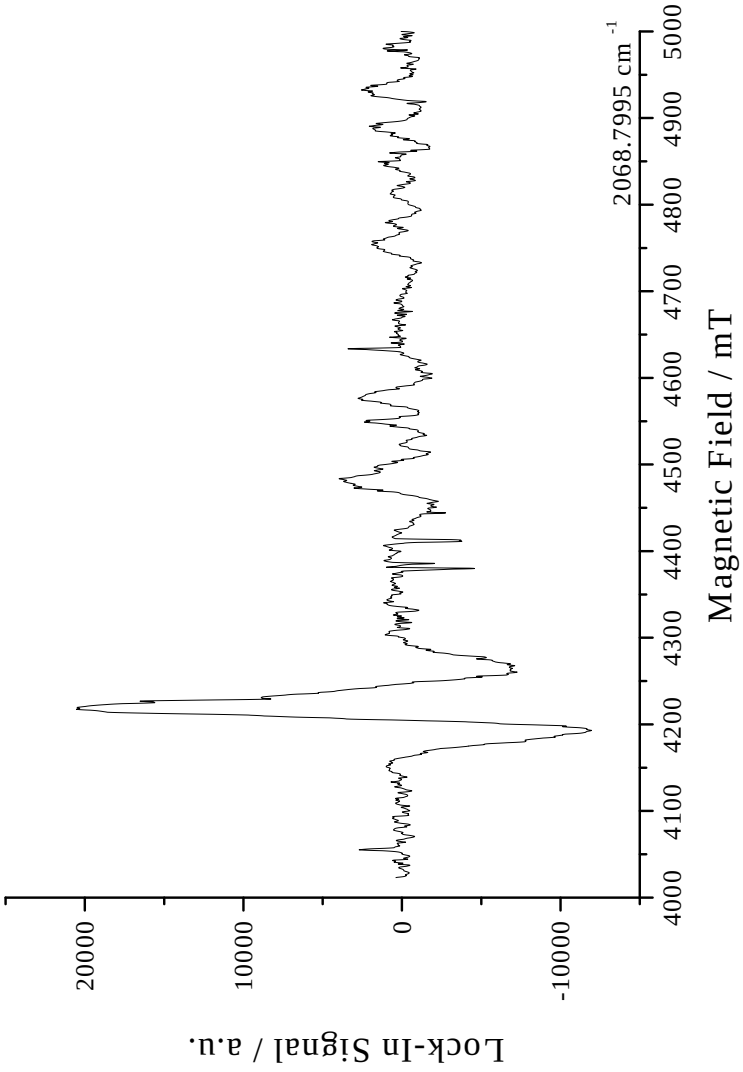

Figure C.4: Spectrum of I^* on the $1P_{12}$ at high fi eld with AOM showing the transition $(^3P_2)nd[2]_{\frac{5}{2}} \leftarrow (^3P_2)np[2]_{\frac{3}{2}}$.

Appendix D

LMR-Spectra of IO

In this appendix, all LMR spectra of iodine monoxide are collected. All spectra are split into two diagrams, the first showing the lower field region up to $2.5T$, the second showing $2.5T$ to $5.0T$ respectively. In the second section, the predicted Zeeman pattern of the R-, Q- and P- of the finestructure transitions for $A_0 = -2073.5cm^{-1}$ are shown.

D.1 Experimental Spectra

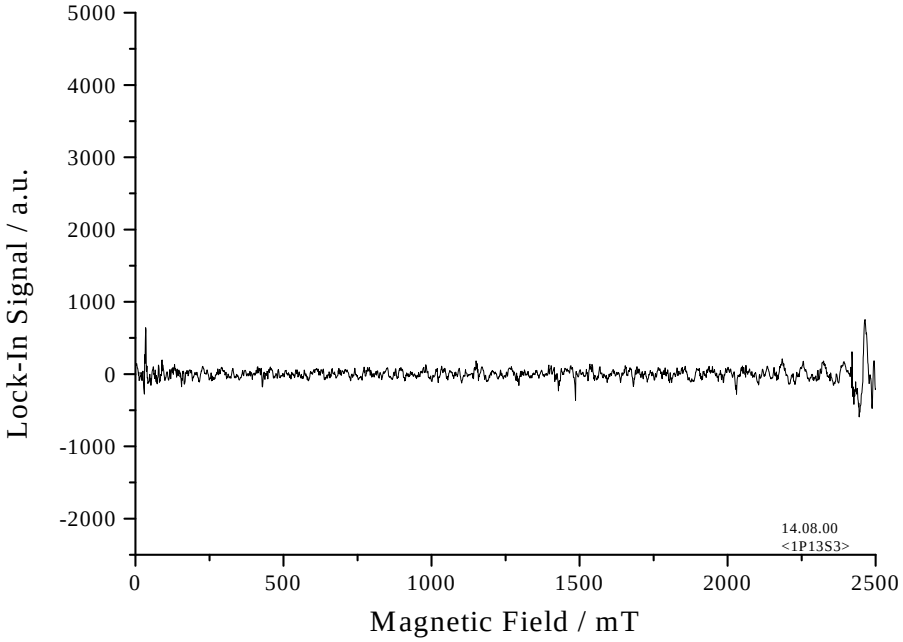

Figure D.1: Spectrum of IO on the $1P_{13}$ @ $2064.584cm^{-1}$ between $0.0T$ and $2.5T$

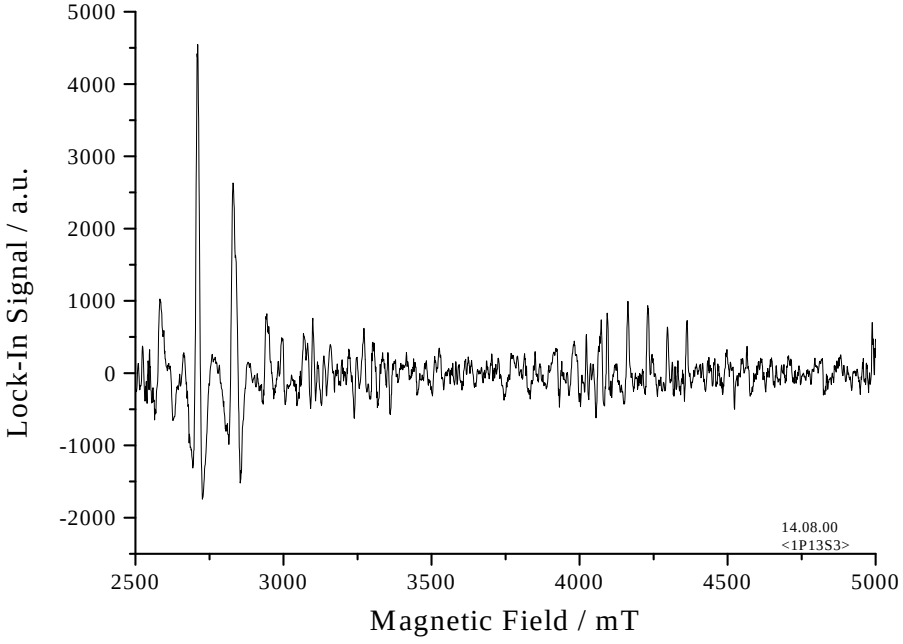

Figure D.2: Spectrum of IO on the $1P_{13}$ @ $2064.584cm^{-1}$ between $2.5T$ and $5.0T$

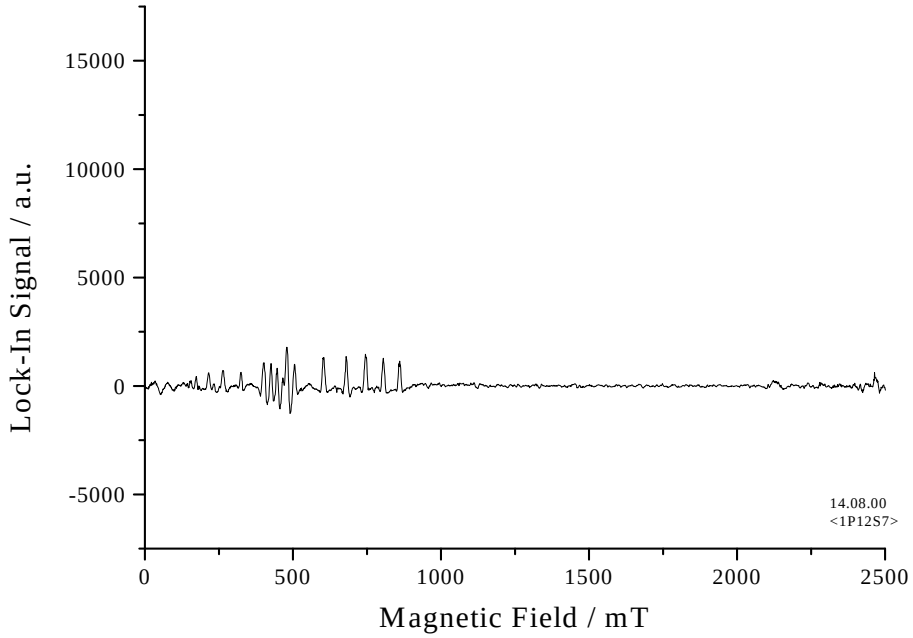

Figure D.3: Spectrum of IO on the $1P_{12}$ @ $2068.8025cm^{-1}$ between $0.0T$ and $2.5T$

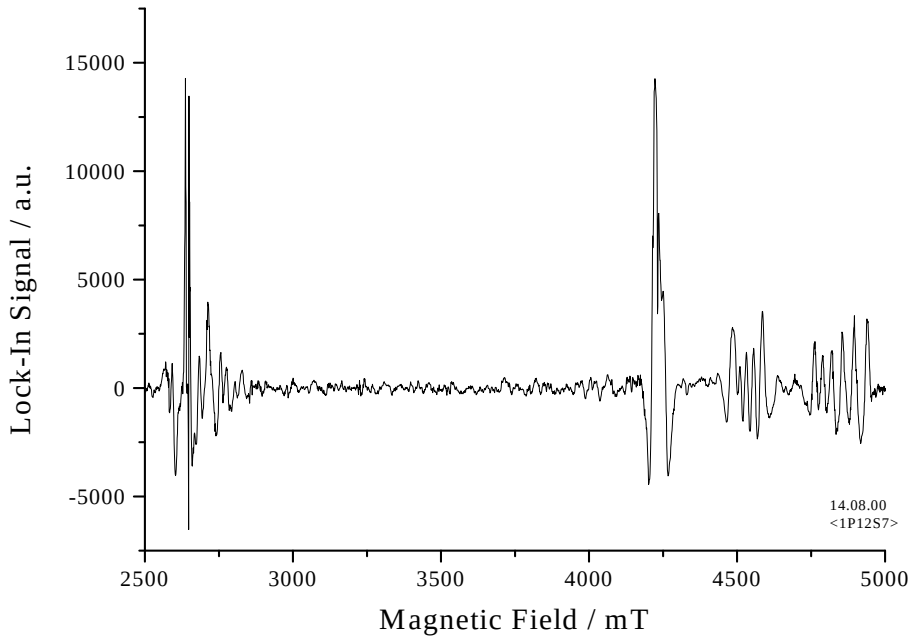

Figure D.4: Spectrum of IO on the $1P_{12}$ @ $2068.8025cm^{-1}$ between $2.5T$ and $5.0T$

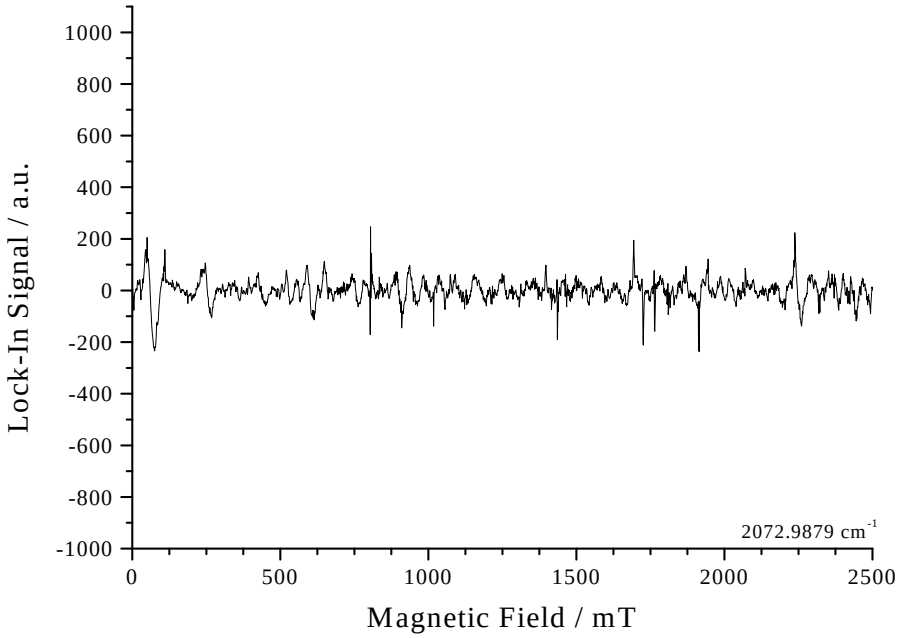

Figure D.5: Spectrum of IO on the $1P_{11}$ @ $2072.9879cm^{-1}$ between $0.0T$ and $2.5T$

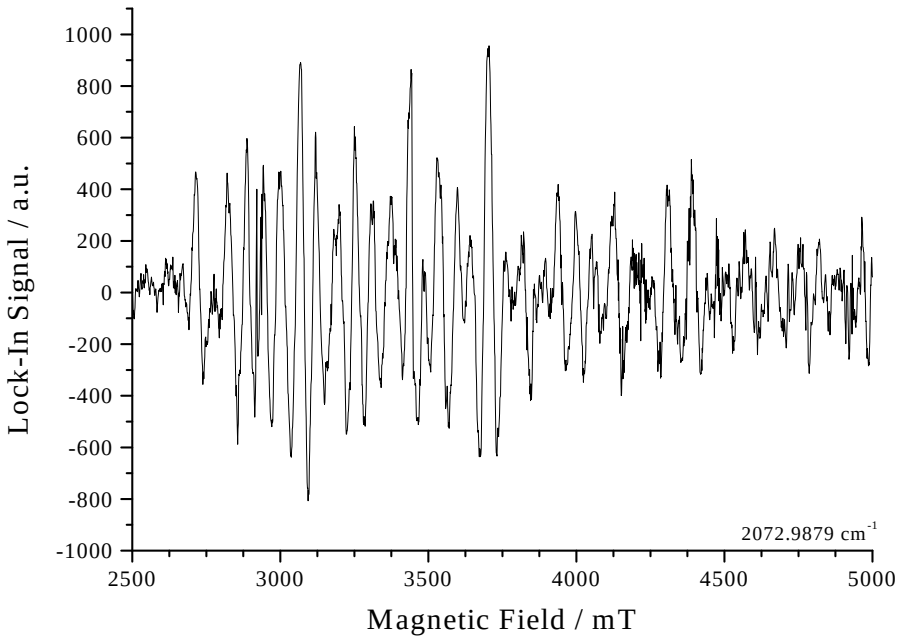

Figure D.6: Spectrum of IO on the $1P_{11}$ @ $2072.9879cm^{-1}$ between $2.5T$ and $5.0T$

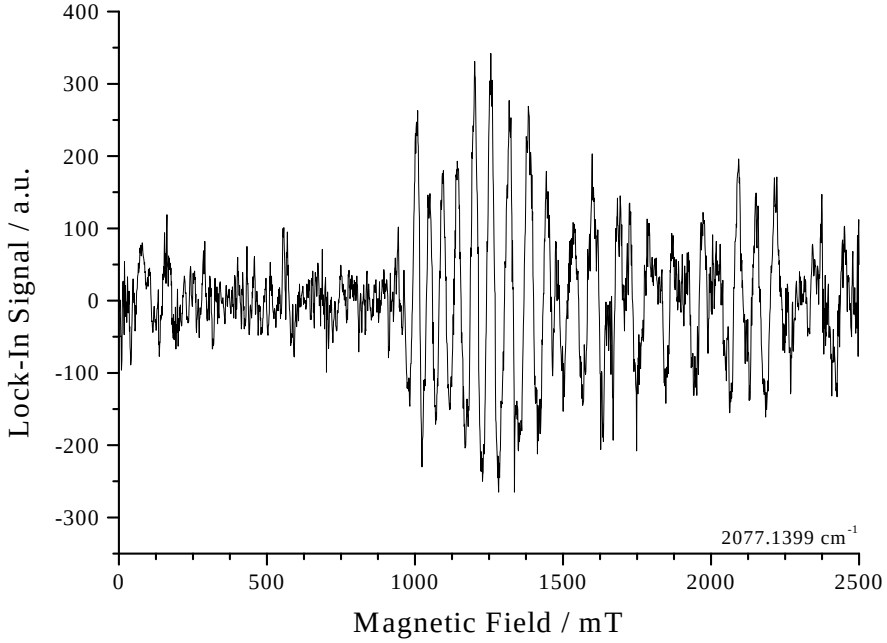

Figure D.7: Spectrum of IO on the $1P_{10}$ @ $2077.1399cm^{-1}$ between $0.0T$ and $2.5T$

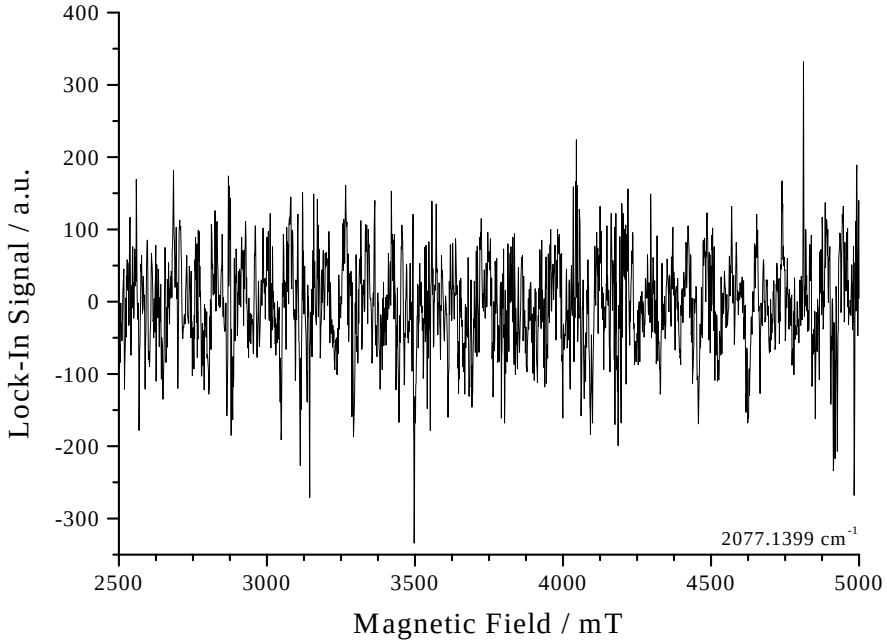

Figure D.8: Spectrum of IO on the $1P_{10}$ @ $2077.1399cm^{-1}$ between $2.5T$ and $5.0T$

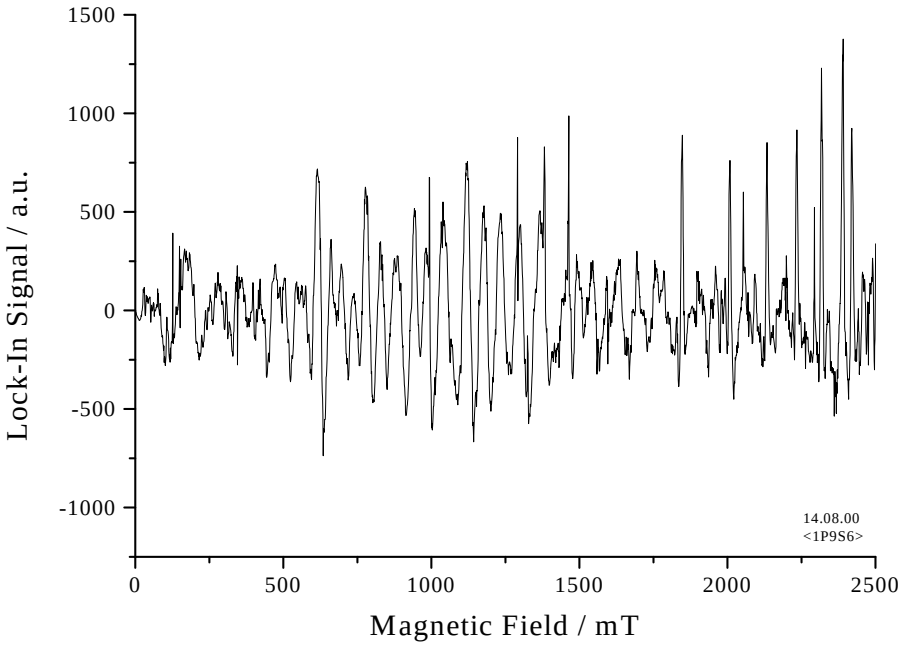

Figure D.9: Spectrum of IO on the $1P_9$ @ $2081.2583cm^{-1}$ between $0.0T$ and $2.5T$

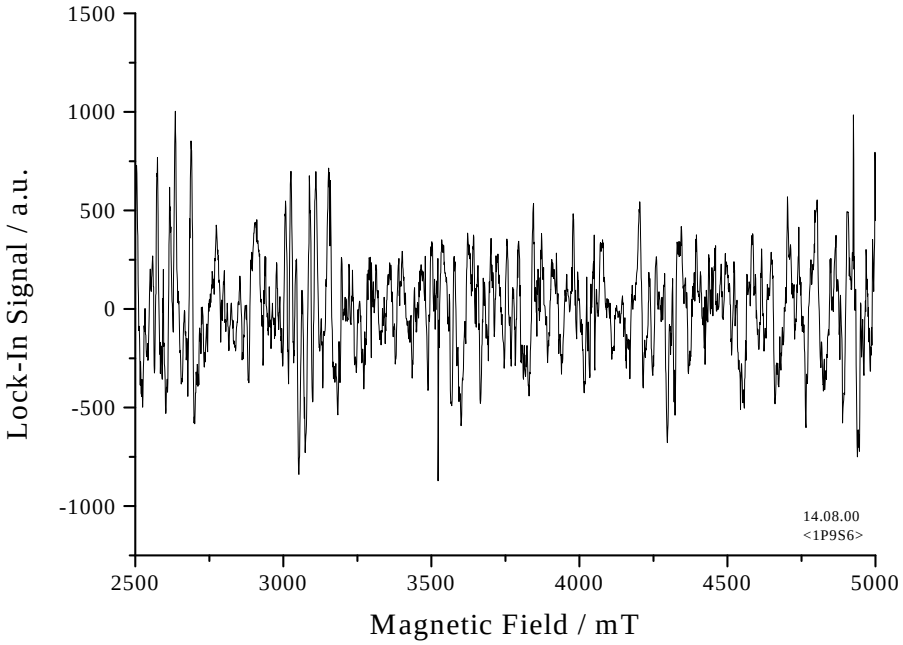

Figure D.10: Spectrum of IO on the $1P_9$ @ $2081.2583cm^{-1}$ between $2.5T$ and $5.0T$

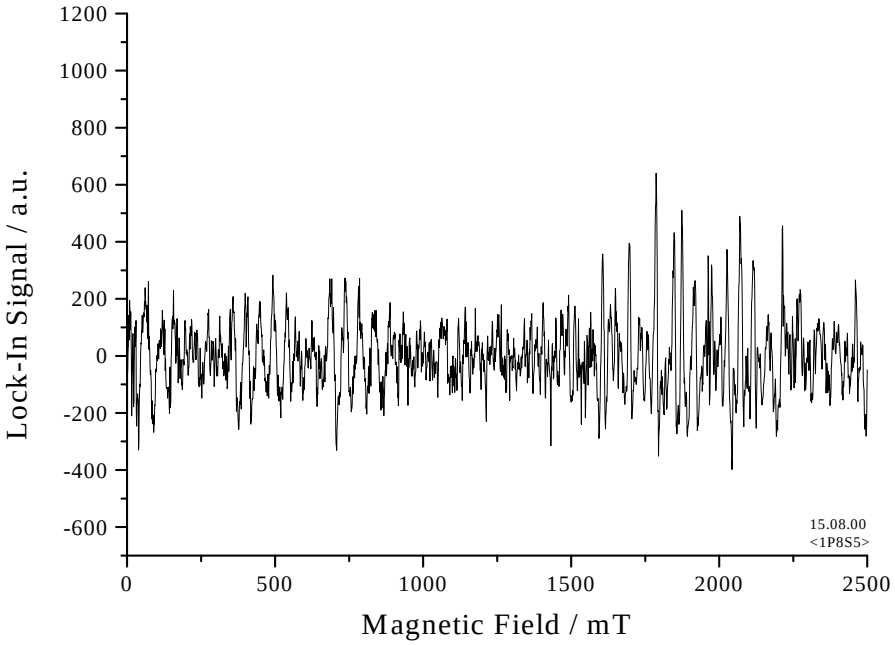

Figure D.11: Spectrum of IO on the $1P_8$ @ $2085.3431cm^{-1}$ between $0.0T$ and $2.5T$

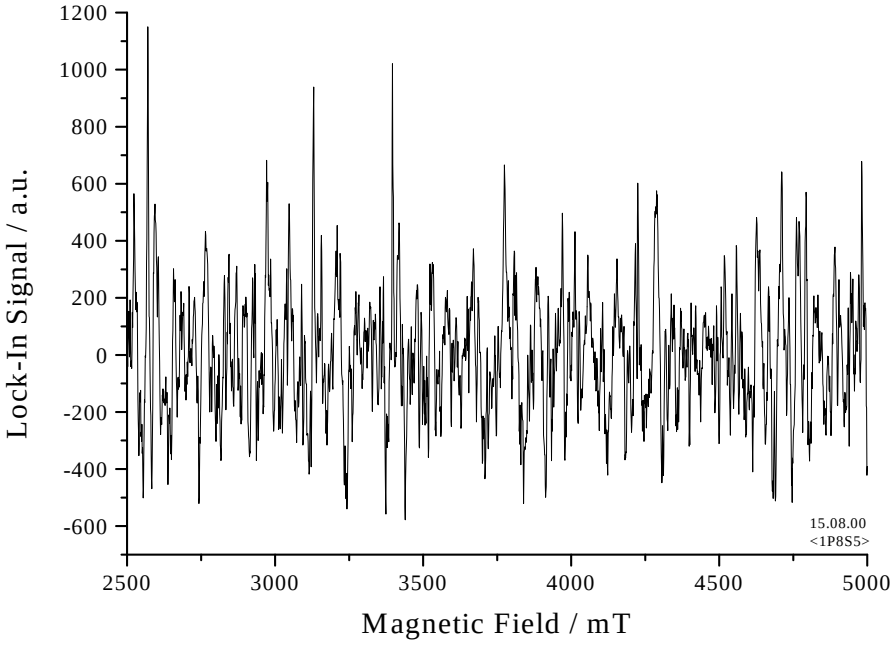

Figure D.12: Spectrum of IO on the $1P_8$ @ $2085.3431cm^{-1}$ between $2.5T$ and $5.0T$

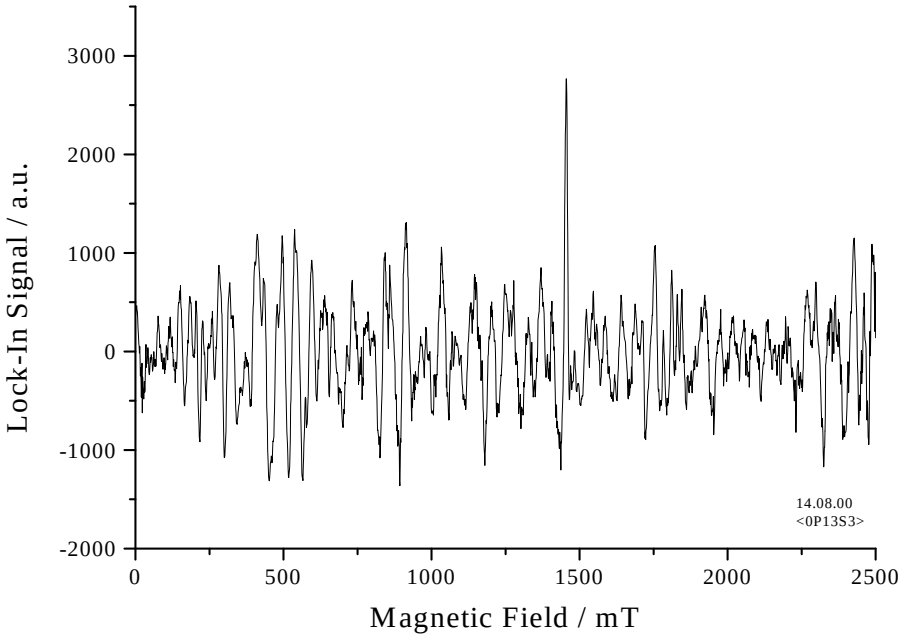

Figure D.13: Spectrum of IO on the $0P_{13}$ @ $2090.6087cm^{-1}$ between $0.0T$ and $2.5T$

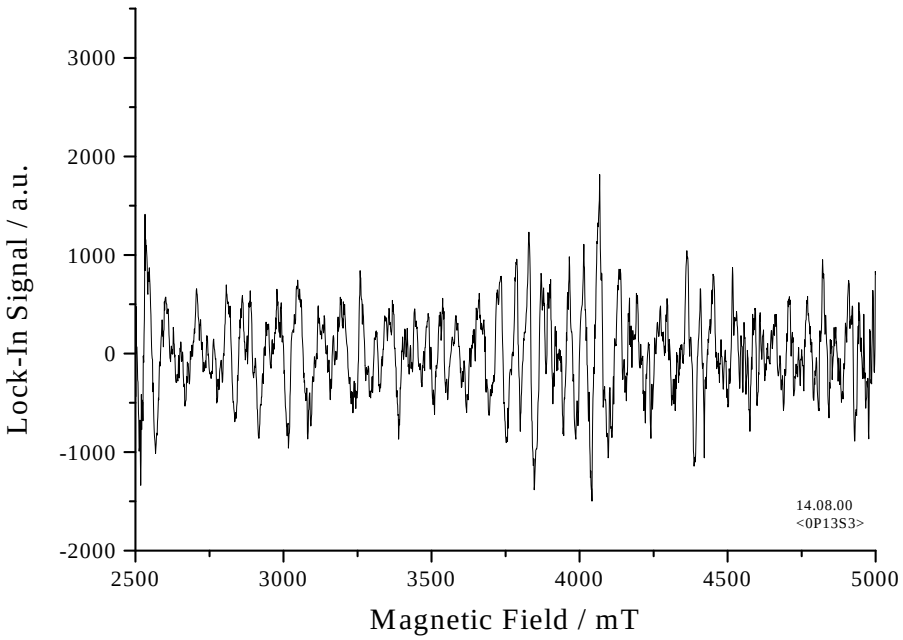

Figure D.14: Spectrum of IO on the $0P_{13}$ @ $2090.6087cm^{-1}$ between $2.5T$ and $5.0T$

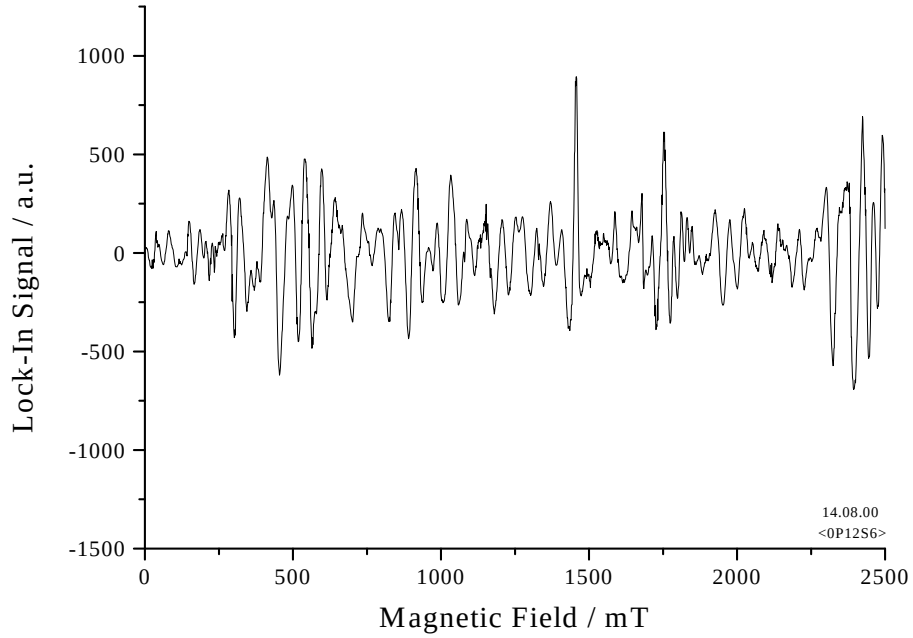

Figure D.15: Spectrum of IO on the $0P_{12}$ @ $2094.8623cm^{-1}$ between $0.0T$ and $2.5T$

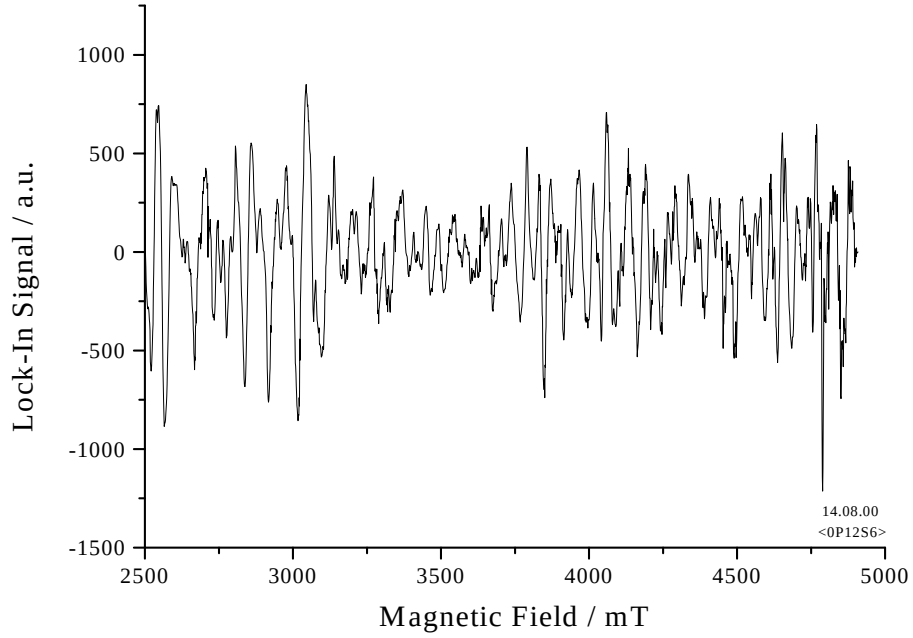

Figure D.16: Spectrum of IO on the $0P_{12}$ @ $2094.8623cm^{-1}$ between $2.5T$ and $5.0T$

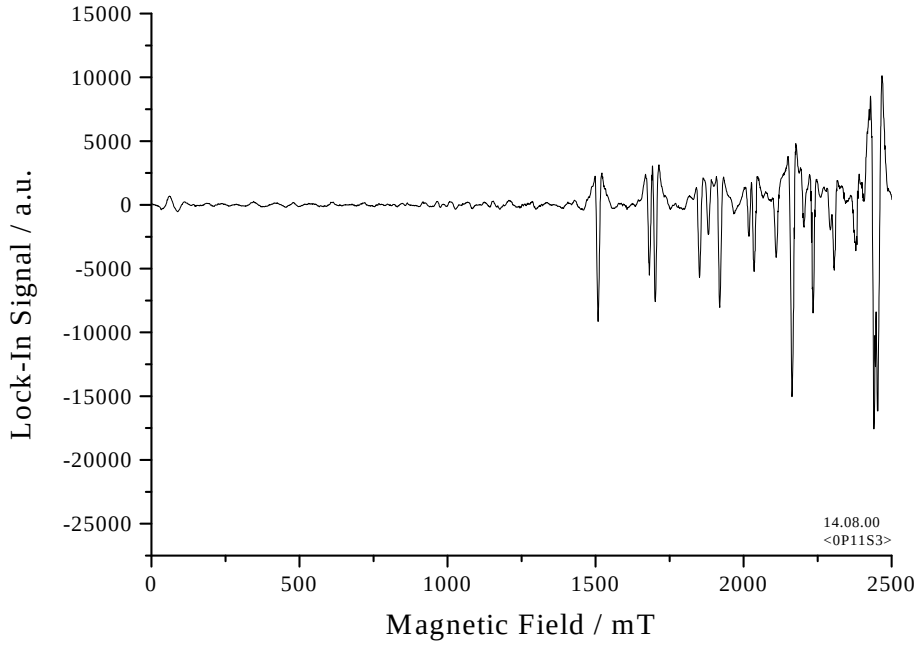

Figure D.17: Spectrum of IO on the $0P_{11}$ @ $2099.0827cm^{-1}$ between $0.0T$ and $2.5T$

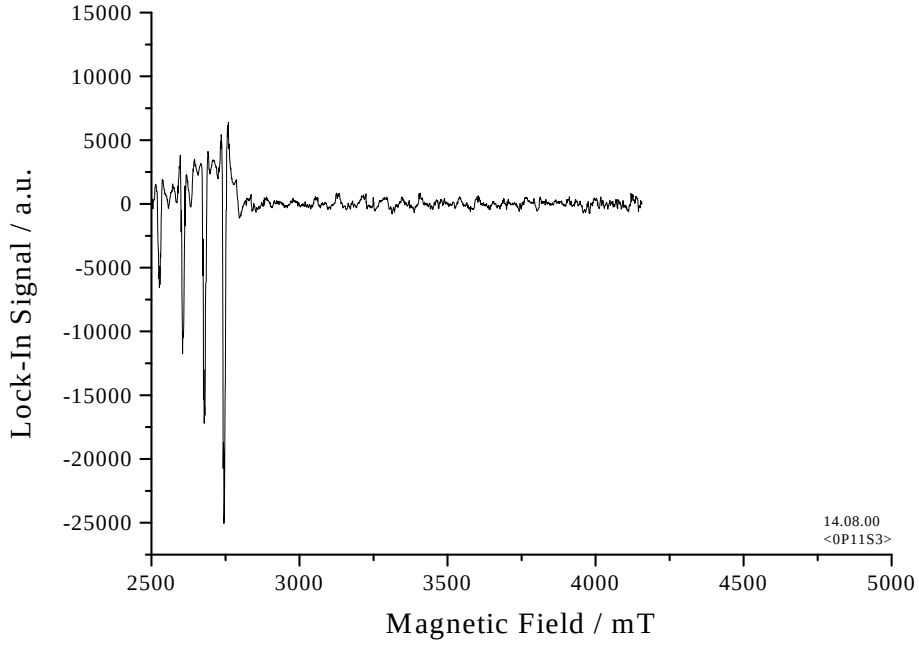

Figure D.18: Spectrum of IO on the $0P_{11}$ @ $2099.0827cm^{-1}$ between $2.5T$ and $5.0T$

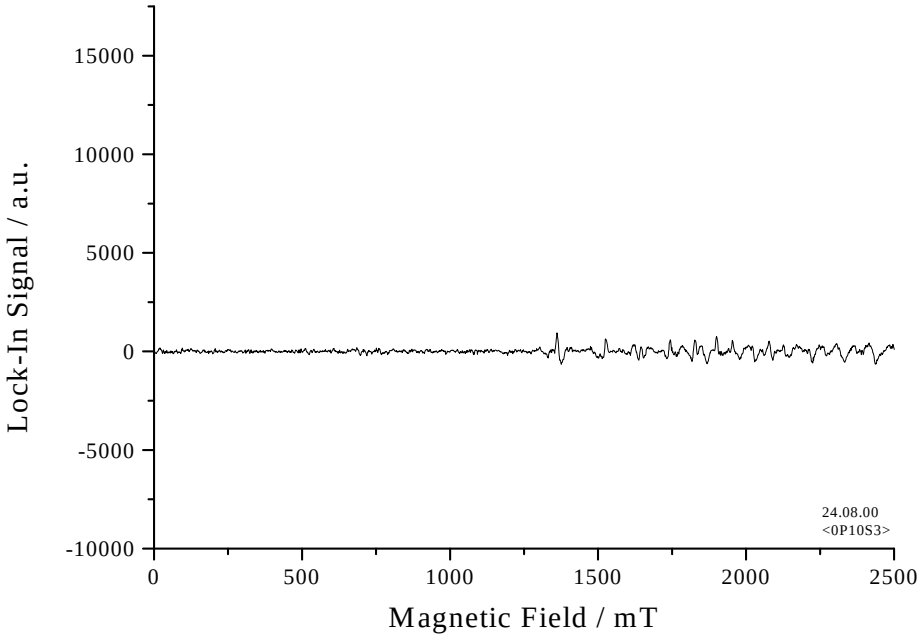

Figure D.19: Spectrum of IO on the $0P_{10}$ @ $2103.2697cm^{-1}$ between $0.0T$ and $2.5T$

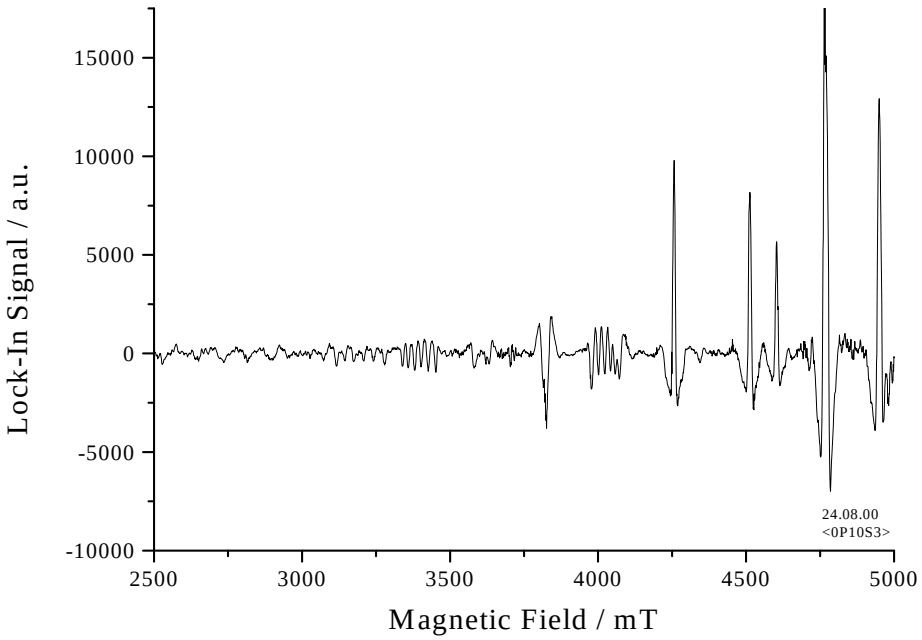

Figure D.20: Spectrum of IO on the $0P_{10}$ @ $2103.2697cm^{-1}$ between $2.5T$ and $5.0T$

D.2 Predicted Zeeman pattern of P-, Q- and R-branch

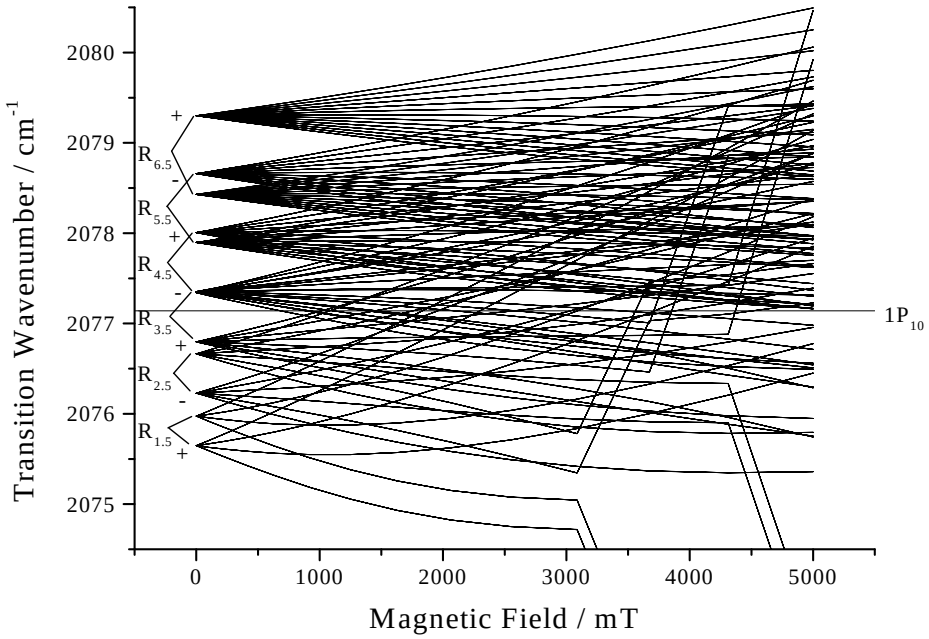

Figure D.21: Zeeman pattern calculated for the R-branch of IO ($A_0 = -2073.5cm^{-1}$)

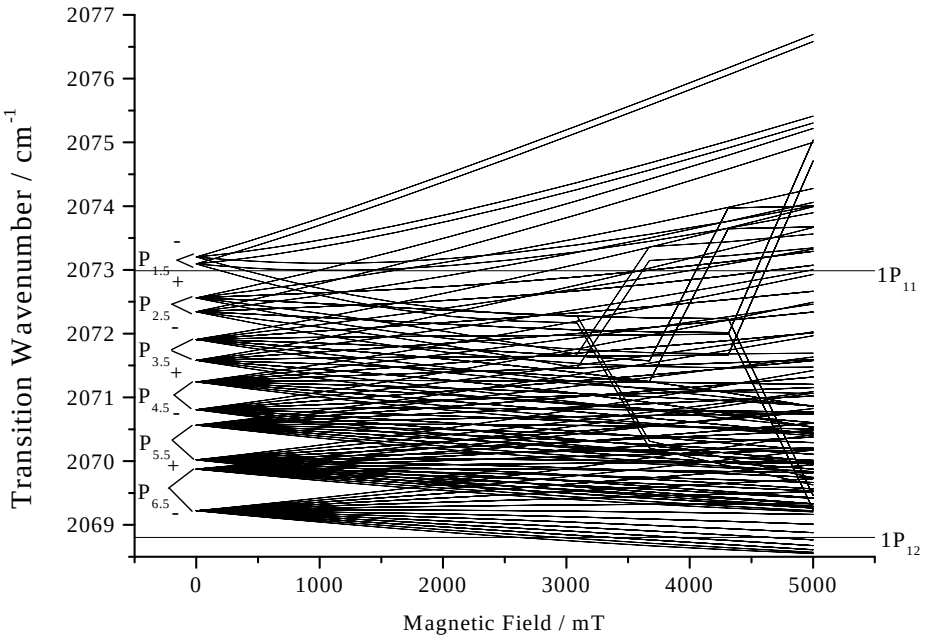

Figure D.22: Zeeman pattern calculated for the P-branch of IO ($A_0 = -2073.5cm^{-1}$)

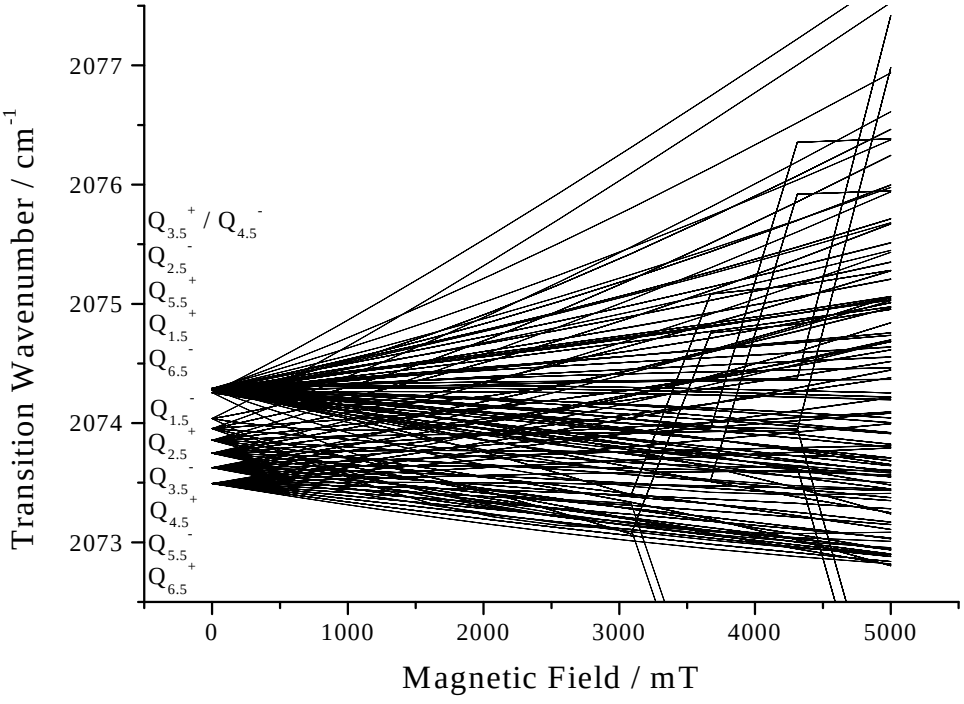

Figure D.23: Zeeman pattern calculated for the Q-branch of IO ($A_0 = -2073.5cm^{-1}$)

Bibliography

[Abr70] A. Abragam and B. Bleaney. *Electron Paramagnetic Resonance of Transition Ions*. Clarendon Press, Oxford (1970).

[All00] B. J. Allan, G. McFiggans, J. M. C. Plane, and H. Coe. Observations of Iodine Monoxide in the Remote Marine Boundary Layer. *Journal of Geophysical Research - Atmospheres*, 105(D11):14,363–14,369 (2000).

[Bac88] E. Bachem. *Faraday-LMR-Spektroskopie an Molekülionen und Integration eines Akusto-Optischen Modulators*. Diplom-thesis, Institut f¨ur Angewandte Physik, Bonn (1988).

[Bek83] J. P. Bekooy, W. L. Meerts, and A. Dymanus. High-Resolution Laser-Rf Spectroscopy on the $A^2\Pi_{\frac{3}{2}}$ System of Iodine Oxide (IO). *Journal of Molecular Spectroscopy*, 102:320 – 343 (1983).

[Bie01] J. Bieroń, P. Pyykk¨o, and D. Sundholm. Nuclear Quadrupole Moments of Bromine and Iodine from Combined Atomic and Molecular Data. *Physical Review A*, 64:052,507–1 – 052,507–12 (2001).

[Boh89] W. Bohle. *Konzepte der Absorptionsspektroskopie mit Polarisationseffekten*. Tech. rep., Institut f¨ur Angewandte Physik, Bonn (1989).

[Bre98] T. Breitbach. *Improvements of the Laser Magnetic Resonance Spectrometer at Oxford*. Diplom-thesis, Physical & Theoretical Chemistry Laboratory, Oxford and Institut f¨ur Angewandte Physik, Bonn (1998).

[Bro72] J. M. Brown, C. R. Byfleet, B. J. Howard, and D. K. Russell. The Electron Resonance Spectra of BrO, IO and SeF in $J = \frac{5}{2}$. *Molecular Physics*, 23(3):457 – 468 (1972).

[Bro78] J. M. Brown, M. Kaise, C. M. L. Kerr, and D. J. Milton. A determination of fundamental Zeeman parameters for the OH. *Molecular Physics*, 36(2):553–582 (1978).

[Bro79a] J. M. Brown, E. A. Colburn, J. K. G. Watson, and F. D. Wayne. An Effective Hamiltonian for Diatomic Molecules. *Journal of Molecular Spectroscopy*, 74:294–318 (1979).

[Bro79b] J. M. Brown and A. J. Merer. Lambda-Type Doubling Parameters for Molecules in Π Electronic States of Triplet and Higher Multiplicity. *Journal of Molecular Spectroscopy*, 74:488–494 (1979).

[Car67] A. Carrington, P. N. Dyer, and D. H. Levy. Gas-Phase Electron Resonance Spectrum of ClO. *The Journal of Chemical Physics*, 47(5):1756 – 1763 (1967).

[Car70] A. Carrington and P. N. Dyer. Gas-Phase Electron Resonance Spectra of BrO and IO. *The Journal of Chemical Physics*, 52(1):309 – 314 (1970).

[Coh01] E. A. Cohen. Private Communication (2001).

[Com86] E. R. Comben. *The Study of Small Molecules by High Resolution Molecular Spectroscopy*. Ph.D. thesis, Physical & Theoretical Chemistry Laboratory, Oxford (1986).

[Con35] E. U. Condon and G. H. Shortley. *The Theory of Atomic Spectra*. Cambridge University Press (1935).

[Dur60] R. A. Durie, F. Legay, and D. A. Ramsay. An Emission System of the IO Molecule. *Canadian Journal of Physics*, 38:444–452 (1960).

[Edm74] A. R. Edmonds. *Angular Momentum in Quantum Mechanics*. Princeton University Press (1974).

[Fro52] R. A. Frosch and H. M. Foley. Magnetic Hyperfine Structure in Diatomic Molecules. *Physical Review*, 88:1337–1349 (1952).

[Ged82] A. Gedanken, M. B. Robin, and Y. Yafet. The Methyl Iodide Multiphoton Ionization Spectrum with Intermediate Resonance in the A-Band Region. *Journal of Chemical Physics*, 76(10):4798–4808 (1982).

[Geo90] T. George. *Entwicklung und Stabilisierung eines CO-Fundamentalbanden-Lasers*. Diplom-thesis, Institut f¨ur Angewandte Physik, Bonn (1990).

[Geo93] T. George. *Der CO-Fundamentalbanden-Laser als sekundärer Frequenzstandard: Hochauflösende Sättigungsspektroskopie an CO und OCS zwischen 1900 and 2100 cm^{-1}*. Phd-thesis, Institut f¨ur Angewandte Physik, Bonn (1993).

[Gil92] M. K. Gilles, M. L. Polak, and W. C. Lineberger. Photoelectron Spectroscopy of the Halogen Oxide Anions $FO^-, ClO^-, BrO^-, IO^-, OClO^-, OIO^-$. *The Journal of Chemical Physics*, 96(11):8012 – 8020 (1992).

[Hin82] A. Hinz, J. Pfeiffer, W. Bohle, and W. Urban. Mid-Infrared Laser Magnetic Resonance using the Faraday and Voigt Effects for Sensitive Detection. *Molecular Physics*, 45(6):1131–1139 (1982).

[Hum71] C. Humphreys, E. Paul, and L. Minnhagen. First Spectra of Chlorine, Bromine and Iodine in the $4 - \mu m$ Region. *Journal of the Optical Society of America*, 61(1):110–114 (1971).

[Hun26] F. Hund. Zur Deutung einiger Erscheinungen in den Molekelspektren. *Zeitschrift für Physik*, 36:657–674 (1926).

[Ker98] S. M. Kermode. *The Search for HNO in its $^3A''$ Electronic State and the Infrared Spectrum of the IO Radical*. Part II thesis, University of Oxford (1998).

[Kie59] C. Kiess and C. Corliss. Description and Analysis of the First Spectrum of Iodine. *Journal of Research of the National Bureau of Standards*, 63A(1):1–18 (1959).

[Kop56] H. Kopfermann. *Kernmomente*. Akademische Verlagsgesellschaft, Frankfurt / M., 2nd edn. (1956).

[Lem88] B. Lemoine, C. Demuynck, and J. L. Destombes. Rydberg Transitions of neutral Magnesium in the Infrared: Frequency Measurements and Zeeman Effect. *Astronomy and Astrophysics*, 191:L4–L6 (1988).

[LK75] E. Luc-Koenig, C. Morillon, and J. Vergès. Etude Expérimentale et Théorique de l'Iode Atomique. *Physica Scripta*, 12:199–219 (1975).

[Mar60] W. Martin and C. Corliss. The Spectrum of Singly Ionized Atomic Iodine ($I\!I\!I$). *Journal of Research of the National Bureau of Standards*, 64A(6):443–479 (1960).

[Mil01] C. E. Miller and E. A. Cohen. Rotational Spectroscopy of IO $X^2\Pi_i$. *Journal of Chemical Physics*, 115(14):6459–6470 (2001).

[Min61] L. Minnhagen. The Energy Levels of Neutral Atomic Iodine. *Arkiv för Fysik*, 21(26):415–478 (1961).

[M¨ol60] N. H. M¨oller. Calculation of Atomic Energy Levels for Electronic Configurations with one Electron outside a nearly closed Shell and two Holes in this Shell for LS and Pair Couplings. *Arkiv för Fysik*, 18(9):135–157 (1960).

[Moo71] C. E. Moore. *Atomic Energy Levels*, vol. 3 of *NSRDS-NBS 35*. National Bureau of Standards, 3rd edn. (1971).

[Mor75] C. Morillon and J. Vergès. Etude Des Configurations Fondamentales $5s^25p^4$ de Te I et $I\!I\!I$ Par l'Observations Des Raies *Multipolaires* Infrarouges. *Physica Scripta*, 12:145–156 (1975).

[Mur58] K. Murakawa. The Arc Spectrum of Iodine and the Quadrupole Moment of ^{127}I. *Journal of the Physical Society of Japan*, 13(5):484–492 (1958).

[New98] S. M. Newman, W. H. Howie, I. C. Lane, M. R. Upson, and A. J. Orr-Ewing. Predissociation of the $A^2\Pi_{\frac{3}{2}}$ State of IO studied by Cavity Ring Down Spectroscopy. *Journal of the Chemical Society, Faraday Transactions*, 94:2681–2688 (1998).

[Pfe91] C. Pfelzer. *Aufbau und Erprobung einer CO-Faraday-LMR-Apparatur und Messungen am MgO-Molekül*. Diplom-thesis, Institut f¨ur Angewandte Physik, Bonn (1991).

[Sai73] S. Saito. Microwave Spectrum of the IO Radical. *Journal of Molecular Spectroscopy*, 48:530 – 535 (1973).

[Sch88] L. A. Schlie and R. D. Rathge. Transverse Flow cw atomic iodine Laser at $1.315\mu m$. *Journal of Applied Physics*, 63(12):5664–5667 (1988).

[Sch96] C. Schmidt. *Faraday LMR Spektroskopie des* $X^2\Pi(0,1,0) \rightarrow {}^2\Pi(3513cm^{-1})$ *Überganges im* C_2D *Radikal*. Diplom-thesis, Institut f¨ur Angewandte Physik, Bonn (1996).

[Sch00] C. Schmidt. *Hochauflösende Infrarotspektroskopie Rovibronischer Übergänge des Methoxy-Radikals* CH_3O. Ph.D. thesis, Institut f¨ur Angewandte Physik, Bonn (2000).

[Tam99] F. Tamassia, J. M. Brown, and K. M. Evenson. Fine-Structure Spectrum of the FO Radical, observed by Far-Infrared Laser Magnetic Resonance. *Journal of Chemical Physics*, 110(15):7273 – 7286 (1999).

[Tam01] F. Tamassia, S. M. Kermode, and J. M. Brown. A Study of the (2-0) Overtone Bands of the FO, BrO and IO Free Radicals by Laser Magnetic Resonance. *Journal of Molecular Spectroscopy*, 205(1):92–101 (2001).

[Urb87] W. Urban. Infrared Lasers for Spectroscopy. In: J. H. A.C.P. Alves, J. M. Brown, editor, *Frontiers of Laser Spectroscopy of Gases*, NATO ASI Series. Kluwer Academic Publishers, London (1987).

[Urb90] W. Urban. The CO-Overtone Laser – A Spectroscopic Source in a most interesting Wavelength Region. In: M. I. W. Demtr¨oder, editor, *Applied Laser Spectroscopy*. Plenum Press, New York (1990).

[Wit00] F. Wittrock, R. M¨uller, A. Richter, H. Bovensmann, and J. P. Burrows. Measurements of Iodine Monoxide (IO) above Spitsbergen. *Geophysical Research Letters*, 27(10):1471–1474 (2000).

List of Tables

List of Figures

Abstract

This thesis describes an investigation of the spectra of iodine and iodine monoxide in the region about $2100cm^{-1}$. For this study, the CO Faraday Laser Magnetic Resonance Spectrometer at Bonn was used. For the first time a CO-$v = (1 \rightarrow 0)$ laser was used in such an experiment.

For the iodine atoms, several transitions in the region between $2056cm^{-1}$ and $2103cm^{-1}$ were recorded. In order to explain these observations, a theoretical model was developed including the spin-orbit interaction, the magnetic dipole and electrostatic quadrupole hyperfine interactions and the Zeeman effect. The contributions by the electronic configuration were included using the central field approximation. Afterwards this picture was converted into matrix representations for $LS-$, $J_cK, s-coupled$ and $J_cK, s-decoupled$ vector coupling schemes.

A program for fitting the LMR spectra to the theoretical model was written and tested on a known transition between excited states of chlorine. In the course of this, a fault in the previous analysis was found and corrected. For the newly recorded data of iodine atoms, a complete analysis of the transitions was performed for three transitions. Thus, accurate g factors and hyperfine parameters were obtained.

The purpose of the investigation of iodine monoxide was the determination of the finestructure splitting of the vibronic groundstate. Spectra in the region $2064 - 2103cm^{-1}$ were recorded. They have to be attributed to IO for their chemical characteristic and their rich hyperfine structure. Due to the latter, no lines are resolved and an analysis via a least squares fit becomes impossible. An alternative approach by a simulation of the spectra was attempted and the spin-orbit splitting was found to be of the order of $-2073.5(1.0)cm^{-1}$. Although the accuracy of this value is far from being satisfying, it still resembles the first direct measurement of the splitting and improves the previously known value of $-2091(40)cm^{-1}$ considerably.